Emergence in Practice: Case Studies Using Density Functional Theory

SCHOONMAKER, ROBERT,TIMOTHY

Emergence in Practice

Case Studies Using Density Functional Theory

Robert Timothy Schoonmaker

A Thesis presented for the degree of
Doctor of Philosophy

Condensed Matter Physics:Theory
Department of Physics
Durham University
United Kingdom

June 2018

Emergence in Practice

Case Studies Using Density Functional Theory

Robert Timothy Schoonmaker

Submitted for the degree of Doctor of Philosophy

June 2018

Abstract: Emergence is a philsophical concept that has proved to be attractive and long lasting. However in some forms, theories of emergence can be at odds with the process of deductive scientific research. Here I develop a theory of historical emergence based on our inability to describe, and therefore explain highly complex physical systems. To provide evidence for this hypothesis, I perform electronic structure calculations on cyclobutadiene, iron arsenide, elemental iron, and manganese oxide using DFT. I find that only in the iron calculations was historical emergence found. I conclude that historical emergence is an effective definition of emergence, as only the iron calculations exhibited all the behaviour expected in a system that hosts emergence, namely dependent novelty, irreducibility, and unpredictability.

Further, I propose a general theory that is able to calculate the wavefunction of the nuclei in an effective potential. I use this to calculate the Raman spectrum of cyclobutadiene, in which an energy splitting of vibrational energy levels is found due to tunnelling between two chemically equivalent rectangular configurations. I find that the structure of this spectrum, including the tunnelling splitting, can be explained by recourse to the typical motions predicted from a semiclassical model. I conclude that the properties different isomers cannot be calculated using a single

generalised quantum calculation, even though isomers are composed of the same particles and have the same Hamiltonian. Therefore chemical systems are likely to host historically emergent explanations.

From the analysis of single-crystal XRES measurements on FeAs, and symmetry considerations I propose a new canted magnetic structure commensurate with the incommensurate elliptical helical magnetic order. I justify this with an orbital projection method that is able to calculate the susceptibilities of the material to spin-orbit interactions.

I also detail a spin initialisation procedure based on rotations of the exchange-correlation potential, that aims to reduce bias towards undesired density configurations by the density search algorithms in noncollinear systems. I present its application to symmetry unconstrained, noncollinear calculations of manganese oxide and elemental iron. I conclude that this procedure is not suitable for systems with magnetic configurations robust to changes in their exchange and correlation potentials. Additionally symmetry unconstrained calculations are nontrivial, and future calculations will require modified density search algorithms to deal with symmetry unconstrained calculations on many conductors due to complex interactions at the Fermi surface.

Declaration

The work in this thesis is based on research carried out in the Department of Physics at Durham University. No part of this thesis has been submitted elsewhere for any degree or qualification.

Acknowledgements

I would like to thank the Templeton Foundation for generously funding my work.

Contents

Abbreviations

CM Collinear magnetism

DFT Density functional theory

DM Density mixing

EDFT Ensemble density functional theory

LDA Local density approximation

MP Monkhorst-Pack

NCM Noncollinear magnetism

PBE Perdew Burke Ernzerhof

XRES x-ray resonant electron scattering

Chapter 1

Introduction

Emergence is the process by which, to borrow Anderson's turn of phrase [1], more becomes different. In this process, the objects that compose a system of interest exhibit new properties and behaviour; the behaviours of objects that compose the system are changed. Due to this, the study of emergence is deeply linked to reductive explanation, in which the behaviour of a system is described and explained in terms of the fundamental properties of the system's constituents alone. In a reductive explanation the new properties and behaviour directly result from a combination of the properties and behaviour of the constituents. Systems that display this sort of reducible emergence are usually called weakly emergent [2].

But consider another type of emergence, often called strong emergence. It is proposed that in strong emergence the behaviour cannot be reductively explained in terms of the system's constituents. This type of system is of especial interest to some philosophers; for them it is an opportunity to create a new framework for explanation. The allure of this framework is that it may give a robust theoretical method by which explanatory power, or perhaps physical properties and behaviours, are associated not with the divisible constituents of the system, but with something new, be it an object or set of governing laws. The implication would be that as the new thing is not divisible from the system as a whole, it has fundamentally different properties, and might therefore be distinguishable from the usual fundamental physical constituents

or laws present in the world. This line of thought follows a heritage of philosophical study, from Plato's realms of ideals [3], or indeed Cartesian theories of the soul or modern philosophies of the mind, such as non-reductive physicalism. In these theories the new objects or governing laws play decisive explanatory and even causative roles [4, 5, 6]. For this reason the development of such a non-reductive framework that is widely acceptable would be a worthy philosophical achievement.

However those philosophical works which concern the causal and explanatory roles of unphysical objects are unsatisfying to many. Instead most scientists conclude that in a physical experiment, the failure of reductive explanation is likely not to be evidence of a new object, but is instead a failure in the construction of the explanation [7, 8]. Their reasoned position is that the world is extremely complex, and so while a non-reductive theory may capture the behaviour in a simple and easy to understand way, it ultimately fails to give the deeper understanding and knowledge of the complexity. Further in scientific studies there will often be a large number of similar phenomena that are explained only in terms of their physical constituents. In this context the appeal to an new object or governing law to describe a system's behaviour is considered to be a last resort to be used only when exhaustive analysis of the complexity has failed.

These two types of explanatory framework represent two extremes, the so called strong emergentist's and strong reductionist's positions. But there is a third conceivable system, in this case it is not possible to give a reductive explanation, even if all the properties and behaviours are directly attributable to the system's constituents. Due to the complexity often present in physical systems, it is not unreasonable to expect that such a system may exist. This type of emergence I call epistemic emergence because if it exists it will not be possible to validate that the system is reducible. Necessarily, to describe the emergence in such systems one must describe how a system's properties and behaviours cannot be deduced or explained by reference to the properties of the constituents. This requires an understanding of specific system properties, and the challenge is therefore to describe how this occurs in a

sufficiently general yet satisfactory fashion.

Epistemic emergence seems the most fruitful area in which to make progress on the philosophical account of emergence. This is because as at one extreme a strong reductionist position places all the weight on a theoretical explanation and requires no deeper discussion of philosophy. At the other extreme a phenomenon that is strongly emergent has yet to be conclusively experimentally isolated, and requires a large and challenging philosophical description. Instead the philosophical quandary of epistemic emergence is present and less severe, though may additionally be able to contribute both to the understanding of how a satisfying theoretical explanation is constructed, and provide an account of how such a reductive explanation is not possible and the necessary consequences for the study of physical phenomena that result. As a result I will focus on this type of emergence.

In this thesis I will develop a theory for a type of epistemic emergence, which is based on complexity and the physical and practical limitations that constrain information and knowledge. This theory entails that when the number of experimental outcomes or physical states that must be described for a satisfactory understanding of an explanation are too large to be represented physically, such a system must be treated differently and deserves to be called emergent. I will show that in such a system at least some of the outcomes of an experiment on such an emergent physical system will not be verifiably repeatable, as the number of different outcomes are too numerous for the same result to be expected each time. Therefore an experimenter can only understand the processes of the system by reference to a specific measured outcome, and cannot create a complete understanding of the system. As such I call this type of emergence "historical emergence".

However a study of epistemic emergence of this sort must rely on a study of physics and the behaviour of physical systems. To this end I will also model some physical systems which have been selected for their relevance to emergence, with density functional theory (DFT) [9]. DFT was chosen as it provides an effective way to describe and explain the origin of physical processes, while at the same time providing

the pragmatic advantage of speed when it is used to study many electron systems. This is by comparison to more precise approaches like quantum Monte-Carlo, and GW approximation approaches that are computationally much more intensive and therefore much slower [10].

I will first study the benefits and limitations of DFT for a study of historical emergence, by performing symmetry relaxed and noncollinear calculations on the well understood materials elemental Fe in the bcc structure and the magnetic insulator MnO in chapter 5.2. I will then study physical systems to inform the discussion of historical emergence. The systems I study will be FeAs in chapter 4, which was chosen for its complex magnetic structure formed of a noncollinear elliptical canted spin-spiral, which has a periodicity that is itinerant under temperature variation; the four-membered carbon ring cyclobutadiene in chapter 3, was chosen as it exhibits quantum mechanical tunnelling between two chemically equivalent configurations, and therefore does not have a fixed chemical structure.

This study of physical systems will show how historical emergence is able to inform and contribute to the process of science. I show that this definition of historical emergence is able to distinguish between different types of physical system. As it distinguishes between them, it is also able to show why particular processes and systems deserve to be treated differently. It provides a framework to explain why not everything can be deduced from the fundamental physical laws, and at the same time can inform the process by which further research can be performed.

1.1 Motivation for emergence

In the process of emergence, the objects that compose a system of interest exhibit new properties and behaviour; the behaviour of the objects that compose the system are changed [1]. This definition helps to capture the sense of emergence, however alone it is not really a satisfactory definition. This is because as discussed in the previous section, there are a number of senses in which this can be true. However

before presenting or discussing specific theories of emergence, I will outline the motivation for considering emergence as a concept at all.

The concept of emergence was originally coined by the British emergentists, the most prominent of these was C.D. Broad [11]. The motivation behind their proposition was the observed disunity in the sciences. While physics was highly effective at describing and manipulating mechanical systems and single free particles like electrons [12, 13] in the 1920's, it had no satisfactory explanation for chemical behaviour, and chemistry was observed to have the same relationship with biology. For the British emergentists, this was taken as empirical evidence for the disunity of the sciences. The word emergence was coined to describe the process by which a new behaviour comes into existence from the combination of the well understood fundamental constituents. For them, examples of systems that might possibly be emergent included life, mentality, and acetone [11, 12].

Of course with hindsight, what was a mystery of how the fundamental particles form new phenomena such as chemical compounds has been well explained by quantum mechanics in a way that now seems to undermine Broad's original position. As such discussions of emergence have continued in two forms, in the first form life and mental phenomenon have not been explained by new theories, and so continue to be discussed in similar ways in the philosophical literature [14, 15, 16]. The second form which is more relevant to this work is based on the observation that the considerable explanatory advances of quantum mechanics have not unified science into a single field of study. Science is still composed of a wide array of specialised fields. Despite the apparent dependence of these on more fundamental theories, most of the work done relates only to the specific area of specialism [17, 18].

That scientific study can be independent of a description of the fundamental phenomena, implies that an explanation in terms of the fundamental constituents is not required and perhaps inappropriate. On this basis a philosophy in which all phenomena must be grounded in, and described by, the properties of the fundamental constituents is at best unhelpful and at worst simply incorrect. However for

a useful philosophy that can be used in the process of research and the study of new phenomena, an applied theory of strong emergence along the lines discussed above is likely to be just as unhelpful. As has been shown by the historical example of Broad and others, an application of the theory of strong emergence is especially susceptible to the formulation of an incorrect hypothesis. In short, to get caught up in the tangle of strong emergence just as one is trying to understand a new system is to invite disaster.

The source of this trouble is that in the study of an incompletely understood system, a failure to explain a behaviour by reference to the fundamental behaviour of the constituents may originate in either the inadequacy of the method of explanation, the inability for the problem to be explained in a particular way, or an insufficiency of the fundamental behaviour [1]. However regardless of which it is, a scientist needs some way to make sense of the situation, and an appeal to either of the extreme reductionist/emergentist positions cannot provide this. However an epistemic theory of emergence is sensitive to how a method of explanation can be inadequate, and so will have a practical use.

It is important to note however, since theories of epistemic emergence deliberately concern themselves with the particular methods of analysis [19, 20], such theories are open to the criticism that they are not worth studying. The argument runs that since they are about our own subjective theories, they necessarily have nothing useful to say about objective behaviour, and as we get closer to the correct objective theory we will end up having to discard or re-run the argument. On this reasoning it would instead be better to work on an objective theory from the start. However I disagree. First, objective accounts of emergence have been motivated by subjective theories, but has had nothing useful to say about them. For example of Broad and chemistry: despite the work put in this study failed to inform or advance the understanding of chemical knowledge. Ultimately it has either been discarded or been through significant amendment, so that work seems to have been wasted. In this case it

[1] Like trying to explain planetary motion with respect to electromagnetism.

might have in fact been more useful to detail a subjective theory that contributed to the scientific discussion. Secondly as yet there is no convincing account for an objective emergence, nor do I feel there to be any promising ones.

Instead it may be more fruitful to make incremental progress on a less complex problem. Indeed, it may be that physics in fact does place objective limits on any subjective theory. In this case it would be no less fundamental than a theory of emergence, and possibly a great deal more useful. However before the discussion of a new type of epistemic emergence, it is useful to discuss previous work on epistemic emergence.

1.1.1 Batterman's singular limit emergence

In Batterman's account of emergence [19] , he starts his book with the Euler strut [21, ch. 14]. This is a thought experiment that is composed of a single vertical structural beam that is gradually loaded until at the critical loading weight, it collapses in one of two directions: either left or right. Crucially the gross structure of the beam is symmetric, such that it is the dynamic microstate of the system that determines which way the beam collapses. With this example he observes that although the microstructure is decisive in determining the direction in which the beam will collapse, which of the possible different microstates the strut is in gives essentially no extra explanatory information about the critical collapse weight. Instead this collapse weight can be determined by macrostructural properties of the strut: the shape and area of its cross-section, its Young's modulus, and its length. He observes that once one knows the gross structure of the beam, the instantaneous microstructure is completely unnecessary to explain the most important quantity, the critical collapse weight of the system.

This argument about the Euler strut is only illustrative however, since it must be conceded that when one is provided with details about both the micro- and gross structure of the system, one is in fact being supplied with the same relevant

information (that of the gross structure) twice. This is because if one is given the microstructure of the system, one may concede that via a renormalisation procedure, it might be possible to recover the gross structure of the beam [7]. Batterman however counters this criticism, as he reasons that this generation of the gross structure relies on an appeal to a continuous beam which only makes sense in the limit where the size of the beam becomes infinite. However this infinite limit is necessarily unrealisable. As a result the gross structure of the strut is qualitatively different to the microstructure of the physical system, and he reasons the use of this method can never precisely reproduce a continuum structure like the gross structure of the beam which is used to determine the Euler strut equation in the classical limit [19, p. 124].

In this way, Batterman purports to show how his theory of emergence captures how an emergent system becomes qualitatively different to the properties of its parts. What distinguishes his account from theories of strong emergence, is that his theory turns only on the *explanatory* roles of the different theoretical objects. In so doing his discussion is partly about the physical objects. However the emergence in the system is actually not a property of the physical system, but of the theoretical description. It is for this reason that I class Batterman's emergence as epistemic emergence, since it is principally concerned with a practical inability to explain properties and behaviours in terms of the microstructural constituents of a physical system.

However criticism is often levelled at Batterman's description of emergence, as he grants that it might be possible to explain the behaviour of the system without an appeal to these singular theoretical objects. In such a situation he observes that this would be done "poorly" [19, p. 52]. In so doing Batterman makes clear that his conception of emergence is primarily practical in its motivation. The concern for this theory of emergence is that it is not robust as it may be open to an attack that is motivated by changes or improvements in the practical methods that he relies on. However the systems that he studies: the Euler strut, behaviour at thermodynamic critical points, and optical systems which require both ray and diffraction optics, are

understoody with capable, simple, and are so far unchanged methods. Nonetheless, many eschew his account in favour of an objective account, that would remain unaffected when the practical methods relevant to the problem improve.

1.1.2 Computational emergence

It is worth examining computational emergence as well. In the philosophy of pancomputationalism, the world is studied using principles of computer science [22]. This is motivated by the ability to model any physical system as a computer, and is defined with respect to an effective quantisation of space and time. The time quantisation is the time taken to perform a single operation in the model computer and is given by the minimum time period it takes for a physical system to evolve between different states [23]. The space quantisation determines the effective memory for the model computer, and is the total number of available states available in the physical system [22]. These two components, the memory and the number of compute operations performed during a time period, make up the computational resources available to a physical system.

Computational emergence is motivated by the observation that physical systems appear to instantiate particular algorithms. The definition of an algorithm is regular process which results in a particular physical state or property being realised. However, in certain cases the computational overhead in terms of memory and compute operations for computing the algorithm exceeds the computational resources available to the system. Such a system is called emergent [24]. A common example in the literature is protein folding, which is said to instantiate the minimum energy search algorithm [24, 20, 25]. In this example it is observed that the number of compute operations that are required to perform an exhaustive energy search of all the different conformations of a protein is vastly larger than the number of different compute operations available to the system during the time in which a protein folds.

However there are a number of concerns about computational emergence. The

principle weakness is the observation or assertion that a physical system instantiates an algorithm. The observation of an instantiated algorithm which must be emergent, necessarily conflicts with the observation of the available computational resources. Further, many algorithms give similar results, but there is no way to account for which one of these algorithms the physical system in question truly instantiates. In a system that appears emergent, it may be the case that there is another similar algorithm that is functionally equivalent, but is not emergent. For example in the protein folding example frequently used, an alternative algorithm is the local minimum energy algorithm further aided by certain symmetries or patterns in the protein structure itself [26, 27]. Even for a choice of algorithm there are many implementations. Indeed for the local minimum energy search algorithm, a quantum nonadiabatic computational implementation requires significantly fewer resources than a classical computational implementation [28].

Therefore while computational emergence has strengths, namely a rigorous way to determine if a system is emergent or not, it suffers from a flaw that the method used to discern if computational emergence is present, is unsound in its practice. This is because there is not yet a rigorous way to determine if a system only appears to be emergent due to an incorrect assessment about the instantiated algorithm, or because it really is emergent. Some progress has been made based on Kolmogorov-Chaitin incompressibility [24], as an incompressible algorithm cannot be replaced by a more efficient algorithm. However the underlying concerns remain, as it may be that while the algorithm chosen may reproduce certain aspects of the observed physical behaviour, the correct instantiated algorithm is different. To my knowledge there are no concrete physical examples of computationally emergent systems.

1.1.3 Historical emergence

Much of the motivation for and problems with emergence, centre around difficulties in an account of complexity. Historical emergence is motivated by complexity as

well. However as I demonstrated in the discussion of pancomputational emergence, physical systems are usually open so that they interact with the rest of the world. Due to this, discussion about complexity needs to be constrained, or else depending on an individual's opinion, an open system may grow to larger proportions as it includes all the influences of the cosmos, or collapse[2]. This ultimately distracts from the real interest which originates in the physical system itself.

In previous accounts of emergence, whether or not a physical system is emergent can be based on whether the explanation of the physical process has a particular construction, like in the accounts of Batterman [19], Mumford [2, pp. 92-109], and Luisi [25]. It can also be based on whether or not the causal processes must be of a particular form, like in Broad's account [11]. Indeed these two approaches are closely related, but it is useful to rest a definition of emergence on a single secure foundation. Since I aim to describe historical emergence epistemically, it is more natural to couch the account in an explanatory, rather than the causal framework.

An account of explanation

Modern theoretical discussion of a philosophical theory of explanation was started by Hempel and Oppenheim in 1948 [29]. Their theory, which was later named the deductive-nomological (D-N) theorem of scientific explanation, formed a key part of much of the ensuing philosophical discussion on the topic [30]. There are however some valid criticisms of this account of scientific explanation. As a result I will take their theory and modify it so that it can be practically used in an account of emergence. In particular I will omit the condition that an explanation must be grounded in physical or general laws. Doing this allows me to skirt a number of thorny philosophical issues, though introduces the added complication that I must support my argument by grounding it in the wider scientific literature.

In an explanatory set-up constructed in the D-N form I identify three important

[2]The reasoning follows that if the universe is in a pure state all the behaviour and properties in it may be obtained by the simple application of the relevant operators to that state [8].

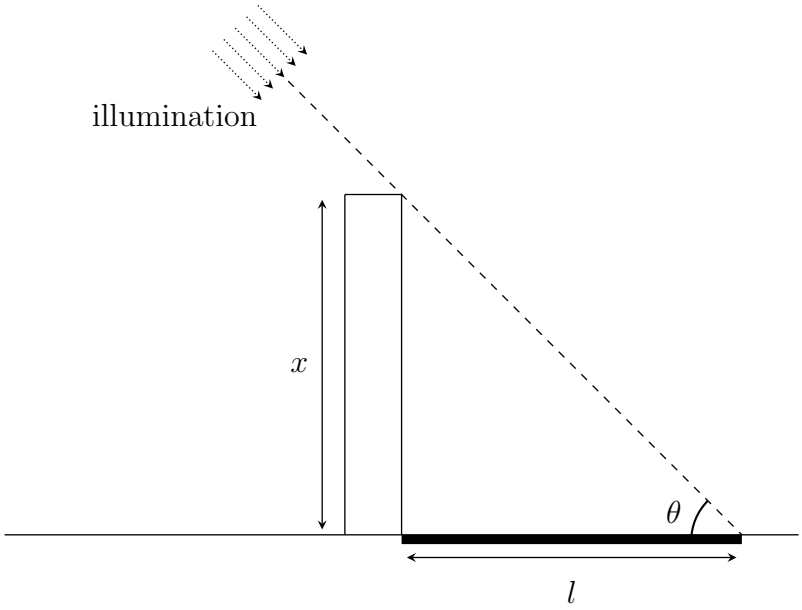

Figure 1.1: The length of a shadow from a tower can be explained by deduction.

components. There are the physical conditions or constraints, $\mathcal{A}$, of the system in question that are to be explained[3]. There are the physical laws, L, which determine the behaviour of the system. Then there is the explanandum, or the phenomena which is to be explained α. In Hempel's D-N account, an explanation of α is equivalent to its prediction from $\mathcal{A}$ acting under L [29]. An objection to this symmetry between prediction and explanation is that an explanation can also be cast as a retrodiction [31]. As a result I will broaden Hempel's definition, such that an explanation is equivalent to a deduction. In this way a logical or mathematical deduction can be written as:

$$L_{\mathcal{A}:\alpha}(\mathcal{A}) = \alpha \tag{1.1.1}$$

where $L_{\mathcal{A}:\alpha}$ is the logical or mathematical operator that is composed of an application of L, which deduces the explanandum α from the conditions $\mathcal{A}$ in question. The operator $L_{\mathcal{A}:\alpha}$ must be dependent on α and $\mathcal{A}$, since changes in the boundary conditions or explanandum demand different explanations even if the laws remain unchanged. The strength of this definition is in the simplicity of the formulation. However there are a number of criticisms of it. In order to examine these, I shall first

[3]Often called boundary conditions.

take an example in which a tower illuminated by a collimated light source (like the sun) casts a shadow on the ground. A diagram of this process is shown in fig. 1.1. In this system the initial conditions are the angle of illumination, the height of the tower x, and that the tower rises perpendicularly from the ground. The governing laws are that light is projected in a straight line, and that the tower is opaque. Using this, one can deduce that the length of the shadow on the ground is $l = x\cot(\theta)$. This value of l constitutes the explanandum.

This example was first used by Bromberger to elucidate a criticism of Hempel's approach [32, pp. 79-105]. In this example the length of the shadow can be explained by reference to the height of the tower, and indeed this can be deduced. However it seems strange to say that the height of the tower is explained by the length of the shadow, even though this can be deduced [30]. However, I perceive this to be a linguistic trap. This is because it seems perfectly reasonable to say that "in this explanatory set-up, what the height of the tower must be is explainable by the length of the shadow and the angle of illumination".

I perceive that this linguistic trap exists because from an everyday perspective, the explanandum "the height of the tower", can in fact be explained in a great number of different ways. Some methods of explanation, perhaps those that appeal to its design and construction, are of much greater interest from the practical perspective of everyday use of the tower than the transient and ephemeral properties of the shadow. As a result one would intuit that if the length of the shadow was invoked in response to the request "please explain the height of the tower", while it might constitute a logically consistent explanation, the response would probably not be met with satisfaction. If however, the purpose of the explanation was to detail how the height of the tower might be measured, this would be very satisfactory.

I believe it is for similar reasons related to satisfaction that Hempel and Oppenheim insisted that the laws that are used in a D-N explanation are general laws. Such an insistence on generality appears to bias a proper explanation towards a reductive conception, in which more general, "true" laws are used to explain specific behaviour.

Such a grounding in terms of the general laws would make an explanation similarly general, and it would be as inviolable as the laws on which it was based. However it is very difficult to find a completely general physical law. For example while one might claim that as a general law "solid gold expands when heated", under certain conditions, for example if it is wedged by a material of a larger thermal coefficient of expansion, the gold would in fact contract [30, p.84]. Instead what is required for an explanation is that the laws invoked are able to describe all the necessary behaviour, of all the necessary states of the system that arise under the conditions of the explanatory set-up. Specifically, the necessity of these requirements relates to the deduction of the explanandum that occurs.

To give an example, when zinc is immersed in sulphuric acid, an exothermic gas-producing reaction occurs. When the explanandum is the answer to "how does the experiment proceed?", physical laws that relate to heat, gas, acid-base reactions and the thermal properties of all the constituents in the reaction are certainly necessary. However, during the explanation the possible nuclear reactions of the zinc nuclei that occur as a result of proton bombardment are not necessary, since although both protons and zinc nuclei are present they never actually undergo nuclear reactions. While they may certainly be included to give a richer understanding of the physical processes present, since they are not necessary for the explanandum, they do not for a requisite part of the explanation.

Since not all systems are purely deterministic, probabilistic systems must be included in an account of explanation. While Hempel did this by a modification of the core of a D-N explanatory account [33], others extend his account in the so-called deductive-statistical account in a way which means the ontic nature of a deduction need not be dropped [34, pp.448-452] [30, pp.172-177]. To make a probabilistic explanation ontic, let us first observe that there are two ways in which a probabilistic occupation of different states can occur in an system. The first way is that the initial conditions are uncertain, this can be accounted for by treating each of the possible initial states as a separately in the deduction. The second way is if the governing laws of the

system are indeterminisitic, such a system can be treated equivalently to the first, with the exception that the number of states that are considered increases each time an indeterministic event occurs. Therefore after every inderministic event the number of different states in the deduction might increase[4]. Regardless of which way the uncertainty arises in the calculation a consistent explanation can still be made, although it may be that certain explanandums like the answer to the request "explain why the uranium nucleus will not decay", are strictly forbidden with respect to the governing laws[5], as they are nonsensical. This makes an account of explanations in certain applied sciences difficult, like an explanation of how a particular person is to blame for an oil disaster [34, pp.448-452]. However, as my work concerns only pure science I do not need to account for these issues.

Under the considerations discussed above, equation 1.1.1 constitutes my definition of an explanation. For philosophers however there is one principle flaw in my definition: I have omitted an account for how an explanation becomes ontological or scientific. But I believe that to place philosophical restrictions on the kind of content that can constitute a scientific explanation is asking for trouble. This is because there are a large variety of methods that different scientific schools of thought use to determine whether an explanation is satisfactory. In particular explanations are often perceived to be valid only on the basis of a large amount of past accumulated literature that may be formed from the work of many people. As a result an explanation often cannot be judged solely on intrinsic merits or failures, but only by reference to the broader literature.

A philosophical account of whether an explanation is scientific or not is therefore likely to be a much larger project[6] that can not be explained or even described in this work. Further my analysis above suggests that the relevant justifications that make

[4]The number of states required to treat the system does not necessarily increase, for example there are some systems like Markov chains in which the state space of the computation may not increase after each indeterministic event.

[5]This explanandum should be rephrased as "explain why the uranium nucleus will *probably* not decay".

[6]To be sure, this is likely an extremely worthwhile and interesting project.

an explanation scientifically satisfactory must already be performed by scientists in the broader scientific literature. Therefore, in this work it will be sufficient to justify each of my explanations as I present my scientific study, in a fashion relevant to the area of study in which the explanation is grounded. With this definition for what constitutes an explanation, I now proceed to discuss a practical definition of emergence.

Definition and discussion

First it is important to note that a realisation of epistemic emergence is dependent on a particular explanation. Of course a scientific explanation must aim to be grounded in a physical system, and in this case the emergence will have important and interesting scientific and ontological import. However because of this dependence historical emergence must be a property of a specific explanatory set-up. This is why a good account of explanation is necessary to detail a new theory of epistemic emergence.

Indeed this approach has historical precedent, for when Hempel and Oppenheim presented their definition of an explanation they also attempted to detail a conception of emergence [29]. The position of the British emergentists, the motivations for which are discussed in chapter 1.1, was that explanandums in an emergent system could not be explained using physical laws that determine the behaviour of the fundamental particles in the system[7]. I interpret this to mean that it is not possible to construct an explanation in the form of equation 1.1.1 using these laws.

However, there are two ways that equation 1.1.1 might fail to be constructed. The first way is that the explanandum is simply incompatible with the initial conditions or the physical laws, as they apply to completely different kinds of system, or because the physical laws are insufficient to determine or predict the behaviour specified in the explanandum. Regardless of whether such a situation is a failure in the

[7]This includes those with different boundary conditions.

explanandum or physical laws, a simpler diagnosis of the failure of explanation will always be that a better explanatory set-up must be sought. The protein folding example of computational emergence is in this category.

The second way is because there is some limitation such that, while the governing laws can be shown to apply to all the behaviour the system can exhibit, it is not possible to detail how the explanandum can be deduced, as the deduction is intractable. This is the more interesting case. The usually occurs through a discussion of the physical laws of the system, when these laws generate a mathematical or deductive intractability. For example this may be caused by a state crossing during the process of an adiabatic continuation. However it may be that such a failure in deduction simply results from a failure in deductive skill, and a further investment in time and ability may solve the problem. Batterman's theory of emergence can be subjected to such a criticism, and indeed he aknowledges it as a valid criticism (although as his is a practical theory he does not feel the criticism carries the philosophical weight others invest in it).

However, I observe that there is another way by which an explanandum cannot be deduced. This is motivated by the observation that many systems have an extremely large state space. In some explanatory set-ups which of these states the system is in is critical. This means that in the explanandum all the different available states must be considered, so the information for each state must be stored. Information requires a physical instantiation and, as the computational emergentists observe, there are physical limits to the information that can be stored even in the entire accessible universe. Therefore there must be some explanatory set-ups for which an explanation cannot be given, since the information required to detail the explanation exceeds the physical constraints which the information must be subject to. Such an explanatory set-up I call historically emergent.

A crucial part of this definition turns on the word 'must'. It is clearly the case that a specific determination in an explanatory set-up will be strongly dependent on the method being used, but some methods require more states to be considered than

others. There are always an absolute minimum number of states that are required in an explanation. These are the number of states that are required[8] to give detail and meaning to the explanandum itself. An example of a method that requires a large number of states to construct an explanation is cyclobutadiene, discussed in chapter 3. The eigenvalue solver method used requires a large number of position states to work, although only a small number of energy eigenstates are really of interest. As a result one finds that the explanatory set-up in cyclobutadiene cannot be considered emergent.

How does this definition of historical emergence aid an understanding of explanation? To address this I will use some thought experiments. To begin with, I will explain why a system each state may need to be explained separately. Let us examine a thought experiment in the form of a card game. The rules of the game are as follows:

I The game is formed of cards, and at the start of the game all the cards are randomly arranged in the deck.

II Players each take turns to draw cards from the deck, which they keep in their hands.

III Players are not allowed to look at the cards until they are drawn.

IV Each card is worth a number of points, and the player with the highest number of points when the deck is empty wins the game.

V On each card are written some additional rules, actions or information that must be followed by the players as soon as they draw the card.

On half of the cards there is the following instruction: “take the top card of the deck and place it outside the game, do not look at the card”. On one of the cards is

[8]In the case where a property is the explanandum, it must be observed that a property needs to be related to a physical state to have a physical instantiation. Note that average properties still only need one state: pressure only needs to be related to a single molecular rebound to have a physical basis even if it is defined as the average of many.

written the rule "This is the winning card. The player who draws this card instantly wins the game and the game ends".

From these rules and the details of the cards, it can be seen that there are two ways the game can end. One way is that one of the players draws the winning card, they win and the game ends. Let us call this the fast way. The second way is that a card is drawn which causes the winning card to be placed outside the game. In this case the players run through the deck, and the game ends. Let us call this the exhaustive way. Now, let us say that after two people have played the game, a friend asks them "who drew the winning card?". As we know all the rules of the game, and all the details of the cards, it is easy for us to work out what the friend means. Likewise if the players finished the game the fast way, they will know how to respond. However if the players finished the game the exhaustive way; there is no answer to give. In this instance the question will not make sense to them, as it will lie outside their experience[9].

What this card game example illustrates is that in some cases an experience of a system or process will be incomplete, and that such a limitation will mean that one is unable to formulate or even understand the goal or purpose of an explanation or experiment. In order for the players to understand the card game, there is a simple solution: they could repeatedly play the game until they find the winning card, and understand the question.

This kind of exploratory thought experiment is common in many theoretical and experimental works; the explanandum of the (thought) experiment is to explain what can happen. This illustrates why in some cases each outcome or state needs to be considered separately for a full explanation to be given. It is because under the conditions of the explanandum the individual states belong to completely different classes and so must be treated separately.

There are also many areas of physical study where experience is necessary to provide

[9]It is implied that the correct answer would be: "no-one drew the winning card".

an explanation. For example all the behaviour in solar cells is based on exactly the same physics: quasiparticle excitation and transfer [35]. The really interesting physics that drives current work in the field refers to properties of the material when it is engineered to improve the efficiency of energy conversion. In order to provide an explanation, first one must know what the state of the system is when it is most efficient. Since this is strongly dependent on the efficiency of charge transfer, it often concerns crystal inclusions, defects, and also the device structure [36].

Although a system that requires experience to understand is one property of an emergent explanatory set-up, this is not unique to emergent explanations. I show this in chapter 4, as in order to study the magnetic order of iron arsenide, it is necessary to first study experimental x-ray diffraction results. Therefore there are other qualities a set-up must also have if it is historically emergent. I will illustrate these with a second thought experiment. I call this the cat box death experiment.This thought experiment is similar to Schrödinger's cat. I place my cat who I will call Theo, in an adiabatic box. In the box I also place the necessary life support equipment. I close the box, and wait for a suitable period of time, perhaps a week. I then open the box to see what happened. However immediately before I place Theo in the box I infect him with special virus. This virus mutates rapidly, so as it spreads inside Theo it has the capacity to mutate into a large variety of different lethal strains. The number of different outcomes of the experiment are vast: depending on which mutation occurs, and at which time and which place in the body this happens, the virus may kill Theo in one of a large number of different ways. It may also be the case that Theo is left permanently debilitated in a particular way, or depending on the precise events, that Theo's body successfully contains the infection so that he feels no ill effects at all.

In the cat box death experiment, a reasonable explanandum to ask for may be to "explain the ways Theo can die". However in this experiment it is likely that there an uncountably large number of different different types of death Theo may suffer. This means that one is unable to detail all the possible outcomes of the experiment.

Worse still it may be vanishingly unlikely that even if one detailed a large range of different ways that Theo may die, none of them would be likely to happen. This means that the whole process of seeking an explanation is a doomed exercise.

However it is important to note that if the experiment was run, and Theo died, it would be possible to explain "how Theo died". One cannot explain how Theo *could* die, but once he has died, one can explain how Theo *did* die. A meaningful account of the death of Theo can therefore only be provided after the event has taken place, and cannot be provided before.

A well known type of physical system that behaves similarly to this thought experiment is the weather. Precise knowledge of weather effects is additionally extremely important, since weather prediction is used to direct scarce resources. However it is not possible to predict weather phenomenon by much more than a week using current methods. In the same way as the cat box death experiment, a reasonable assessment of the weather cannot be made ten days in advance. Instead one must wait and see what happens.

I have shown that a system that hosts an historically emergent explanatory set-up must have certain properties that are relevant to the scientific study of the explanation. One must expect that an experimental result that contributes to the explanandum will be at the very least extremely difficult to repeat. This condition violates one of the expectations of a good scientific experiment, namely that the results are independently verifiable. Also, although an explanation of the entire behaviour of the system is not available, an explanation of how a particular outcome may arise is available. As in general an explanation of a particular result that has occured is at least as relevant, and usually more relevant than the explanation of a random result, an explanation can become important through the occurence of an event. This is the reason I have named this type of emergence "historical emergence".

There is an ambiguity in my definition of historical emergence: the upper limit of the different states that are required in an explanation. As detailed in chapter 1.1.2 there is a phsyical limit to the amount of representable information is limited, and

this could serve as a suitable limit. However in practice a strict upper limit like this on the number of states is not actually required, because past a certain limit of complexity, an explanation loses its appeal. This is because although in reality there are many physical systems in which the outcomes of all the various states are extremely important and must be dealt with separately, resources are always scarce so there will be many systems in which the utility of the results is too small to bother with. One can note that there are likely to be many systems which, although not strictly emergent, are emergent in practice. Once an exhaustive state analysis for these system is ruled out, they become for all intents and purposes historically emergent.

Similar to the determination of whether or not an explanation is scientifically satisfactory discussed at the end of chapter 1.1.3, a philosophical definition of whether or not an explanatory set up is practically emergent is beyond the scope of this work. Instead for the system where I find a system which is emergent in practice, in chapter 5.2, I will detail why a full description of all the different states is inaccessible using considerations related to the system under study and methods being used.

1.2 The method of study: why density functional theory?

While the theory of historical emergence may be consistent, it is important to examine whether any physical systems host historically emergent explanatory set-ups . As I search for such a system, I must provide an account for how my explanations are scientifically *satisfactory*, and how an explanatory set-up is *practically* emergent. In order to do this I will us a consistent method to compare different systems and minimise the quantity of scientific justification that must be given. For these purposes I have chosen density functional theory (DFT).

To detail why I have chosen DFT, let me return to Batterman's theory of emergence.

Regardless of whether or not his is a good theory of emergence, it correctly identifies that it is often very challenging to construct an account of a system's behaviour in terms of processes at the fundamental level. This is important as the theory of historical emergence is indifferent to the theoretical challenges faced in a deduction. In the study of condensed matter systems, the explanandums of interest are related properties of the materials in question. There are two general methods capable of modelling properties in a broad range of systems: wavefunction methods and DFT. In the construction of a particular explanation however, the less complexity that is required the better. It is found that while wavefunction methods are suitable for systems with small numbers of electrons, it is very challenging to model more than around forty electrons due to the exponential scaling properties involved in wavefunction solvers [10, 37].

By comparison DFT is in practice able to calculation many of the same properties. The theory of Hohenberg and Kohn shows that all the properties of a single state, of a many-electron system can be expressed as a function only of the electron density of the state, and the potential that the electrons are in [38]. What this theory implies is that the wavefunction does not need to be calculated at all. This greatly reduces not only the computational overhead in the calculation, but provides an easier way to describe the behaviour of systems in terms of changes only in the electron density [9].

Aside from these explanatory advantages that DFT can offer in our study of applied historical emergence there are other benefits to using DFT. As DFT is a general theory, it can be applied to a wide range of different systems. This means that these different systems can be compared and analysed using the same methodology. Additionally it is a widely used method and there is a great deal of experience and knowledge in the condensed matter physics community around the interpretation of the results of DFT. This means that a discussion of emergence, or a particular instantiation of it, will be understood by much of the scientific community. This is important for the wider discussion of emergence.

1.3 Historical emergence in practice

Limitations of the approach One downside of restricting this work to a single method is that when I study any particular system I must accept all the inadequacies and problems of the method. In particular in chapter 5.2 I conclude that the iron system when calculated using DFT exhibits practical emergence. The method of DFT is an important part of this conclusion. However as long as I remain clear that the "laws" in the explanatory set-up are only related to the physical system via DFT, useful conclusions can still be drawn with an appeal to historical emergence. Whether or not the results of the DFT calculation represent the real physical processes in iron, or only exist due to the approximate treatment should not affect the conclusion, as it is shown that historical emergence is able to inform the analysis of the system. The framework of historical emergence is additionally able to inform and motivate a discussion of alternatives and improvements to the method used, and in such a way inform the process of scientific research.

1.3.1 Summary of the researched physical systems

This work combines philosophical analysis with computation physics research. Since the study is motivated by philosophical considerations, in the process of analysing physical systems there is also the opportunity to improve the methods of study that are applied to research areas that are thought to hold really interesting emergent systems. Additionally I find number of important results about the physical systems which I study.

Cyclobutadiene In chapter 3 I study cyclobutadiene in an effort to understand how different isomeric compounds are related to each other. Chemistry and isomers are thought to host emergent phenomena, as there are a great many different chemical structures with markedly different properties but with the same Hamiltonian [2, pp.146-163]. Cyclobutadiene is a molecule that can transition betwee two rectan-

gular configurations, via a process called automerization. Automerization is similar to chemical reactions, as it involves the motion of nuclei to a different structural conformations. However in automerization the product and reactant in the reaction are identical, and the transition does not require thermal or collision processes as it is permitted by quantum tunnelling [39, 40, 41, 42]. These distinctive qualities of cyclobutadiene means that when one studies this molecule one can study how structure changes when nuclei tunnel, without additional complications such as dynamic molecular collisions.

In order to calculate this nuclear tunnelling, I propose a general method for calculating the energy eigenstates and wavefunctions of nuclei bound in molecules. As the electron energy levels are sufficiently well seperated in energy, I am able to use the Born-Oppenheimer approximation, and use an effective potential energy surface determined by the electrons and Coulombic forces to model the nuclear motion. I use this to calculate the Raman spectrum and molecular wavefunctions using the symmetry-conserving motions permitted under rectangular symmetry. I am able to determine how the nuclear motions for different Raman resonance states affect the rate of tunnelling. I show how the calculation and interpretation of the wavefunction reveals the sensitivity of the system to environmental effects, and how the inclusion of hydrogenic motion affects the carbon motion and the strength of the tunnelling interaction.

As the method I use is based on the wavefunctions and eigenstates, it is not immediately clear how to interpret the 4D wavefunction in a way that yields information about the physical processes. In cyclobutadiene, although the effective internuclear potential energy surface is anharmonic over its entire extent, the potential minima are sufficiently deep and the potential energy surface is harmonic enough, that the typical motions of the model expected from semiclassical models [43, 44] can still be identified in the multidimensional wavefunctions. This is done using specific operators, and in this way these typical motions can be used to explain why different excited states have different tunnelling rates. I also extend the study to symmetry

breaking processes in cyclobutadiene. I do this by considering small symmetry-breaking perturbations, and reasoning the influences that these potentials will have on the tunnelling rates and Raman transition amplitudes. Here I am able to detail how different chemical structures are related to each other through symmetry breaking, and that since the behaviour of these symmetry-broken structures must be explained individually, historical emergence must be present at some level of chemical complexity.

Iron arsenide Many correlated electron systems are thought to be emergent [45, 46], however they are usually under conceptions of emergence like Batterman's as the electrons correlate into states with properties and behaviours that are novel, with respect to the properties of individual electrons. It is therefore of interest to see if historical emergence can inform the behaviour in systems that exhibit electron correlation. In chapter 4 I study iron arsenide. This is a material that displays an elliptic incommensurate helimagnetism that changes with temperature[47], leading to a continuum of magnetic structures with different periodicities. Even if the material does give rise to a historically emergent explanatory set-up, a study might be used to investigate symmetry breaking caused by electron correlation in noncollinear systems, as XRES measurements have found a right-handed chiral state in the material [47].

It has been suggested that the helimagnetic structures results from competing low-energy magnetic states [48]. This helimagnetic structures breaks a number of crystal symmetries. Based on neutron diffraction studies by Frawely et al. [47], I propose a magnetic structure based on local environment and symmetry arguments, in which the magnetic moments canted out of the **a**-**b** plane. I perform DFT calculations on the material, and probe the local Fe atom environment using spin-orbit coupling as a perturbation and a projection of orbitals at the Fermi surface. I use these calculations to justify how the canting may arise in the material.

Based on an analysis of the different spin configurations and their relative energies, I conclude that the magnetism in the system has its origin in a Stoner-type Fermi

surface instability, which must be significantly complicated by correlations in the material. With DFT I also examine the local Fe-potentials for different magnetic states, and these suggest that magnetic order in the system causes a distortion in the crystal lattice positions, similar to that occuring in chromium [49, 50]. There is therefore no reason to expect that iron arsenide can host a historically emergent explanation.

Noncollinear magnetism and spin initialisation In spin polarised DFT calculations there are often a number of different stable spin configurations. While in collinear calculations there are usually relatively few of these, in noncollinear calculations there is the possibility that there are a large number of such states. Such systems would be ideal candidates for historical emergence, due to the multiplicity of different states that they can support. Indeed frustrated systems are one such class of system, and many think that they exhibit emergence, as the large number of competing states leads to complexity, and novel unexpected behaviour [51, 52, 53].

Therefore it is important to implement a method of spin initialisation which can drive the density search algorithm towards a desired spin configuration in NCM calculations. Methods already exist for this purpose [54, 55, 56, 57, 58], however each of these methods may bias the density search algorithms in unexpected or undesired ways. In chapter 5.2 I develop a method of spin initialisation that is designed to avoid these problems, which works by performing rotations of the exchange-correlation potential.

Additionally it is often the case that symmetry is broken in unexpected ways in magnetic systems. Therefore although enforcing symmetry constraints on a particular DFT calculation may reduce the computational load of a calculation (see chapter 2), it is not always desirable. To examine how symmetry-unconstrained DFT calculations behave in magnetic systems, and also to test the spin initialisation method I developed, I perform calculations on elemental iron and manganese oxide.

Calculations on iron show my spin initialisation procedure is able to push the mag-

netic order in systems into particular orientations. They also find that the relaxation of the symmetry conditions allows the density search algorithm to find new low energy magnetic configurations in iron. These configurations are likely stable due to complex interactions between states at the Fermi surface. In real space the interactions appear to be localised in either interstitial electron states, or electron states close to the nuclei. Each of these interactions cause deviations from the lowest energy configuration of a particular symmetries, and by particular energies. This allows the exclusive identification of the interacting states in the calculations. There is an extremely large multiplicity of these different magnetic configurations, all with different energies and density distributions. Since each configuration can be distinctly identified and has a different structure, beyond the broad identification of the interstitial or localised deviations from the ground state it is not practically possible to provide a unified account for the properties of these different configurations. I therefore conclude that Fe hosts a practically historically emergent explanatory set-up, at least in the calculations presented here.

Calculations on manganese oxide showed a bias towards the ferromagnetic spin configuration. This was likely caused by interactions in unstable electronic configurations early in the calculation, before the correct d-shell configuration on the Mn atoms was found by the density search algorithm. The spin initialisation procedure was only partially able to counteract this bias. This was because the magnetic structure and the lack of a Fermi surface, meant the different magnetic states were stable with respect to changes in the exchange correlation potential. This stability however means that other less sensitive spin initialisation procedures could be used in MnO, without fear of causing bias to an undesired magnetic configuration. Finally, as the different magnetic configurations were robust, the relaxation of symmetry constraints did lead to any new states or configurations being found. Manganese oxide does not seem to host any historically emergent explanatory set-up.

1.3.2 Utility of historical emergence

When proposing a new theory of emergence, there is a risk of unintended consequences. By this I mean that there may be a large number of systems that would not normally be considered emergent, and do not really exhibit any of the typical qualities associated with emergence, which nonetheless are technically defined as emergent under the new definition. In the physics research carried out here, I find that of the four physical systems that were investigated, three of them displayed none of the qualities typical to an emergent system, and were also not found to be historically emergent. These are cyclobutadiene in chapter 3, iron arsenide in chapter 4, and manganese oxide in chapter 5.2.

The remaining system, elemental iron in chapter 5.2, was found to display historical emergence. While elemental iron is not typically considered to be an emergent system, the calculations performed did show many of the qualities expected from emergent systems, such as dependent novelty, irreducibility, and unpredictability. Additionally all these were closely related to the historical emergence exhibited in the system. This demonstrates the discerning and effective nature of historical emergence as a definition.

Chapter 2

Method of density functional theory

2.1 Background

Density functional theory has been a remarkably successful and computationally cheap method of estimating the properties of the ground state of quantum systems [59, 60]. The theorem of Hohenberg and Kohn (HK) shows that the energy of the ground state E_{GS} of any electronic system can be represented as a functional of the density. This density corresponds to a global minimum of an energy functional, allowing the state to be found variationally with respect to changes in the density, it is usually expressed as [38]:

$$E_{\mathrm{GS}} = \mathcal{F}[\rho] + \int \mathrm{d}\boldsymbol{r}\rho(\boldsymbol{r})V(\boldsymbol{r}) = \mathcal{T}[\rho] + \mathcal{E}_{\mathrm{xc}}[\rho] + \int \mathrm{d}\boldsymbol{r}\rho(\boldsymbol{r})\left[V(\boldsymbol{r}) + \frac{1}{2}V_{\mathrm{H}}[\rho](\boldsymbol{r})\right], \quad (2.1.1)$$

where $V(\boldsymbol{r})$ is the potential supplied by the nuclei, $\rho(\boldsymbol{r})$ is the ground state electron density, and the HK functional $\mathcal{F}[\rho]$ is arbitrarily divided into the kinetic energy functional $\mathcal{T}[\rho]$, the exchange and correlation functional $\mathcal{E}_{\mathrm{xc}}[\rho]$, and the inter-electronic Hartree potential $V_{\mathrm{H}}[\rho](\boldsymbol{r})$. However although such a functional is proven to exist in principle, the form is unknown and DFT calculations have to use approximations instead. It seems from early work that an important term to capture accurately

is the large contribution from the kinetic energy, since early attempts such as the Thomas-Fermi approximation [61] do not match well to experiments [62, 63] and these have been largely replaced by the Kohn-Sham (KS) orbitals technique discussed below. DFT-HK Kohn and Sham showed that decomposition of the density into single-particle like orbitals is mathematically equivalent provided that the correct orbital functionals are employed [64]. The orbitals ψ_i are chosen such that

$$\rho(\boldsymbol{r}) = \sum_{i}^{N} \psi_i^*(\boldsymbol{r})\psi_i(\boldsymbol{r}), \tag{2.1.2}$$

where the sum is over all orbitals N. This relationship between the KS wavefunctions and the density leads to a relationship between the KS wavefunctions and the density functional, and this arises because the energy $E_{\mathrm{GS}}[\rho]$ is minimised for the choice of the ground state density $\rho(\boldsymbol{r})$ [9, p. 123]. Formally speaking, under an infinitesimal change in the ground state density $\rho(\boldsymbol{r}) \to \rho(\boldsymbol{r}) + \delta\rho(\boldsymbol{r})$, if one places the constraint that electron number must be conserved then

$$\int \mathrm{d}\boldsymbol{r}\delta\rho(\boldsymbol{r}) = 0. \tag{2.1.3}$$

Due to the variational principle the energy of the system in the energy of the extremal ground state is unchanged under the infinitesimal variations of $\delta\rho(\boldsymbol{r})$. One can perform the same procedure for each of the KS wavefunctions. In the same way one can vary wavefunction $\psi_i(\boldsymbol{r})$ by $\delta\psi_i(\boldsymbol{r})$ so that

$$\delta\rho(\boldsymbol{r}) = \delta\psi_i(\boldsymbol{r})\psi_i^*(\boldsymbol{r}) + \delta\psi_i^*(\boldsymbol{r})\psi_i(\boldsymbol{r}). \tag{2.1.4}$$

The ψ_i are complex, and this means that variations in the phase of ψ_i will leave $\rho(\boldsymbol{r})$ unchanged. For this reason variations in $\delta\psi_i(\boldsymbol{r})$ will be constrained so that $\delta\psi_i^*(\boldsymbol{r})\psi_i(\boldsymbol{r})$ is real. One thus obtains

$$\delta\rho(\boldsymbol{r}) = 2\delta\psi_i(\boldsymbol{r})\psi_i^*(\boldsymbol{r}). \tag{2.1.5}$$

If one enforces the same constraint specified in equation 2.1.3, it must necessarily

be the case that

$$\int \mathrm{d}\boldsymbol{r}\delta\rho\frac{\delta\psi_i}{\delta\rho}\frac{\delta E_{\mathrm{GS}}}{\delta\psi_i} = 0, \tag{2.1.6}$$

This variation can be rewritten as

$$\int \mathrm{d}\boldsymbol{r}\delta\psi_i\frac{\delta E_{\mathrm{GS}}}{\delta\psi_i} = 0. \tag{2.1.7}$$

so that

$$\int \mathrm{d}\boldsymbol{r}\frac{\delta\rho}{\psi_i^*}\frac{\partial E_{\mathrm{GS}}}{\partial\psi_i} = 0. \tag{2.1.8}$$

However since our choice in the variation $\delta\psi_i$ and by extension the variation $\delta\rho$ is arbitrary with respect to $\boldsymbol{r}$, for equations 2.1.3 and 2.1.8 to both be satisfied

$$\frac{\partial E_{\mathrm{GS}}[\rho]}{\partial\psi_i^*(\boldsymbol{r})} = \epsilon_i\psi_i(\boldsymbol{r}), \tag{2.1.9}$$

where ϵ_i is the energy of orbital ψ_i. These ϵ_i can be used to help calculate the energy of the system, since they completely account for the first order response of the system to changes in ρ

$$E_{\mathrm{GS}}[\rho] = \sum_i^N \psi_i^*\epsilon_i\psi_i + E_{\mathrm{remainder}}[\rho], \tag{2.1.10}$$

where

$$\frac{\delta E_{\mathrm{remainder}}[\rho]}{\delta\rho} \equiv 0 \tag{2.1.11}$$

for any $\delta\rho$, even those that do not conserve electron density.

It is not immediately clear how to calculate these ϵ_i, which are clearly dependent on the number of electrons and the external potential. In addition there is no guarantee for the uniqueness of the ψ_i and ϵ_i. However Kohn and Sham observed that for the particular model problem of the noninteracting electron system, this orbital decomposition of the density was mathematically equivalent to a fully quantum mechanical calculation. They reasoned that since this formulation was able to calculate the kinetic energy in an noninteracting system, non-interacting orbitals ψ_i could be used to approximate the kinetic energy of interacting electrons[65].

Motivated by this they developed the local density approximation (LDA). This

calculates the energy of the system by reference to the interacting homogeneous electron gas (HEG), which is exactly solvable using Monte-Carlo techniques [66]. An orbital energy operator is constructed as

$$\epsilon_i \psi_i = \mathcal{H}\psi_i = \left(\frac{\hbar^2}{2m_\mathrm{e}} \nabla^2 + V_\mathrm{xc}\left[\rho\right](\boldsymbol{r}) + V_\mathrm{H,n}(\boldsymbol{r}) \right) \psi_i \tag{2.1.12}$$

where $V_\mathrm{H,n}(\boldsymbol{r}) = V_\mathrm{H}(\boldsymbol{r}) + V(\boldsymbol{r})$, the sum of the Hartree and external potentials, and V_xc is the potential term due to exchange and correlation. The orbitals are also set to obey the orthogonality condition, required by noninteracting electrons, and are occupied in such a way that leads to the correct total number of electrons with the lowest possible energy, and the phases of the orbitals must minimize the energy of the entire orbital system, as in the noninteracting electron case. This framework provides sufficient means to deduce the properties and values of $\mathcal{E}_\mathrm{xc}$ and $E_\mathrm{remainder}$, such that in the jellium case the calculated energy is calculated exactly (or as accurately as the original Monte-Carlo calculations).

From this treatment of LDA it seems that the orbitals chosen, although corresponding to the orbitals of a non-interacting system lack physical interpretation aside from their collective properties (i.e. density and energy). However, the orbital energies (and their "bandstructure") are extremely useful in explaining physical properties of the material. This is because in periodic crystals, the energies and densities of the highest occupied state and the lowest unoccupied state can be determined from the KS orbitals. This was shown by Janak [67], and the argument runs that upon a small change in the electron density, perhaps corresponding to the addition or removal of a single electron in the entire crystal, the system will remain in a ground state and will be similarly determinable using the ground state density functional E_GS. Since the addition is so small, the density and overall energy change will be negligible and the orbital structure will remain broadly unaffected. The distribution of changes in density and energy will therefore be representative of a 'quasiparticle' moving through the system, meaning DFT should be able to accurately predict band gaps.

2.2 Implementation

DFT can represent both molecular and periodic systems, however while isolated molecular systems have only a finite number of electrons, periodic systems are infinite. Therefore in order to accommodate this calculations make use of the periodic symmetry. To do this, each of the KS orbitals has a Bloch translation eigenvalue $\alpha_{\boldsymbol{k}}$ [9, pp. 85-90]:

$$\psi_{i,\boldsymbol{k}}(\boldsymbol{r}+\boldsymbol{a}) = \alpha_{\boldsymbol{k}}^{\boldsymbol{a}\cdot\boldsymbol{k}}\psi_{i,\boldsymbol{k}}(\boldsymbol{r}). \tag{2.2.1}$$

Since these $\psi_{i,\boldsymbol{k}}$ are necessarily orthogonal over the entire extent of the crystal, the number of states that must be orthogonalized in the calculation is greatly reduced.

However in this transformation it is important to note that $\boldsymbol{k}$ can vary continuously, so that technically there are still an infinite number of KS states to deal with. However in practice the energies of the orbitals given in equation 2.1.12 also change continuously, and so an effective calculation can be performed in which reciprocal space in $\boldsymbol{k}$ is discretised into cells, each cell being modelled by a single set of KS orbitals with a set value of $\boldsymbol{k}$ chosen for each cell. As the KS orbitals of each material are different, the spacing of these cells therefore needs to be at least some some minimum value for the material to be modelled accurately. In all the calculations used here, the cells are divided up using a Monkhorst-Pack (MP) grid, in which each cell is a cuboid in reciprocal space [68]. In addition to the periodic symmetry, space group symmetry operations of the crystal can all be utilised to reduce computation considerably. If under the space group symmetry two k-points are equivalent, only one of them needs to be calculated, thus allowing a further reduction in computational load.

Due to the discretisation of reciprocal space and the reduction of symmetry, the density is calculated as the sum of the occupied states over the irreducible Brillouin zone (IBZ) [9]:

$$\rho(\boldsymbol{r}) = \sum_{k}^{\text{IBZ}} \sum_{i}^{\text{occ}} w_{k,i}\psi_{k,i}(\boldsymbol{r})\psi_{k,i}^{*}(\boldsymbol{r}), \tag{2.2.2}$$

where second sum is over the occupied orbitals i at k, and $w_{k,i}$ is a weighting function, which is used to account for the kpoints 'doubled-up' via symmetry operations.

2.2.1 Plane wave basis set, and pseudopotentials

The KS orbitals are computed as solutions to the noninteracting electron problem. This problem can be effectively solved through the use of a basis set. The choice of this basis set is one of the most important factors in the speed at which the solution is found, and the precision of the results. For the purposes of this thesis, I will use the plane wave basis set. The benefit of this basis is that it is easy to construct an orthogonal basis set, and it is effective at modelling the electrons between nuclei that form the bond structures. However, there are significant problems with the use of a plane wave basis set to represent both these interstital electrons and the electrons near to the nuclei, as in these regions the wavefunction varies rapidly. This requires the plane waves used to have a large range in frequencies, and greatly increases the cost of the computation.

It is observed that in most materials the electronic structure closest to the nuclei is largely unchanged between the free atomic case and that situation found in materials, and so hardly contributes at all to the important physical properties of the material. This means that the precise structure of the wavefunction near the nucleus is actually unimportant for most material properties. One defines two regions in a material, these core regions around nuclei where the KS orbitals are largely unchanged, and the interstitial regions. The core regions do not contribute much to the material properties. Therefore in order to model the material effectively, only the interstitial orbitals need to be calculated, as long as the phase and amplitudes of the wavefunction near the boundary between the core and interstitial regions. For these reasons pseudopotentials, potentials that mimic the behaviour of the true atomic potential to obtain the same phase and amplitude relations, are used. In the plane wave basis set this is implemented in a particular way. When the plane wave

interacts with the atomic potential, it scatters. These scattering amplitudes are invariant to changes of the phase in increments of 2π, and so a good pseudopotential is as weak as possible as this minimises the maximum energy of the plane waves that must be used in the calculation, but still reflects the correct boundary conditions between the interstitial and core regions [9, Ch. 11].

Additionally in the use of pseudopotentials, the atomic orbital states are separated into core and valence states, the core electrons represent the low energy electrons that are resistant to perturbations typical to material binding energies, and so they do not play a role in material properties.

While it is possible to construct a pseudopotential that gives a good fit with experimental data, in modern implementations it is more common to use an ab-initio calculation as the basis for determining the pseudopotential. It is most common to fit the pseudopotential to the KS wavefunctions and their phase shifts in the free atom, and then to use this pseudopotential in a full material calculation. However this brings up the issue of transferability, as the atomic environment is different to the environment experienced in other materials. This means that pseudopotentials have a limited range of applicability and the right pseudopotential must be chosen for the problem at hand.

Additionally there are a number of methods that can be used to construct pseudopotentials to deal with the difficulties of transferability and computational load. Two common ones that are used in this work are norm-conserving and ultrasoft pseudopotentials and these are discussed below. The use of the pseudopotential is able to reduce the size of the basis set. However the basis set size used depends both on the material in question and the chosen pseudopotential. As a result this needs to be optimised for the purposes of the calculation being performed.

2.2.2 Norm-conserving pseudopotentials

In general pseudopotentials may be inaccurate. This is because pseudopotentials are usually transferred between systems. In this transfer while the wavefunctions and density near the nucleus remains mostly unchanged in the all-electron case, in the pseudopotential case this is no longer guaranteed and this means that the wrong amplitude and phase differences will be used in the calculation.This is especially important when an atomic system is used to generate a pseudopotential, since the atomic and material environments can be very different.

However mathematical study of pseudopotentials determined that if the electron density in the region of the pseudopotential was equal for both the fully determined system and the pseudopotential system, the scattering phase shifts for both systems display the same perturbation response to a linear order [69, 70]. This constraint is called the norm-conservation condition. Satisfying it ensures that the pseudopotential is more transferable, as it they are better able to model systems which are dissimilar to the free atomic case case, than those that are not norm conserving.

2.2.3 Ultrasoft pseudopotentials

Satisfying the norm-conservation condition often does not allow the pseudopotential to be much softer than the original all-electron atomic potential, even after core and valence state separation are taken into account [71]. This has led to the devolopment of ultrasoft pseudopotentials. The wavefunctions of these pseudopotentials are not strictly norm-conserving, but the pseudopotential is constructed in a way that they satisfy the same conditions [71, 72]. This is possible as long as the pseudopotential is able to replicate not only the phase properties of the occupied wavefunction states in the KS formulation, but also the energies of the unoccupied states.

This condition is less restrictive than the norm-conservation condition, and allows the choice of a softer pseudopotential. An ultrasoft pseudopotential can be constructed in a consistent way by defining a new auxiliary function. Before detailing the

pseudopotential method, it is useful to observe that a set of modified functions β_s are often used in the implementation of DFT, it is defined as:

$$|\beta_s\rangle = \sum_{s'} \frac{(\epsilon_s - \mathcal{H}_{\text{loc}}^{\text{PS}})\,|\psi_s^{\text{PS}}\rangle}{\langle\psi_s^{\text{PS}}|(\epsilon_s - \mathcal{H}_{\text{loc}}^{\text{PS}})|\psi_{s'}^{\text{PS}}\rangle}. \tag{2.2.3}$$

where $\mathcal{H}_{\text{loc}}^{\text{PS}}$ is the Hamiltonian modified to include a pseudopotential which has the eigenfunctions $\psi_s^{\text{PS}}(r)$ and eigenvalues ϵ_s, and the sum is over all the eigenfunctions used in the calculation. Through this definition in norm-conserving pseudopotentials, the nonlocal part of the pseudopotential can be efficiently represented using these modified functions, since when the correct eigenvalues are found $(\epsilon_s - \mathcal{H}_{\text{loc}}^{\text{PS}})\,|\psi_s^{\text{PS}}\rangle = \delta\hat{V}\,|\psi_s^{\text{PS}}\rangle$, where $\delta\hat{V}$ is the nonlocal part of the pseudopotential.

Now let us move on to a description of how an ultrasoft pseudopotential is constructed. If one assumes radial symmetry about the nucleus, the auxiliary functions $\Delta Q_{s,s'}$ are defined as:

$$\Delta Q_{s,s'} = \int_0^{R_c} \mathrm{d}r \left[r^2\psi_s(r)\psi_{s'}^*(r) - r^2\psi_s^{\text{PS}}(r)\psi_{s'}^{*\text{PS}}(r)\right] \tag{2.2.4}$$

where $\psi_s(r)$ is the wavefunction of energy level s in the all-electron case, r is the radial distance from the nucleus, and R_c is the cutoff radius of the pseudopotential. This auxiliary function is the charge density difference between the pseudopotential eigenfunctions and the all-electron eigenfunctions. It is included in the generalised eigenvalue equation as an overlap operator $\hat{S}$, where

$$\hat{S} = \mathbf{I} + \sum_{s,s'} \Delta Q_{s,s'}\,|\beta_s\rangle\,\langle\beta_{s'}|\,. \tag{2.2.5}$$

With this overlap operator, the generalised eigenvalue equation is modified to become [71, 72]

$$\left[\mathcal{H} - \epsilon_s\hat{S}\right]|\psi_s^{\text{PS}}\rangle = 0. \tag{2.2.6}$$

However it is important to note that the addition of $\hat{S}$ to this equation now means that the β functions defined in equation 2.2.3 can no longer be used in a straightforward manner to represent the application of the non-local part of the pseudopotential.

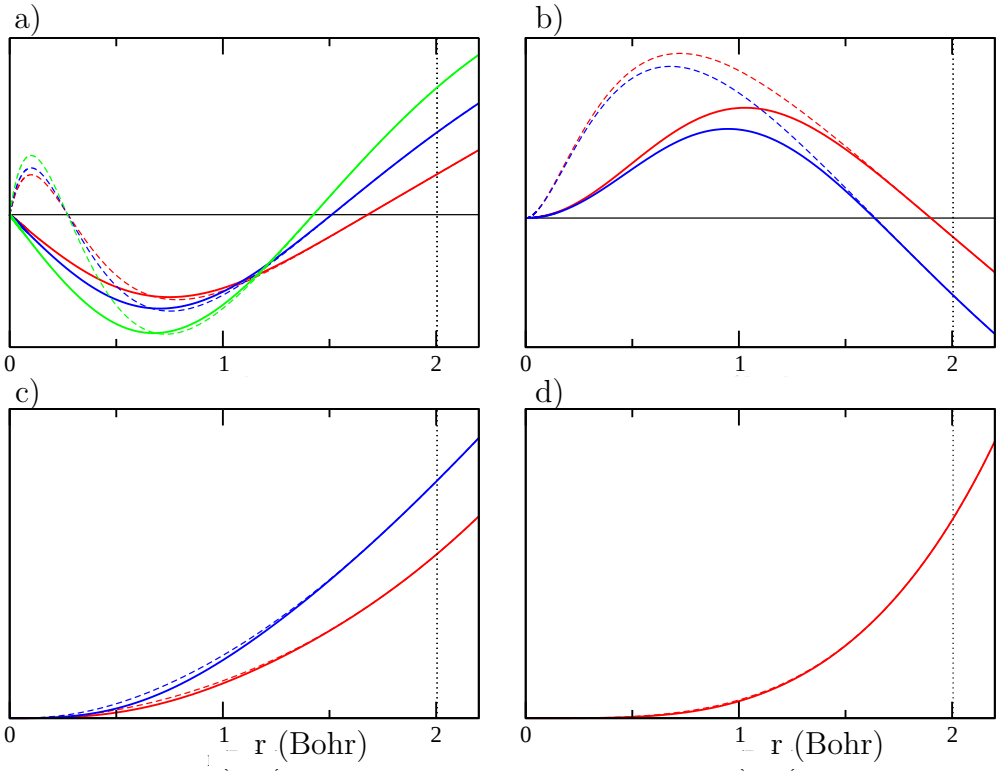

Figure 2.1: Ultrasoft pseudopotential used for oxygen in chapter 5.2. $1s^2$ orbitals are taken to be core. a) s- b) p- c) d- d) f- orbitals. Dashed lines are all-electron wavefunctions, bold lines are pseudopotential wavefunctions. Red lines are the ground state wavefunctions, and blue then green are the wavefunctions for fractionally occupied excited states.

Instead the modified application must include the use of the overlap operator, since

$$(\epsilon_s \hat{S} - \mathcal{H}_{\text{loc}}^{\text{PS}}) \, |\psi_s^{\text{PS}}\rangle = \delta\hat{V} \, |\psi_s^{\text{PS}}\rangle \, . \tag{2.2.7}$$

As a result the inclusion of the overlap operator and the requirement to calculate unoccupied eigenvalues and their eigenstates leads to increased computational cost. What is most important is then the computational load, and whether a consideration of the many plane waves required for norm-conserving pseudopotentials is more cumbersome than that required for ultrasofts. In practice it is most often the case that ultrasofts are preferable, as with modern eigenvalue solvers reducing the basis set causes the largest gains in reducing computational burden [73]. An example pseudopotential can be seen in figure 2.1.

2.2.4 Search for the density

In any implementation it is important to find the density distribution of the ground state of the system. This is not immediately trivial since the KS system is a coupled system of KS wavefunctions and density. There are a number of ways of finding the lowest energy state. One is the method of density mixing (DM) [74]. This method observes that in the ground state the KS wavefunctions and the density are self consistent, but in intermediate density configurations, the KS wavefunctions commensurate to that density's potential do not have to produce a consistent density distribution. This inconsistency can then be used to rapidly guide a calculation towards the lowest energy density configuration. Formally speaking, the self-consistency of the jth calculation iteration is calculated using equations 2.1.2 and 2.1.12, so that from some initial density ρ_j, the KS wavefunctions $\psi'_{j,i}$ are

$$\epsilon'_{j,i}\psi'_{j,i}(\boldsymbol{r}) = \left(\hat{T} + X_{\mathrm{xc}}[\rho_j] + \hat{V}\right)\psi'_{j,i}(\boldsymbol{r}), \tag{2.2.8}$$

where $\psi'_{j,i}$ have been solved self-consistently and othogonalised over i. One can calculate the density of these new KS wavefunctions as

$$\rho'_j = \sum_i \alpha_{j,i}\psi'^{*}_{j,i}\psi'_{j,i}, \tag{2.2.9}$$

where $\alpha_{j,i}$ are the occupancies of the orbitals, usually calculated with the standard Fermi-Dirac statistics. This allows us to calculate the discrepancy between the initial density and the resultant density Δ_j, where

$$\Delta_j = \int \mathrm{d}\boldsymbol{r}\left|\rho'_j - \rho_j\right|. \tag{2.2.10}$$

The value of Δ_j can then be used to determine how close ρ_j is to the correct ground state density. From these Δ_j and the density distributions, a new ρ for the next iteration in the calculation is generated. Providing a good weighting function is used for the Δ_j's, this can often lead to rapid convergence of a DFT calculation onto the desired state [75, 76].

However the method of density mixing can notably fail in certain systems, such as those where the wavefunction naturally changes quite rapidly in response to small variations in the density. This is is often the case in conductors, in which the static response is necessarily non-zero. This behaviour is known as charge sloshing. While there are a number of ways to dampen this behaviour based different algorithms [74], but for some systems it is more effective to use a different density search method.

One such method is ensemble density functional theory (EDFT) [77]. This method works first by using a projected functional, in which the occupancy of the orbitals is determined as the functional is calculated. Minimisation of the projected functional $G[\psi_i]$ is equivalent to the minimisation of the original density functional, but it lifts the dependence on occupation and on unitary rotations of the wavefunction in hte minimizer. The algorithm involves the construction of two iteration loops. In the inner loop, for a choice of KS orbital wavefunctions, the charge density and orbital occupations are successively updated until the energy has been minimized. This constitutes a calculation of $G[\psi_{j,i}]$, on the jth iteration of this outer loop. In the outer loop the gradients of $G[\psi_{j,i}]$ with respect to $\psi_{j,i}$ are calculated, and these are used to generate the wavefunction $\psi_{j+1,i}$ for the next iteration. These gradients $G_{j,i}$ are computed as [77].

$$G_{j,i} = \left(\hat{T} + \hat{V}_{\mathrm{xc}}[\rho'_j] + \hat{V}_{\mathrm{H,n}}\right)\psi_{j,i} \tag{2.2.11}$$

where ρ'_j is the density found from the result of the inner loop. To generate the wavefuntion $\psi_{j+1,i}$, trial steps are taken in the direction of $G_{j,i}$ which are calculated over successive repeats of the inner loop, until the minimum energy in that direction has been determined. As this algorithm is variational, it is much more consistent in its convergence. However this consistency comes at a significantly higher computational cost.

2.3 Spin polarization in DFT

DFT can be extended to include spin polarisations. There are two types of calculation that include spin terms: collinear [78] and noncollinear [79, 80]. These both require different considerations.

Collinear In a collinear system, all magnetic polarization is aligned along a single axis. As a result in these systems in the noninteracting system of electrons in the Kohn-Sham Hamiltonian, it is possible to separate the electrons into two subsystems, one each for up and down [78]. In this way there are two coupled systems, one each for spin up and down, which have the form in equation 2.1.12. The mutual interaction between these systems is mediated by the exchange-correlation potential, which has the form $\mathcal{E}^{\text{charge}}[\rho_\uparrow, \rho_\downarrow] \pm \mathcal{E}^{\text{spin}}[\rho_\uparrow, \rho_\downarrow]$, where the second term uses the positive for the spin up system and the negative for the spin down system. In this work two correlation functions are used, the local spin density approximation [81], and the generalised gradient approximation [82].

Noncollinear spin polarisation In the noncollinear case, the noninteracting electrons need to be treated using spinor wavefunctions as in quantum electrodynamics [83, 56]. In the same way, the spin polarization is extracted from the spinor wavefunctions Ψ_j using the spin-half Pauli matrices $\boldsymbol{\sigma}_i$. In this way the spin polarisation in direction $i = \boldsymbol{x}, \boldsymbol{y}, \boldsymbol{z}$ is

$$\rho_i^{\text{SP}}(\boldsymbol{r}) = \sum_j \Psi_j^\dagger(\boldsymbol{r}) \boldsymbol{\sigma}_i \Psi_j(\boldsymbol{r}) \tag{2.3.1}$$

and the charge density is

$$\rho_{\text{C}}(\boldsymbol{r}) = \sum_j \Psi_j^\dagger(\boldsymbol{r}) \Psi_j(\boldsymbol{r}). \tag{2.3.2}$$

The governing KS equations remain unchanged in their form, and the spin-dependent exchange-correlation potential is also applied to the system through the use of Pauli spinor matrices. In the case of LSDA, for a spin polarisation density $\boldsymbol{\rho}_\sigma(\boldsymbol{r})$ and

charge density $\rho_{\mathrm{C}}(\boldsymbol{r})$ the exchange-correlation energy in the NCM case $\mathcal{E}_{\mathrm{LSDA}}^{\mathrm{NCM}}$, is given by

$$\begin{aligned}\mathbf{V}_{\mathrm{LSDA}}^{\mathrm{NCM}}(\boldsymbol{\rho}_\sigma(\boldsymbol{r}),\rho_{\mathrm{C}}(\boldsymbol{r})) =&\mathbf{V}_{\mathrm{LSDA}}^{\mathrm{spin}}(|\boldsymbol{\rho}_\sigma(\boldsymbol{r})|,\rho_{\mathrm{C}}(\boldsymbol{r}))\sum_i^{\boldsymbol{x},\boldsymbol{y},\boldsymbol{z}}\left[\hat{\boldsymbol{\rho}}_\sigma(\boldsymbol{r})\cdot\hat{\boldsymbol{i}}\right]\boldsymbol{\sigma}_i\\ &+\mathbf{V}_{\mathrm{LSDA}}^{\mathrm{charge}}(|\boldsymbol{\rho}_\sigma(\boldsymbol{r})|,\rho_{\mathrm{C}}(\boldsymbol{r}))\mathbf{I}.\end{aligned} \tag{2.3.3}$$

Here $\mathbf{V}_{\mathrm{LSDA}}^{\mathrm{spin}}$ and $\mathbf{V}_{\mathrm{LSDA}}^{\mathrm{charge}}$ are the spin and charge contributions of exchange correlation contribution, $\mathbf{I}$ is the identity, and $\hat{\boldsymbol{\rho}}$ is the normalised density vector [79].

Extensions of the LDA coefficient are available for the PBE exchange-correlation coefficient, except that since PBE is dependent on the gradient of the spin-density, $\mathcal{E}_{\mathrm{PBE}}^{\mathrm{spin}}$ is a function of the spin polarization $\boldsymbol{\rho}_\sigma(\boldsymbol{r})$ instead of the absolute value of the spin polarisation $|\boldsymbol{\rho}_\sigma(\boldsymbol{r})|$ [80]. This straightforwardly reduces to the collinear case, when all the spin is aligned in the $\boldsymbol{z}$-direction. In the general case the KS equations are therefore

$$\left((-\nabla^2+V_{H,n}(\boldsymbol{r}))\mathbf{I}+\mathbf{V}_{\mathrm{xc}}^{\mathrm{NCM}}\right)\Psi_j=\epsilon_j\Psi_j. \tag{2.3.4}$$

2.4 Determining parameter convergence in DFT

There are two parameters which need to be addressed in the calculation of periodic system using DFT. One is the plane wave energy cutoff, another is the spacing of the MP grid points.

These paramaters need to be tuned to at least a minimum value for the properties and behaviour of the system to be accurately calculated. However due to the pseudopotential method, the core orbitals in the pseudopotential often continue to respond to changes in the parameters even past the effective minimum value. This means that total energy is not necessarily a good indicator of the sorts of properties one may be interested in. Instead the value of each of the significant properties must be independently converged. In order to do this, I have constructed a measure for the value of convergence. For the systems I will study, I will be comparing different

states. The relevant quantity will therefore be the energy difference between these two states, calculated as

$$E'(x) = E_1(x) - E_0(x) \tag{2.4.1}$$

where $E_1(x), E_0(x)$ are the energies of the states of interest, as a function of the paramater of study x. As $x \to \infty$, $E'(x) \to E$, where E is the true value of the energy difference. One can express the fractional convergence of the energy towards the true energy difference by

$$\text{convergence fraction} = \frac{E'(x) - E}{E} = \frac{\Delta E(x)}{E}. \tag{2.4.2}$$

However, in practice it is not actually possible to determine E, as a result E must be estimated from a highly converged calculation instead. When this convergence fraction reaches a small enough quantity for the purposes of the study, then the value of the parameter x required for the calculation is known.

In addition to periodic systems, isolated systems can also be calculated. To calculate such systems using the same method, only one point is requied in the MP grid. However, in order to truly model the system as isolated, a large amount of empty space needs to be included in the effective unit cell of the system, to space out the electrons in successive unit cells. In chapter 3 the molecular system cyclobutadiene is modelled. In this process, the empty space needs to be converged using the method above as well.

2.5 Computer code resources used

DFT outputs are necessarily three-dimensional. Fortunately a large number of 3-d visualisation packages are readily available. Two packages, blender [84] and xcrysden [85] were used in this study, in the projection of density isosurfaces into the unit cell, and of the Fermi surface into the Brillouin zone.

Additionally a number of surface plots and standard 2-dimensional graphs were required. These used the gnuplot package [86].

Finally the CASTEP codebase was both modifed and used in order to perform the DFT calculations presented here [87].

Chapter 3

Emergence in chemical structure: cyclobutadiene

3.1 Introduction

The motions and locations of nuclei underpin how we define molecular structure, structural transitions, and chemical reactions. However these chemical structures do not obviously appear as objects in the many-body quantum mechanical wavefunction or Hamiltonian. It is therefore important to give an account for how quantum mechanics informs these chemical structures and their reactions. Of particular interest for my purposes is that a multiplicity of different isomers can often be formed from a fixed set of atoms. Indeed this behaviour has motivated others call chemical structures emergent [2, pp.146-163]. For the purposes of historical emergence, this seems a fruitful area. This is because different isomers can have very different properties like example reactivity, catalytic activity, or thermodynamic behaviour, that are most commonly explained using individual chemical structures rather than solely by recourse to the governing Hamiltonian. What is not necessarily clear is how these different structures are related to each other at a quantum mechanical level. If each of these structures are simple extensions or modifications of each other, it might be possible to combine the behaviour of isomers in a general way, and dilute

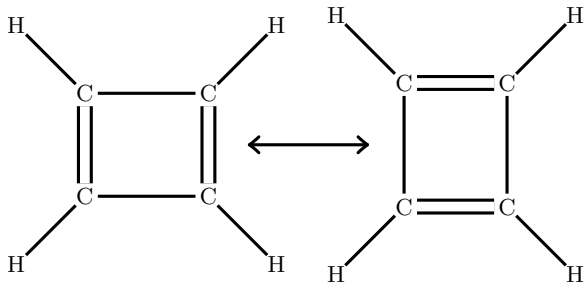

Figure 3.1: The structure of cyclobutadiene and the process of automerisation.

any expectations of historical emergence.

Cyclobutadiene as a free molecule exhibits nuclear delocalization that determines the point group symmetry, for although the lowest-energy electronic configuration suggests that the molecule is rectangular with two double and two single bonds, the molecule automerizes via nuclear tunnelling which results in an overall square symmetry [88, 89]. This process is shown in figure 3.1 A study of cyclobutadiene will therefore allow us to examine the relationship between molecular structure and the underlying quantum mechanics, to examine how in quantum mechanics the relationship between the two different structural conformations of the ring is mediated.

This system converts between the two rectangular configurations, via a process called automerization. This automerization is similar to a reaction, since it involves the motion of nuclei to a different structural conformation. However it is a process distinct from chemical reactions since the reactant is chemically identical to the product, and the transition does not require thermal or collision processes. These qualities therefore present an opportunity to study how structure changes when nuclei tunnel, without additional complications such as dynamic molecular collisions. Here I calculate the energy eigenstates of the nuclear motion that correspond to active infra-red (IR) excitations, and their corresponding nuclear wavefunctions. With these wavefunctions I am able to describe and explain how the different motions of the molecule can enhance or suppress the rate of tunnelling.

There are two electronic configurations at low energies in cyclobutadiene, a singlet

state and an antiaromatic triplet state [90]. Historically it was unclear which state was most important in the low temperature behaviour of cyclobutadiene [91]. While it was found that the singlet state has the lowest energy [92, 90], the electronic structure of the triplet state remains of considerable interest due to conflicting accounts of the aromatic stabilization or antiaromatic destabilization, and the role of ring strain in the electronic structure [93, 94, 95, 96]. At low temperatures the molecule tunnels between two singlet configurations [97, 98], and theoretical studies of the automerization between the two rectangular configurations suggest that the triplet state may determine the effective height of the reaction barrier [99, 42, 100]. However the precise structural conformation where the energies of the singlet and triplet state are equivalent is not precisely known [101], if it exists at all [41, 102]. Additionally in the free molecule the strength of the spin-orbit interaction, which permits a transition between the singlet and triplet states, is small by comparison to the kinetic energy of the nuclei [103], and this will suppress the transition between the singlet and triplet configurations. In this work, we therefore assume that singlet-triplet transitions are symmetry-forbidden, so only the singlet state will be considered.

Some theoretical studies of tunnelling in the singlet ground state focus on the energetic surface and barrier height of this nuclear tunnelling process, as these are required to calculate the tunnelling rate [39, 40, 41, 42]. In chemical systems, the most straightforward approaches to calculate tunnelling rates use WKB(J) formalism [100, 104, 105], however this formalism requires that reverse-tunnelling processes are negligible. There is therefore reason to doubt its applicability to the case of cyclobutadiene where the two configurations are symmetry-equivalent and reverse tunnelling can readily occur. Another common method of calculating rates uses instantons[106], which can be used to map the system onto a one-dimensional tunnelling problem [107, 108]. However as the nuclear potential is anharmonic in cyclobutadiene it is likely that an instanton-based model will not be able to accurately reproduce the tunnelling rate and other properties, such as the motion of the hydrogen nuclei, which is dependent on wavefunction configurations different from

those on the instanton path.

Other work focuses on the prediction of the Raman spectrum of the molecule, which is important to recognise and classify the experimental Raman response of the molecule [109, 110]. However due to time evolution's dependency on the Hamiltonian, the calculations of the Raman spectrum and the tunnelling rate in this single-molecule system are equivalent, and it is possible to study the system under a single framework [109, 88]. The behaviour of current interest is the nuclear tunnelling between the rectangular configurations, this tunnelling results in a small correction where each of the known Raman peaks that have been previously classified under a rectangular symmetry divide into pairs. A previous study by Čársky et al. [109] used a three-dimensional Taylor expansion on a potential calculated under the generalized valence bond method, to approximate the wavefunction and to calculate the energy separation of these pairs. Unfortunately the energy separation that they predicted was not experimentally observed when cyclobutadiene was bound in a solid matrix, possibly due to environmental breaking of the square symmetry [89, 111].

As the calculation of the Raman spectrum and tunnelling rates are the same it is worth discussing the suitability of methods usually used to calculate vibrational spectra. The vibrational self-consistent field (VSCF) is commonly used in the literature [112, 113] to calculate anharmonic vibration states. This method is similar to the Hartree method for electron systems, as the wavefunction of the system is approximated as a single product [112, 113]. As a result the accuracy of the method is highly dependent on the basis set used, as it assumes that motions in each of the coordinates are separable. In this way correlation between nuclear motions can only be included through basis set functions. Due to this effective assumption about the separability (or near separability) of the basis, this method is unsuitable for application to cyclobutadiene, in which the tunnelling rate is calculated as a very small energy difference between two similar eigenstates. As a result a calculation of this value under VSCF would be especially sensitive to the choice of basis set, making it unsuitable. In the wider literature this shortcoming of VSCF has prompted the

development of more general methods that calculate more complete wavefunctions, so are necessarily more computationally expensive. In keeping with the nomenclature of electronic structure methods, these are called vibrational coupled-cluster, vibrational Møller-Plesset, and vibrational configuration interaction calculations[114, 115, 113]. Due to the sensitivity of the tunnelling of cyclobutadiene I will use the vibrational configuration interaction method, as it is the most general and accurate.

In this chapter I propose a general method for calculating the energy eigenstates and wavefunctions of nuclei bound in molecules based on an effective potential energy surface determined by the electrons and Coulombic forces. I use this to calculate the Raman spectrum and molecular wavefunctions using the symmetry-conserving motions permitted under the rectangular symmetry. I am able to determine how the nuclear motions for different Raman resonance states affect the rate of tunnelling. I show how the calculation and interpretation of the wavefunction reveals the sensitivity of the system to environmental effects, and how the inclusion of hydrogenic motion affects the carbon motion and the strength of the tunnelling interaction.

In cyclobutadiene I find the tunnelling mediates the interaction between the wavefunction at different structural conformations. As this tunnelling leads to diverse behaviour among the Raman active energy levels in the system, it is not possible to explain the properties of each of the excited states in a single way. Therefore even in cyclobutadiene since the two rectangular conformations at the potential minima are symmetry equivalent, one might intuit that the combined behaviour of the system is no more complex than a system that involved only one rectangular conformation, this is not the case. This constitutes evidence therefore that the inclusion of different isomeric structures in a quantum mechanical leads to more complexity, so that one ought to expect historical emergence to be present at some level of chemical complexity.

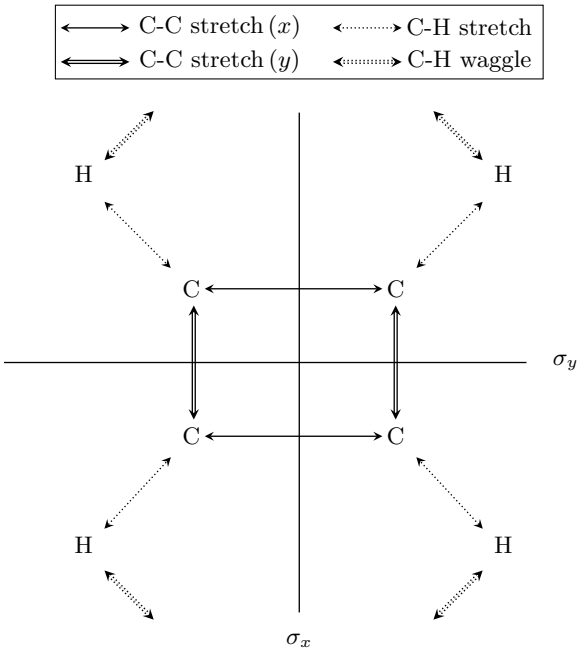

Figure 3.2: The (rectangular) a_g motions permitted in cyclobutadiene: C-C and C-H bond stretches, and the C-H bond waggle. The σ_x, σ_y reflection symmetries are also shown.

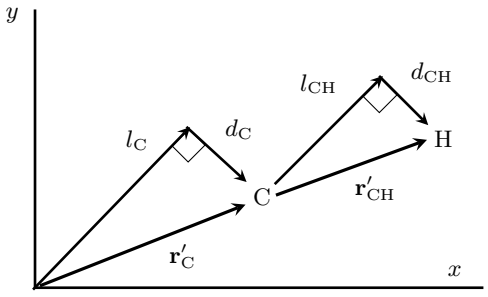

Figure 3.3: The calculation basis $\mathbf{r}'_{\mathrm{CH}} = (d_{\mathrm{CH}}, l_{\mathrm{CH}})$, $\mathbf{r}'_{\mathrm{C}} = (d_{\mathrm{C}}, l_{\mathrm{C}})$ used here, shown on a single quadrant of the molecule. This new coordinate set is related to the absolute positions by $\mathbf{r}'_{\mathrm{CH}} = \mathbf{r}_{\mathrm{H}} - \mathbf{r}_{\mathrm{C}}$, and $\mathbf{r}'_{\mathrm{C}} = \mathbf{r}_{\mathrm{C}}$.

3.2 Methods

Assuming adiabatic separation between the electrons and nuclei, I consider the four in-plane (rectangular, D_{2h}) a_g symmetry-preserving motions of the molecule, as shown in fig. 3.2. This assumes the effective potential, which is a function of the nuclear positions, can be expressed as a sum of potentials. Each of these potentials is related to a particular symmetry operator, and is a function of only those nuclear coordinates that break that particular symmetry operator [43, 44]. This effectively assumes that the motion in each of these symmetry directions is independent, permitting us to decouple the symmetry-breaking and symmetry-conserving motions. The Hamiltonian for this system is therefore

$$\mathcal{H} = \frac{\mathbf{p}_{\mathrm{C}}^{\dagger} \cdot \mathbf{p}_{\mathrm{C}}}{2m_{\mathrm{C}}} + \frac{\mathbf{p}_{\mathrm{H}}^{\dagger} \cdot \mathbf{p}_{\mathrm{H}}}{2m_{\mathrm{H}}} + V_{\mathrm{eff}}(\mathbf{r}_{\mathrm{H}}, \mathbf{r}_{\mathrm{C}}), \tag{3.2.1}$$

where $\mathbf{r}_{\mathrm{C}}$ and $\mathbf{r}_{\mathrm{H}}$ are the displacements of the carbon and hydrogen atoms from the centre of mass, m_{C} and m_{H} are the effective masses of the carbon and hydrogen that are determined by the concerted motion of the nuclei, and both being four times the value of the natural masses of the nuclei. Here V_{eff} is the effective potential determined by the adiabatically separated electrons, and the nuclear momenta operators defined in the usual way [104] with the canonical commutation relations $[\mathbf{p}_{\mathrm{H}} \cdot \mathbf{e}_i, \mathbf{r}_{\mathrm{H}} \cdot \mathbf{e}_j] = -\mathrm{i}\hbar\delta_{ij}$, $[\mathbf{p}_{\mathrm{C}} \cdot \mathbf{e}_i, \mathbf{r}_{\mathrm{C}} \cdot \mathbf{e}_j] = -\mathrm{i}\hbar\delta_{ij}$, where $\mathbf{e}_0$ and $\mathbf{e}_1$ are a pair of two-dimensional perpendicular unit vectors. However calculation in this basis is inconvenient because there are large regions of $\mathbf{r}_{\mathrm{H}}$ which can be effectively ignored.

A choice of basis set in vibration wave function methods can determine both the accuracy and computational load of a calculation. A common basis set used is the normal mode basis set calculated under the harmonic approximation [112]. However cyclobutadiene is demonstrably very dissimilar from a harmonic system as there are two local potential energy minima, one for each conformation in fig. 3.1. For such a normal mode calculation there are two options. The first is to us the high symmetry point at the crest of the potential energy barrier as the origin in an

harmonic expansion. This method must necessarily require a large basis set, as there is almost no wavefunction density at the high symmetry point. Another possible normal mode set may be constructed using two complementary harmonic expansions, each centred on one of the potential minima. However this combined basis will not necessarily be orthogonal. Worse still the overlap will be in the important tunnelling region, so is similarly unsuitable for the purposes of cyclobutadiene.

While it is possible to construct some more complex hybrid basis set with harmonic and real-space components or based on VSCF calculations [115], for the ease of implementation I instead use a real-space grid for the basis set. To make the problem tractable this grid must accommodate the different masses of the hydrogen and carbon. I therefore choose a new set of coordinates for the calculation, shown in fig. 3.3. This coordinate transformation results in a transformed set of canonical momenta that are related by $\mathbf{p}_{\mathrm{C}} = \mathbf{p}'_{\mathrm{C}} - \mathbf{p}'_{\mathrm{CH}}$, and $\mathbf{p}_{\mathrm{H}} = \mathbf{p}'_{\mathrm{CH}}$. In these new coordinates the Hamiltonian is

$$\begin{aligned}\mathcal{H} =& \frac{\mathbf{p}'^{\dagger}_{\mathrm{C}} \cdot \mathbf{p}'_{\mathrm{C}}}{2m_{\mathrm{C}}} - \frac{\mathbf{p}'^{\dagger}_{\mathrm{C}} \cdot \mathbf{p}'_{\mathrm{CH}} + \mathbf{p}'^{\dagger}_{\mathrm{CH}} \cdot \mathbf{p}'_{\mathrm{C}}}{2m_{\mathrm{C}}} \\ &+ \frac{m_{\mathrm{C}} + m_{\mathrm{H}}}{m_{\mathrm{C}} m_{\mathrm{H}}} \mathbf{p}'^{\dagger}_{\mathrm{CH}} \cdot \mathbf{p}'_{\mathrm{CH}} + V_{\mathrm{eff}}.\end{aligned} \tag{3.2.2}$$

This basis choice reflects the structure of the molecule, which is determined by V_{eff}. The potential is four dimensional, however because of the structure one is in practice able to subdivide the potential into three terms that reflect the potential energy of the C-C ring or the C-H bond, and the cross terms between them. I use

$$V_{\mathrm{eff}} = V_1(\mathbf{r}'_{\mathrm{C}}) + V_2(\mathbf{r}'_{\mathrm{CH}}) + V_3(\mathbf{r}'_{\mathrm{C}}, \mathbf{r}'_{\mathrm{CH}}), \tag{3.2.3}$$

$$V_1(\mathbf{r}'_{\mathrm{C}}) = V_{\mathrm{eff}}(\mathbf{r}'_{\mathrm{C}}, \mathbf{R}_{\mathrm{CH}}), \tag{3.2.4}$$

$$V_2(\mathbf{r}'_{\mathrm{CH}}) = V_{\mathrm{eff}}(\mathbf{R}_{\mathrm{C}}, \mathbf{r}'_{\mathrm{CH}}), \tag{3.2.5}$$

where the coordinates $\mathbf{R}_{\mathrm{CH}}$ and $\mathbf{R}_{\mathrm{C}}$ are the chosen such that $V_{\mathrm{eff}}(\mathbf{R}_{\mathrm{C}}, \mathbf{R}_{\mathrm{CH}})$ is the global minimum of the potential. The potential $V_3(\mathbf{r}'_{\mathrm{C}}, \mathbf{r}'_{\mathrm{CH}})$ is the four-dimensional correction term that accounts for the coupled nature of the bonding. If one has chosen the basis well then $V_3(\mathbf{r}'_{\mathrm{C}}, \mathbf{r}'_{\mathrm{CH}})$ is small everywhere, and one can qualitatively

characterise the molecule as a simple combination of C-C and C-H bond motions, in a form analogous to the harmonic approximation [43, 44].

The choice of this basis also enables us to impose appropriate boundary conditions on the system. A pair of potential cutoffs $V_1^{\max}$, $V_{2,3}^{\max}$ were chosen, so that in the calculation only regions where $V_1(\mathbf{r}'_{\mathrm{C}}) < V_1^{\max}$ and $V_2(\mathbf{r}'_{\mathrm{CH}}) + V_3(\mathbf{r}'_{\mathrm{C}}, \mathbf{r}'_{\mathrm{CH}}) < V_{2,3}^{\max}$ are included. A potential cut-off is appropriate as regions outside the boundary have too high a potential energy, so have a negligible amplitude contribution to the wavefunction and energy. I make two different choices of potential cutoff since the carbon and hydrogen nuclei have very different masses and different amounts of potential energy.

The potential $V_{\mathrm{eff}}(\mathbf{r}_{\mathrm{C}}, \mathbf{r}_{\mathrm{CH}})$ was calculated with density functional theory (DFT). This was performed using the plane-wave code CASTEP [87]. As plane-wave code relies on a periodic basis set, the size of the unit cell and the cutoff energy of the plane waves was converged, to where the error in the barrier height energy was less than 0.9 meV. The exchange correlation correction was calculated using the LDA [116].

3.2.1 Eigenvalue Computation

To compute the eigenvalues, a Cartesian basis set was first chosen. From this basis set an $n \times n$ matrix Hamiltonian was constructed, where n is the number of elements in the basis set. In order to compute the eigenvalues, the matrix was first tridiagonalised using the Householder algorithm [117], in which an orthogonal matrix is constructed that that transforms the principal matrix to tridiagonal form. With this tridiagonalised matrix, the differential quotient difference with shifts (dqds) algorithm was used to compute the eigenvalues [118], which is based on the general family of GR eigenvalue algorithms [119]. In this family algorithm the tridiagonal matrix T is factorised so that T = GR, where R is an upper right-hand bidiagonal matrix, and G is a matrix of specific properties, dependent on the exact algorithm

being used. A new tridiagonal matrix T′ is then constructed as T′ = RG, and this new matrix has the same eigenvalues as the original T, except that the off-diagonal elements are smaller. If this process is carried out a sufficient number of times, the off-diagonal elements become arbitrarily small, so that the diagonal elements can be made to be arbitrarily close to the eigenvalues.

The qd algorithm, the basis for the dqds algorithm, first constructs a complementary asymmetric matrix $\sim$ T = $D^{-1}TD$, where D is a diagonal matrix, such that the upper right-hand off diagonal is entirely composed of ones[117]. This matrix has by construction the same eigenvalues as T. This matrix is then decomposed into $\sim$ T = LR, where L is a lower left-hand bidiagonal matrix with ones on the diagonal, and R is an upper right-hand bidiagonal matrix, with ones on the off-diagonal. In the GR formalism these are then used to calculate the next tridiagonal in the iteration $\sim$ T′ = RL, but the qd algorithm does not calculate $\sim$ T′, and instead calculates L′ and R′, the decomposition of $\sim$ T′, directly from L and R. This algorithm has two benefits, first the simplicity of the LR decomposition lends itself to rapid computation, and second that it is more accurate as the L and R matrices are better stores of the eigenvalues than the tridiagonal matrices[118].

The difference between qds and qd algorithms is in the use of transformations of the form ρI, where ρ is a constant[117]. The qd algorithm is only guaranteed to be effective on matrices with positive eigenvalues, and so a shift can be introduced to change the eigenvalues to become positive. Further in the GR algorithm the lowest eigenvalues converge the most rapidly, and so it is useful to choose a shift such that the lowest eigenvalue is small and still positive. Once this eigenvalue is found to the desired accuracy it can be removed from the calculation via a rank-reduction of the matrix, and a new shift chosen for the new lowest eigenvalue. In this way the eigenvalues can all be computed to a high relative accuracy. Further development of the qds algorithm resulted in the dqds algorithm, which eliminates unneccessary subtractions, and improves the accuracy further [117].

The relatively robust representations (RRR) algorithm was used to compute the

eigenvectors of the tridiagonal using twisted factorisations. It is straightforward to construct a singular value decomposition of the tridiagonal matrix, however this is unreliable, as small numerical errors in the eigenvalue λ lead to large errors in the eigenvector. Twisted factorisations can be used in a more reliable method. A set of twisted factorisations are defined as $(\mathrm{T} - \lambda \mathrm{I}) = \mathrm{L}_k \mathrm{D}_k \mathrm{D}_k^{\mathrm{T}}$, where D_k is diagonal, and L_k is lower bidiagonal with unit diagonal until the $k-1$th column, and upper bidiagonal with unit diagonal after the kth column [120, 121]. The important values are the kth diagonal elements of D_k which I label γ_k, as an approximation for the eigenvectors $\mathbf{z}_k$can be calculated from $\mathrm{L}_k \mathbf{z}_k = \mathbf{e}_k \gamma_k$. Therefore if we choose a value r, such that $\gamma_r = \min|\gamma_k|$, we can compute an approximation for the eigenvector. This method has been shown to be effective provided that the eigenvectors are relatively well-separated, that is that γ_r is much closer to zero than any of the other γ_k, which is only possible when the eigenvalues are determined to a high relative accuracy.

The RRR algorithm separates eigenvalues into close groupings, and using the dqds algorithm ensures that the eigenvalues for each of these groupings are well determined relative to each other. The twisted factorisation procedure detailed above is then used to calculate the eigenvectors, which are then transformed back to the original basis using the transformation matrices determined in the tridiagonalisation [120, 121].

3.2.2 Convergences

DFT convergence DFT calculations here need only be converged with respect to the plane-wave energy cutoff and the free space between cyclobutadiene molecules. The convergence for these cutoffs was calculated using the fractional energy difference between the lowest energy molecular configuration and one other distorted one, using the method detailed in section 2.4. I take E' to the energy difference between the lowest energy and the distorted state. The results for this plane wave energy cutoff are shown in fig. 3.4. For the energy cutoff I took the value of 2000eV, which corresponds to an accuracy of one part in 50,000.

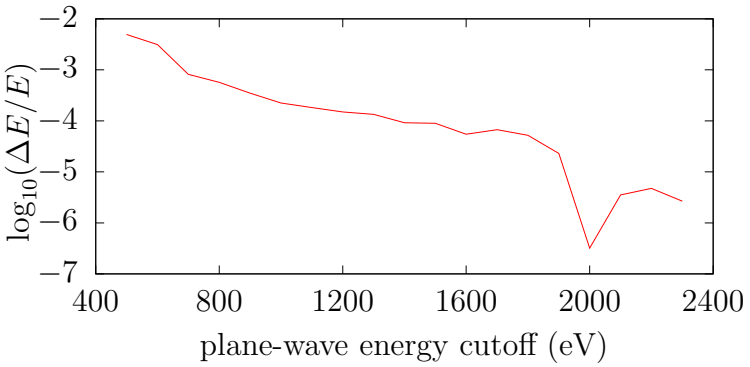

Figure 3.4: Convergence of the fractional energy difference between distorted molecular states as calculated using DFT, with respect to the size of the unit cell.

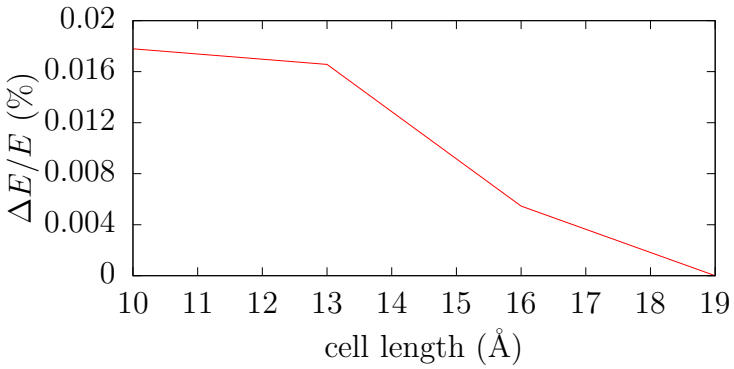

Figure 3.5: Convergence of the fractional energy difference between distorted molecular states as calculated using DFT, with respect to the energy cutoff of the plane waves, on a base 10 logarithmic scale.

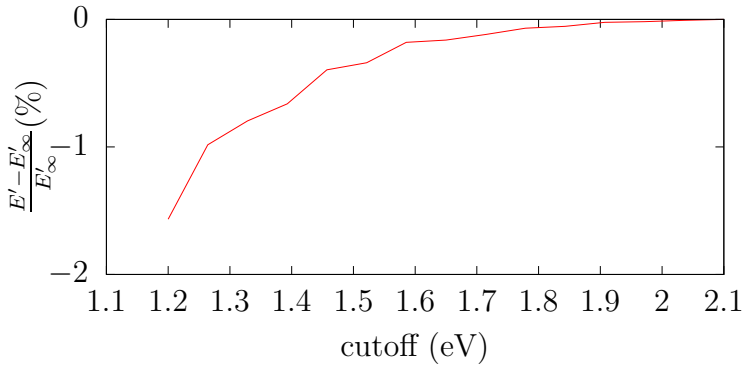

Figure 3.6: Convergence of the energy transition between the ground and first excited states of the $\mathbf{r}_{\mathrm{CH}}$ potential, with respect to the cutoff energy

For the free space between cyclobutadine molecules I use the same convergence method, where the length of the unit cell is the important parameter. The results for this convergence are shown in fig. 3.5. For the unit cell size I took the value of 15Å, which corresponds to an accuracy one part in 10,000.

Eigensolver convergence: C-H bond To perform the eigensolver calculations, I identify two calculation parameters that must be converged. First, the gridsize is the number of spatial divisions along each edge in the Cartesian mesh. Second is the cutoff energy, as points above a certain potential energy do not need to be considered. It is appropriate to choose cutoff energy for each of the potentials V_1 and V_2 as the expected value of the momentum for spatial variation in each of these potentials is different. I will again use the convergence method detailed in section 2.4, where I take E' to be the energy interval between different excited states, as a function of both the gridsizes and the two cutoff energies.

For the C-H stretch potential, the Cartesian mesh is rectangular and had an extent of 0.42 Å in the stretch direction, and 1.2Åin the waggle direction. $E(\infty)$ was estimated by $E'(43 \text{ points}, 2.0 \text{ eV})$. With respect to the cutoff energy, shown in fig. 3.6, the computational cost of increasing the cut-off energy is very small, and so for this case the error was overconverged and the value of the cutoff chosen to be 2eV, corresponding to an error of 0.01%. With respect to the number of point, shown in

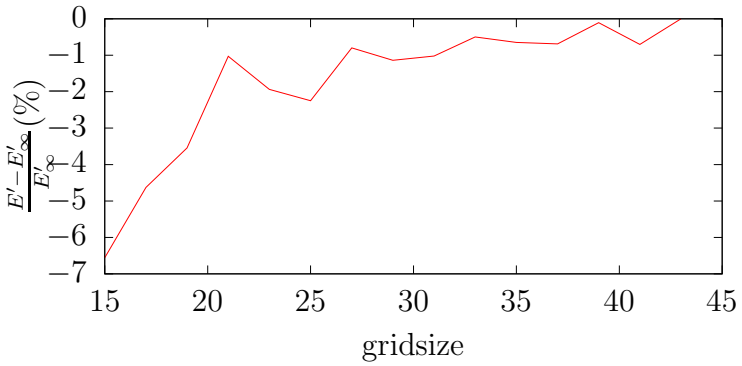

Figure 3.7: Convergence of the energy transition between the ground and first excited states of the $\mathbf{r}_{\mathrm{CH}}$ potential, with respect to the gridsize

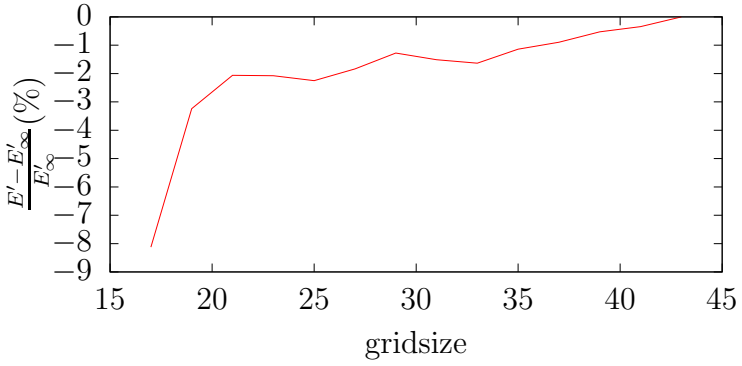

Figure 3.8: Convergence of the energy transition between the ground and fourth excited states of the $\mathbf{r}_{\mathrm{CH}}$ potential, with respect to the gridsize.

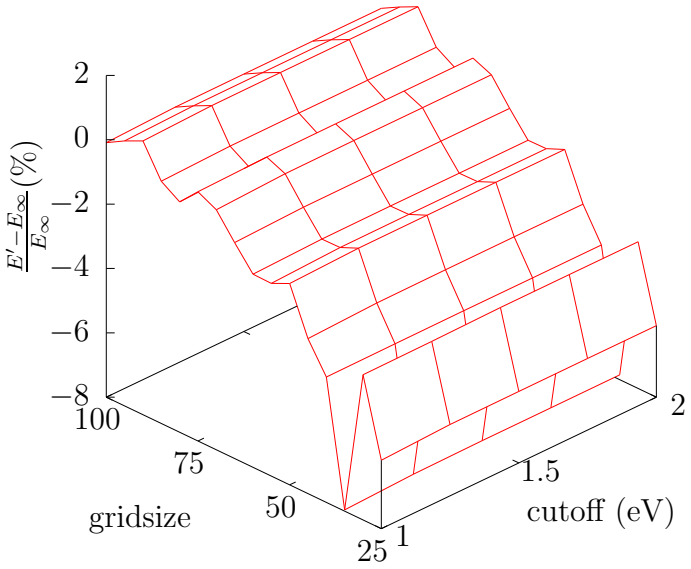

Figure 3.9: Convergence of the energy transition between the ground and second excited states of the $\mathbf{r}_C$ potential, with respect to the gridsize and cutoff energy.

figs. 3.7,3.8, the gridsize was chosen to be 21 corresponding to a convergence of one part in 30, this is therefore the limit of accuracy in this calculation.

Eigensolver convergence: ring In the eigensolver calculations for the ring potential, the Cartesian mesh is square and has an edge length of 1 Å, and $E(\infty)$ was estimated by $E'(60 \text{ points}, 2.0 \text{ eV})$. Result of the convergence between the ground and second excited states are shown in fig 3.9. It was found that a choice of a gridsize of 39 and a cutoff of 1.13 corresponded to a convergence to one part in 30. This is shown in fig. 3.9.

For the carbon ring the tunnelling rates are of interest, and their convergence must be determined as well. The convergence of the TSE of the $1A_g$ state is shown in fig. 3.10, and it shows that for my chosen values of gridsize and cutoff, it is converged to one part in 30. I will also compare the relative rates of tunnelling between different states. The convergence of the difference in tunnelling rates between the $1A_g$ and $2A_g$ excitations are shown in fig. 3.11, and it was found that these were converged to one part in 111 for the chosen gridsize and cutoff.

While the tunnelling rates of the excited states are sufficiently converged, the rapid

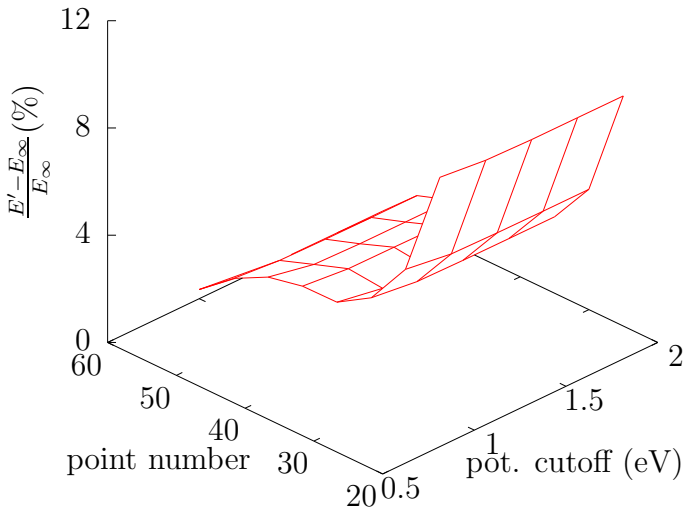

Figure 3.10: Convergence of the tunnelling seperation energy in the $1A_g$ state of the $\mathbf{r}_\mathrm{C}$ potential.

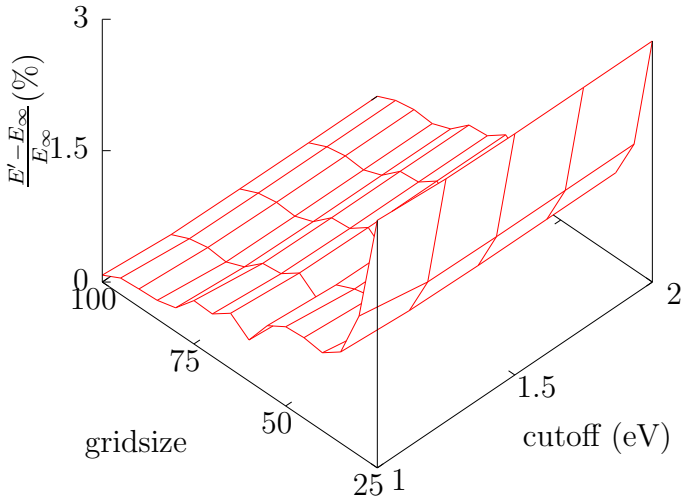

Figure 3.11: Convergence of the relative size of the $1A_g$ and $2A_g$ states' tunnelling rates in the $\mathbf{r}_\mathrm{C}$ potential.

variation of the wavefunction in the tunnelling region for the ground state wavefunction is less so. The same convergence calculations indicate that the ground state TSE is only converged to one part in four. However the TSE difference with respect to the $1A_g$ state is converged to one part in 40. Therefore I will restrict myself to a discussion of relative rather than absolute rates in tunnelling in the discussion of the ground state TSE. Combining the ring and C-H bond convergence parameters results in 38000 grid points in the calculation.

3.3 Results

DFT calculations found that when the potential is separated into V_1, V_2 and V_3 terms, the range of V_3 never exceeded 10 percent of the energetic variation from the global potential minimum, and there was no discernible change in the position of the minimum of $V_2(\mathbf{r}'_{\mathrm{CH}}) + V_3(\mathbf{r}'_{\mathrm{C}}, \mathbf{r}'_{\mathrm{CH}})$. This will permit us to qualitatively interpret the results as linearly linked C-H and C-C bond motions. I find the V_1 potential, for which a cross-section is shown in fig. 3.12, to be very similar to the standard 1-D double well system in which the first few energy levels are well localized. As their energy is less that the barrier height, their wavefunctions tunnel through the central barrier. The characteristic features of localized states in the double well, is that they are found in closely energetically spaced symmetric/antisymmetric pairs, and that the tunnelling rate across the barrier is proportional to this energy separation of the pairs. The more localized these states are, the smaller the energy separation between these pairs is, and correspondingly the smaller the rate of tunnelling. I performed computations on the two-dimensional potentials as well as the four-dimensional potential to compare how motion of the hydrogen nucleus affects the tunnelling of the carbon ring.

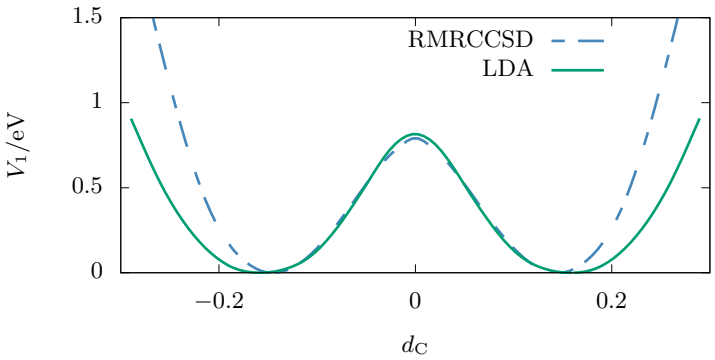

Figure 3.12: The potential ($\mathbf{r}'_C$), shown for a constant l_C chosen such that the potential energy at $\mathbf{r}'_C = (0, l_C$ is minimised. Potentials calculated using LDA here ($l_C = 2.02$), and reduced multireference coupled-cluster method with singles and doubles (RMRCCSD) calculations ($l_C = 2.07$) taken from reference [110], are compared.

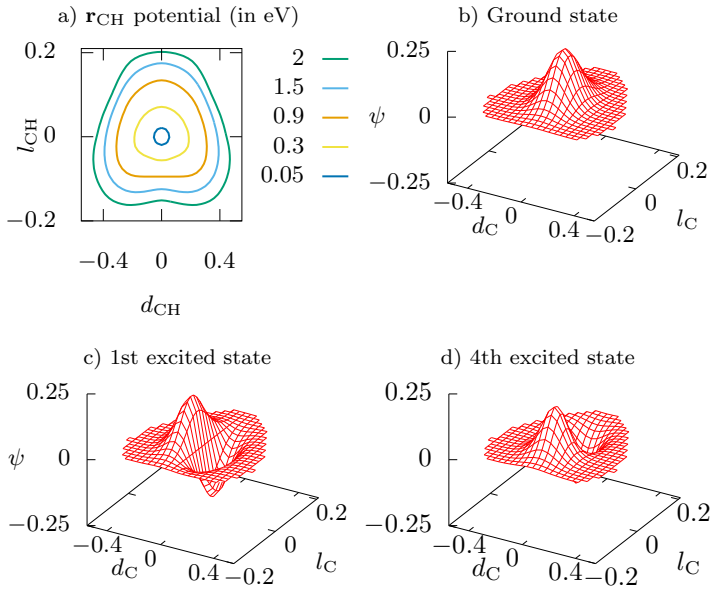

Figure 3.13: a) The governing potential $V_2(\mathbf{r}_{CH})$. b),c),d) Wavefunctions of the principal excited states with fixed $\mathbf{r}_C$ so that V_1 is at a minimum. ψ is the unitless finite (and real) wavefunction and defined so that the sum over the points (located at line intersections) $\sum \psi^2 = 1$.

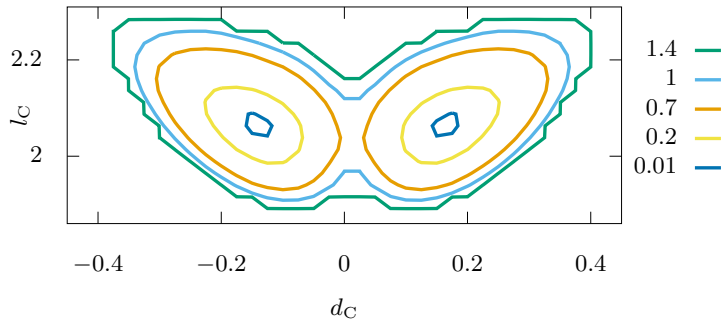

Figure 3.14: The governing potential $V_1(\mathbf{r}'_C)$, the energies of the potential are in eV. The jagged edge at 1.4 eV chosen as the boundary of DFT calculation, above the 1.13 eV cutoff.

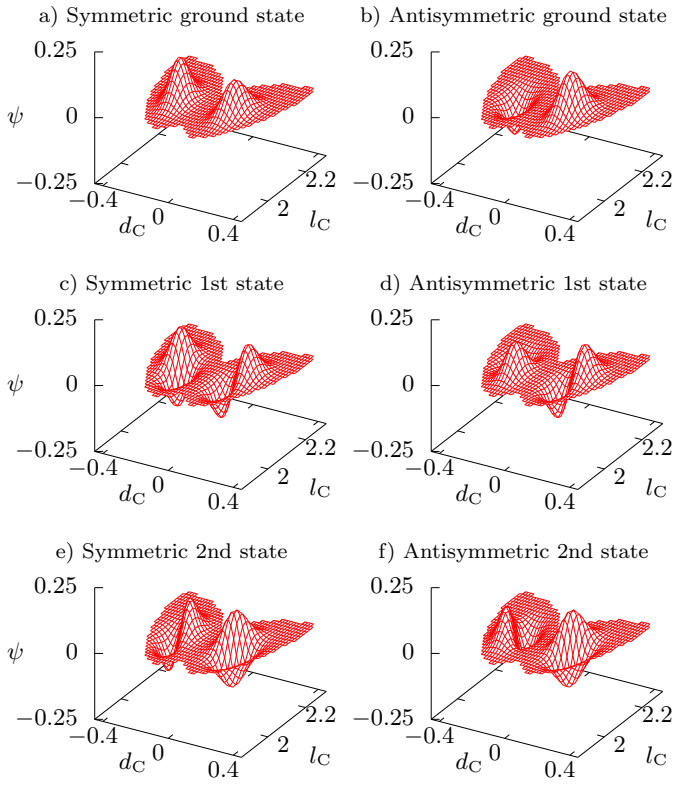

Figure 3.15: a)-f) Real wavefunctions of the finite 2-dimensional system with fixed $\mathbf{r}_{CH}$ so that $V_2 = 0.0$, with the first three (rectangular) states and their symmetric/antisymmetric pair. Values of ψ are normalized over the sum of their squares, all coordinates l_C, d_C are in Angstroms. a), b) correspond to the ground state under rectangular considerations, c),d) to the long-bond excitation, and e),f) to the short-bond excitation.

Ring Only

state	D_{2h}	energy (cm^{-1})	TSE (cm^{-1})
0 & 1	ground	0	0.0008
2 & 3	$1A_g$	1067	0.112
4 & 5	$2A_g$	1611	0.112

C-H only

state	D_{2h}	energy (cm^{-1})
0	0	0
1	$1A_g$	1248
2	$1A_g^2$	
3	$1A_g^3$	
4	$2A_g$	3139

Table 3.1: Energies of eigenstates calculated under ring-only and C-H only constraints. States are labelled by energy hierarchy and rectangular symmetry considerations (D_{2h}). For the ring-only case the energy separation between symmetric and antisymmetric states is also shown, labelled as Tun. Sep.

states	$D_{2h} label$	energy (cm^{-1})	TSE (cm^{-1})
0&1	ground	0	0.025
2&3*	$1A_g$	839	0.074
4&5*	$2A_g$	1005	0.046
6&7*	$3A_g$	1481	0.26
8&9	$1A_g^2$	1661	0.13
10&11	$1A_g \times 2A_{1g}$	1811	0.14
12&13	$2A_g^2$	1980	0.057
...			
...			
28&29*	$4A_g(+)$	3073	0.13

Table 3.2: Energies and the tunnelling separation energy between symmetric/antisymmetric pairs (TSE), of eigenstates ranked by energy and classified with D_{2h} symmetry considerations in the full 4-dimensional calculation. Principal excitations that I expect to dominate the Raman spectrum are marked with a star. A large number of states are not presented. Since they are not principal excitations they are unconverged. Due to this the state numbers of the final two excitations is likely incorrect.

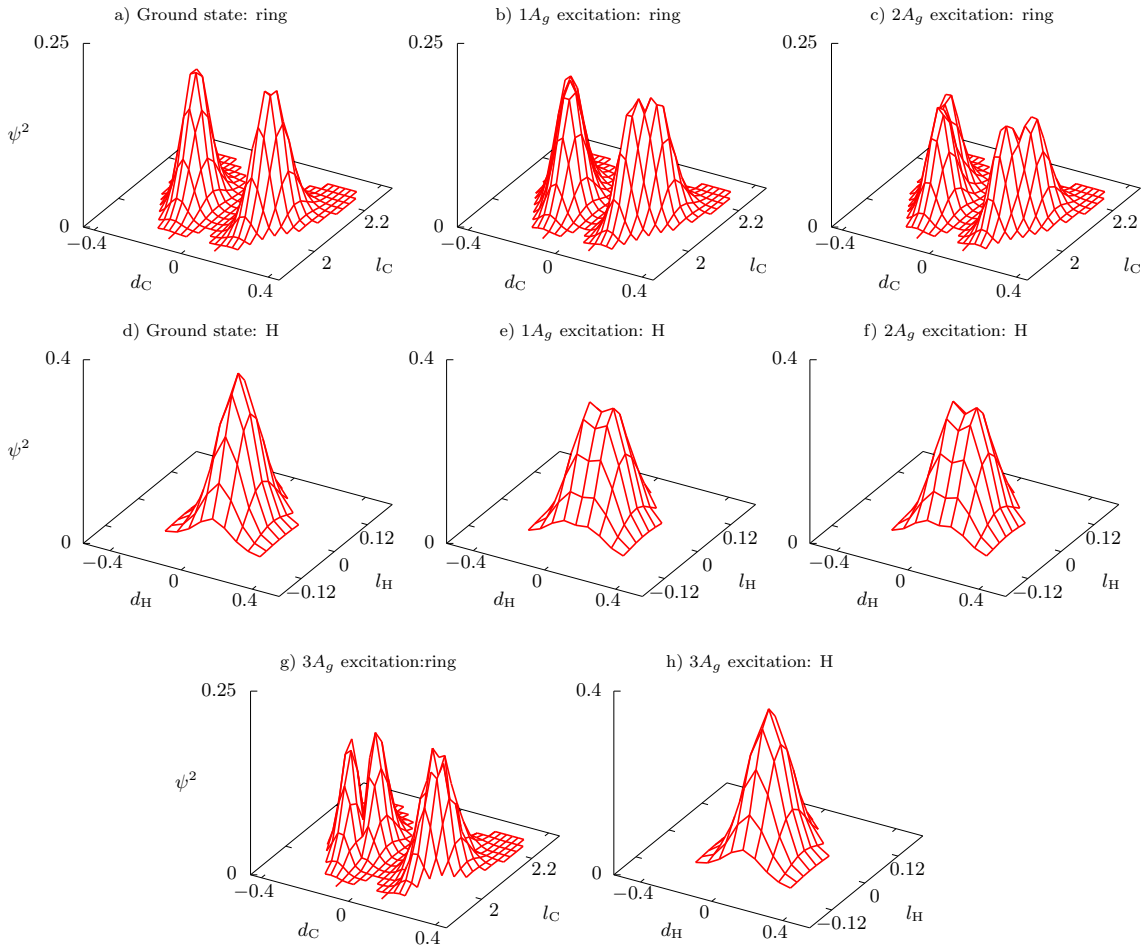

Figure 3.16: Pairwise average of the wavefunction densities of the first three principal rectangular excitations projected onto a)-c) the ring coordinates, d)-f) hydrogenic coordinates, and the fourth principal rectangular excitation projected onto g) ring coordinates, h) hydrogenic coordinates. Coordinate distances are in Å, and the densities normalized over the grid.

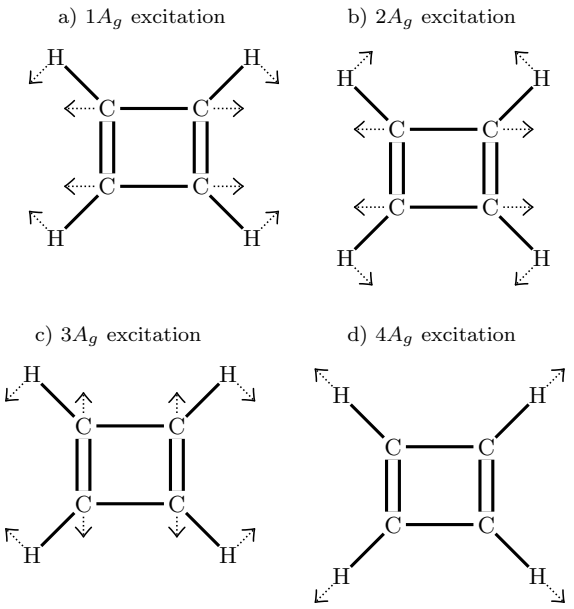

Figure 3.17: A_g excitations in cyclobutadiene

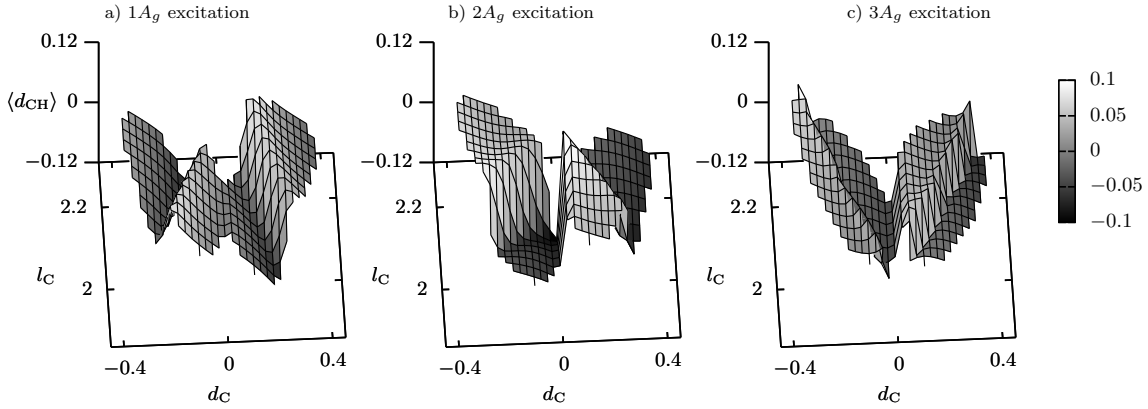

Figure 3.18: The expectation function $\langle d_{\mathrm{CH}}(\mathbf{r}_{\mathrm{C}}) \rangle$, which shows how the hydrogen and carbon motions are correlated. The values of all axes are in Angstroms.

3.3.1 Restricted 2D calculations

In order to understand how the multidimensional nature of the system affects the tunnelling rate, I performed calculations on two 2D subsystems in addition to the full 4D case. The 2D calculations were performed where either $V_2 + V_3 \equiv 0$ (called ring-only), or $V_1 + V_3 \equiv 0$ (called C-H-only). The results for the C-H-only calculation are straightforward as unlike V_1 there is only one potential well that is predominantly harmonic. The V_2 potential and wavefunctions are shown in fig. 3.13. There are two principal excitations, which I define as those states in which there is only one node in the wavefunction, as these correspond to the experimentally observable Raman excitations from the ground state. These states will dominate the spectrum since the wavelength of infrared radiation is much longer than the size of the molecule, so the gradient of a resonant electric field is roughly constant, and states with multiple wavefunction nodes will generate a smaller response. These principal excitations are fairly conventional with both the waggle mode where the wavefunction node is aligned along l_{CH} shown in fig. 3.13c), and the stretch mode in with the wavefunction mode aligned along d_{CH} shown in fig. 3.13b). The energies in table 3.1 show that the waggle mode has a lower energy than the stretch mode, due to the shape of the potential as the C-H bond is stiffer with respect to length changes than to lateral changes.

The V_1 potential used for the ring only calculation is shown in fig. 3.14. The shape of the potential is analogous to a two dimensional version of the double well potential as shown in the cross-section shown in fig. 3.12. Compared to the coupled-cluster calculations, the LDA potential used here has a similar barrier shape and height, but has wider wells [110]. Comparatively this will lead to a reduced localization of the wavefunction and weaker tunnelling than if a coupled-cluster potential was used. The contours around the two wells of the V_1 potential in fig. 3.14 resemble a pair of egg-shaped ovals, and the effects of the single and double electronic bonds are visible. The long direction of each oval is aligned with the single bond, and the

short width of the oval is aligned with the double bound. The wavefunctions for the lowest six energy states shown in fig. 3.15 are the principal excitation states. These need to be defined slightly differently to the C-H bond case since there are no calculations in which there is a single continuous wavefunction node, as it continues past the potential cutoff in the calculation. I define the principal excitation states here as the states in which there is only one wavefunction node in each potential well. Due to the anharmonicity of the potential the existence of multiple nodes does not suppress the Raman response. This is because in anharmonic systems under the perturbation of a linear spatial potential the ground state can transition to a multiple noded wavefunction, as the sum of the raising and lowering operators $\hat{a}^\dagger + \hat{a}$ is not proportional to the position operator $\hat{x}$. The wavefunctions show that the single and double bonds give rise to these principal excitations, with those corresponding to the length-excitation with the wavefunction node across the short axis of the oval fig. 3.15c),d), and those corresponding to the width excitation with the wavefunction node along the long axis fig. 3.15 e),f).

The six lowest-energy states are shown in Table 3.1. They are found in symmetric/antisymmetric pairs and are separated by a small energy which I call the tunnelling separation energy (labelled TSE). Within each pair the wavefunction density, the square of the wavefunction, is very similar and differs significantly only in the tunnelling region between the two wells. By contrast in this region the wavefunction phase either stays the same (symmetric states) or changes sign (antisymmetric states). In each pair the symmetric state is of lower energy than the antisymmetric state, in the low energy states that I calculated. By analogy to the double well, the differences in energy between each state in the pair gives the rate of tunnelling for those states. These energy differences, shown in table 3.1, determine the tunnelling rate. The greater the energy difference between the pair, the higher the tunnelling rate. This is because a localized state constructed from a superposition of the symmetric/antisymmetric states will oscillate between the wells at a frequency $f = \Delta E/\hbar$, which increases as energy separation ΔE. As expected the pair splitting

increases with respect to the total state energy, but this relationship is not linear; the length and width excitations both have around the same tunnelling separation energies despite having different total energies. This is because the motion and the momentum in the short-bond is more tangentially aligned to the barrier, and so the wavefunction does not penetrate so far through it.

To summarise, in the two-dimensional calculations one finds that in the C-H-only calculations the bond motion is very similar to the archetypal C-H bond, with a high energy stretch mode of energy around 3100 cm^{-1}, and a low energy waggle mode[44]. In the ring-only calculations one finds that the potential reflects the long and short bonds determined by the electrons, and these two bonds are responsible for the two different vibrational excitation energies. The system behaves similarly to a 1-D double well as states are found in symmetric/antisymmetric pairs, but the energy of a vibrational state is not enough to determine the tunnelling, as the distribution of the momentum is also important.

3.3.2 4D calculations

When one considers the hydrogenic and carbon-ring motions together, there are four principal excitations possible from D_{2h} symmetry considerations, and the ground state [122]. The most important effect of coupling the hydrogen and ring systems together is a mixing of the motions. As a result the hydrogen and carbon motions become correlated and illustrative sketches of these correlated motions are shown in fig. 3.17.

Of these the ring motions and the C-H waggle mix the most strongly, and form three different states. The C-H stretch motion only weakly couples with the ring motion, and as a result the energy is very similar to the C-H stretch calculated in the two-dimensional case. This can be seen from the projected densities, defined as $\rho_{\mathrm{CH}}(\mathbf{r}_{\mathrm{CH}}) = \sum_{\mathbf{r}_{\mathrm{C}}} \psi(\mathbf{r}_{\mathrm{C}}, \mathbf{r}_{\mathrm{CH}})^2$, and $\rho_{\mathrm{C}}(\mathbf{r}_{\mathrm{C}}) = \sum_{\mathbf{r}_{\mathrm{CH}}} \psi(\mathbf{r}_{\mathrm{C}}, \mathbf{r}_{\mathrm{CH}})^2$, shown in fig. 3.16; since the wavefunctions' nodes do not pass through the four-dimensional space

perpendicular to either the hydrogenic coordinates or the ring coordinates, there are no nodes where the density falls to zero in any of the density projections. Most importantly the density is still split into two regions on either side of the central barrier and this corresponds to a small energy separation between the symmetric and antisymmetric pair. This means that along with the correlations between hydrogenic and carbon-ring motion, the excited states are well localized into the rectangular states.

The first two excited states, $1A_g$ and $2A_g$ shown in figs. 3.16 b),e) and c),f), are the result of strong mixing between the C-H waggle and the long-bond excitation in the ring. Of these, the $1A_g$ excitation is broader and mixes more strongly. This can be observed since while in both excitations there is a saddle point between the two density maxima, which are present in both H and ring motion. In the $1A_g$ excitation the density at the saddle point is more similar to the density at the maxima than in the $2A_g$ excitation. This is likely because the carbon and hydrogen nuclear movements are mixed, and must share the limited energy available in the state. This means they are constrained to remain near the minima in the potential. The $3A_g$ excitation is mostly comprised of the short bond excitation in the ring, and is accompanied by a much smaller amount of hydrogen motion than for the other excitations, as the projected density for the hydrogen is very similar to that of the ground state.

However the projected densities do not provide important information on correlations of the nuclear motion in the excited states. While they show how much the hydrogenic and carbon motions have combined, they do not show how the motions are correlated. This information is required to match the states with schematic motions in fig. (3.17). It is given by the expectation function

$$\langle d_{\mathrm{CH}}(\mathbf{r}_{\mathrm{C}})\rangle = \frac{\sum_{\mathbf{r}_{\mathrm{CH}}} d_{\mathrm{CH}}\psi(\mathbf{r}_{\mathrm{CH}},\mathbf{r}_{\mathrm{C}})^2}{\sum_{\mathbf{r}_{\mathrm{CH}}} \psi(\mathbf{r}_{\mathrm{CH}},\mathbf{r}_{\mathrm{C}})^2}, \tag{3.3.1}$$

which calculates the expected position of the hydrogen for a choice of ring coordinates. This is shown in fig. (3.18). Using this one is able to obtain the correlated motions

of the atoms. In the $1A_g$ excitation, when the long bond is stretched, the hydrogen waggles in the same direction. The two are positively related, and so the hydrogen waggle and long-bond stretch are in phase. The $2A_g$ is the reverse situation, and so the motions are instead out of phase. In the $3A_g$ excitation, there is less movement overall in the C-H waggle, but the short-bond excitation and the waggle motion are also out of phase. In the $2A_g$ excitation there is a sharp change in the hydrogen displacement at $d_{\mathrm{C}} = 0$ accompanied by a sign change in $\langle d_{\mathrm{CH}} \rangle$, this is possible without the energetic penalty associated with a rapid change in the wavefunction because the wavefunction amplitude here is so low.

These calculations are able to calculate the energies and wavefunctions of nuclear energy states, which can be used to calculate all the properties of the excited states. However to perform this calculation effectively, and in order to interpret the results, the coordinate system used needed to reflect the structure of the potential energy surface. Since the potential energy surface is determined by the electrons one is able to use the bond lengths and angles (or the interatomic distances) as this basis. It is also important to restrict the space of the calculation, and this can be done by an appeal to the structure of the potential energy surface. It is important to ensure that the curvature of the wavefunctions, determined by the width of the well and the effective mass of the system in the chosen coordinates, is captured effectively. While this is done by choosing appropriate potential energy cutoffs and a choice of mesh grid spacing, the unequal curvature of the wavefunctions in figs. 3.18, 3.13, 3.15 suggests that improvements could be made which would further reduce the size and complexity of the computation.

In the ring-only vibrations (detailed in Table 3.1), the inclusion of the hydrogenic motion (detailed in Table 3.2) suppresses tunnelling motion in long-bond excitation states, but enhances it in the short-bond excitation states. This is in contrast to the two-dimensional results in which the tunnelling rate is equal for both single and double-bond stretches. There are two causes for difference in the tunnelling rate as more degrees of freedom are considered: in the $1A_g$ excitation the combination

of hydrogen motion with the long bond stretch lowers the energy of the vibration from 1067 cm^{-1} to 839 cm^{-1}. This lower energy results in a reduction of the nuclear momentum and the tunnelling energy difference from 0.112 cm^{-1} to 0.074 cm^{-1}. The second is caused by correlations between the carbon and hydrogen nuclei that suppress the tunnelling rate. For the $3A_g$ out-of-phase waggle state shown in fig. 3.18 b), as the ring conformation approaches $d_C = 0$, $\langle d_{CH} \rangle$ remains high, and at $d_C = 0$ there is a sharp change in $\langle d_{CH} \rangle$. This means that when the ring is in a conformation that is conducive to tunnelling, the hydrogen is out of place, and so the tunnelling rate is suppressed for this vibrational mode.

3.4 Symmetry and Raman excitations

Point group symmetries are used to classify and assign the eigenstates of nuclear motion [43, 44], however in cyclobutadiene the symmetry of the molecule is ambiguous. This is because there are two equivalent minima in the potential energy surface, at nuclear configurations that correspond to a D_{2h} symmetry, but tunnelling means that the eigenstates of the system are superpositions of these two configurations with a D_{4h} symmetry. Additionally the typical energies of the tunnelling separation are small enough that they may be distorted by an external perturbation, so I give an account for how this can occur as well.

In harmonic systems only excitations from the ground state to eigenstates with single nodes (principal transitions) are easily observable. Point group symmetries are useful for such systems as they allow us to predict the number of, and symmetry of, these principle transitions [122]. When one treats cyclobutadiene as a molecule with D_{2h} symmetry, this theory predicts that our calculations will accommodate four principle transitions of A_g symmetry. When one treats it with D_{4h} symmetry, it is predicted that there are two principle transitions with a A_{1g} symmetry and two with B_{2g} symmetry. This conflicts with our results, which show ten eigenstates arranged in pairs of similar energy, corresponding to up to nine principle transitions. The

discrepancy between these two models is due to the anharmonicity of the potential. While D_{4h} is a higher symmetry, the lowest energy nuclear configuration of D_{4h} symmetry is in fact a saddle point rather than a minimum so the requirement for this type of treatment, that the potential is harmonic, is not satisfied.

Since this anharmonicity is most significant in the V_2 potential, it is instructive to re-examine the 2-D wavefunctions of fig. 3.15. All of these states satisfy D_{4h} symmetry: symmetric states correspond to A_{1g} motions, and the antisymmetric states to B_{2g} motions. However most of the wavefunction is localised around the energetic minima located at configurations of D_{2h} symmetry, and around which the potential is almost harmonic. From the energies in table 3.1 the effective width of the potential barrier at the D_{4h} symmetry point is high enough that the tunnelling separation energies are much less than the energies of the lowest energy eigenstates. This means that for energetic purposes superpositions of configurations around the two minima in the potential are well separated and only interact weakly, and the coarse structure of the spectrum (in which the symmetric/antisymmetric pairs are treated as single eigenstates) can be readily interpreted using a D_{2h} symmetry approach, that relies on harmonicity [109, 110]. The overall D_{4h} symmetry is therefore only relevant for an experiment sensitive to the tunnelling separation energy, or for high-energy excitations that can tunnel through the barrier more easily. This is similar to the inversion doubling of spectral peaks, for example in ammonia [123, 124].

Anharmonicity and symmetry is of further relevance to calculations of cyclobutadiene. In particular I made the assumption that the different symmetry breaking and conserving motions could be decoupled. However recent calculations [125, 126] found metastable configurations of similar energy to the ground state, including a puckered configuration with an energy higher than the ground state by 302cm^{-1}, and a distorted planar ring configuration like that observed in the related tetrasilyl-substituted molecule with out-of-plane C-H bonds, that was higher in energy by 533cm^{-1}. While these metastable configurations are different enough from the D_{2h} and D_{4h} configurations that they are unlikely to contribute to tunnelling, they

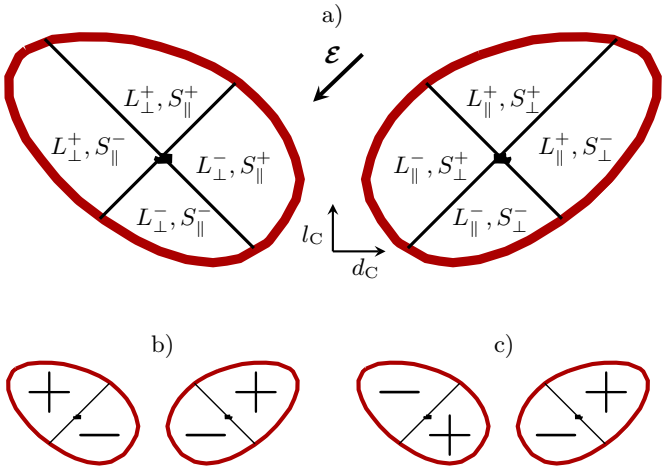

Figure 3.19: a) the eight regions $(L_l^{\pm}, S_s^{\pm})$, that can be used to determine Raman excitations to the principal excited states, and maps of the sign of the phase in b) the symmetric $1A_g$ excitation and c) the antisymmetric $1A_g$ excitation

show that the full potential energy surface of cyclobutadiene is complex and is not harmonic with respect to deviations that break the same symmetry. This suggests that motions which break different symmetries are not completely separable. Indeed other theoretical studies on cyclobutadiene that focus on more accurate calculations of the potential function, also separate the different symmetry motions and show only a partial improvement over the work performed here [101, 41, 110]. Therefore for more accurate calculations on cyclobutadiene, further study of these coupled motions may be necessary.

3.4.1 Raman excitations

Due to the tunnelling and the anharmonicity, it is not immediately clear what the realtive intensities of the infra-red transitions will be. As such I will examine how Raman scattering can be used to probe transitions between energy levels. Transitions between nuclear vibrational energy levels will correspond directly to Raman resonances [43, 44] due to the symmetry in cyclobutadiene. The amplitude of an optical-induced transition is dependent on a transition due to the polarizability

operator [127]

$$T_{a\to b} = \langle\psi_b|\hat{P}|\psi_a\rangle \tag{3.4.1}$$

where the transition is from nuclear vibration state a to state b, ψ_a is the wavefunction of state a, and the polarizability operator for the chosen field direction $\boldsymbol{\epsilon}$ is given by$\hat{P}_{\boldsymbol{\epsilon}} = \int \mathrm{d}\mathbf{x}_n \, |\mathbf{x}_n\rangle \, P(\mathbf{x}_n) \, \langle\mathbf{x}_n|$, where the sum is over the permitted nuclear configurations $\mathbf{x}_n$ and $P_{\boldsymbol{\epsilon}}(\mathbf{x}_n)$ is the polarizability of the electrons for the nuclear configuration $\mathbf{x}_n$. The polarizability operator is further defined as a projection of the polarizability tensor into the field direction $\boldsymbol{\epsilon}$.

The most straightforward application of this theory to simple hydrocarbons makes use of an approximation, that the polarizability tensor changes linearly with respect to changes in the molecular configuration [128, 129]. This means that in harmonic systems the transition amplitude is dependent only on the first derivatives of the polarizability tensor. Moreover, because of the linear response, the overall polarizability of the molecule can be expressed as a sum of polarizability contributions from each individual bond. Since the polarizability is already a second-order perturbative property, even for harmonic systems its derivative can in many cases not be approximated as constant. Due to this and the anharmonicity, this method therefore needs to be modified in cyclobutadiene to calculate the amplitudes of Raman scattering.

The polarisability matrix is given by $\frac{1}{2}\frac{\partial^2 E}{\partial\epsilon_\alpha \partial\epsilon_\beta}$, where ϵ_α is the electric field in direction α. As the polarizability is a ground state property of the electrons, it can be calculated in DFT. This can be performed using density functional perturbation theory. In a periodic implementation such as CASTEP, the contribution of an infinitesimal periodic electrostatic potential can be used to determine the response to a constant electric field[130]. In order to calculate the response of the electron density, while it is possible to use a numerical derivative, in practice it is much easier to construct a variational expression for the energetic perturbation, and then perform a variational search for the perturbation density. This variational search can be performed using the same methods as for the search for the ground state density.

In order to calculate the Raman response of cyclobutadiene, it is neccessary to calculate the polarizability response of all the different configuraitons of the molecule. After this it only remains to calculate the transition amplitues of equation 3.4.1 between the ground and excited states, using the wavefunctions presented in section 3.3.2. However as the DFT calculations were not converged with respect to the values of the polarisability tensor, I will instead use the experimental results to examine how the symmetry of this molcule affects the transitions.

I will compare the transitions from the ground state (state 0) to the two $1A_g$ states (states 2 and 3), to investigate the interaction of the Raman spectrum with the tunnelling. First I must set up the basis that I will study. Motivated by previous observations that most of the wavefunction is localised near the two minima with D_{2h} symmetry, I separate the configuration space into two, these are shown by the red ovals in fig. 3.19. It is necessary to use the wavefunctions of the excited vibrational states, and the only significant difference between these two wavefunctions is in their phase dependence on $\mathbf{r}_{\mathrm{C}}$. The phases for the excited states are shown for our two calculation regions in fig. 3.19 b) and c). For the electric field, I take its orientation to be along the direction of one of the C-C bonds, as this breaks the D_{4h} symmetry in a way that permits transitions from symmetric A_{1g} to antisymmetric B_{2g} states. Finally I need the polarizability responses of the bonds to this electric field. I label the responses for C-C bonds using $T_t^{\pm}$, where T has a value of either L for long bonds or S for short bonds, t describes the orientation of the electric field $\boldsymbol{\epsilon}$ to the the bond (either parallel or perpendicular), and $\pm$ describes the configuration of the bond which is either stretched $(+)$ or compressed $(-)$. With this labelling one can distinguish eight distinct sub-regions that contribute to the polarizability calculation, these are shown in fig. 3.19 a).

With this basis set one can calculate the transition amplitude in terms of these

sub-regions of the configuration space. If one defines the sub-region polarizability as

$$P(L_l^{\pm}, S_s^{\pm}) = \int_{(L_l^{\pm}, S_s^{\pm})} \mathrm{d}\mathbf{r}_{\mathrm{C}} \int \mathrm{d}\mathbf{r}_{\mathrm{CH}} \, \langle \psi_3 | \mathbf{r}_{\mathrm{C}}, \mathbf{r}_{\mathrm{CH}} \rangle \, \hat{P}(\mathbf{r}_{\mathrm{C}}, \mathbf{r}_{\mathrm{CH}}) \, \langle \mathbf{r}_{\mathrm{C}}, \mathbf{r}_{\mathrm{CH}} | \psi_0 \rangle \,, \tag{3.4.2}$$

where the integral in $\mathbf{r}_{\mathrm{C}}$ is over the limits of the sub region $(L_l^{\pm}, S_s^{\pm})$. One is then able to write the transition amplitude as a sum of the contributions of each sub-region

$$\begin{aligned} T_{0\to 3} \approx & \Big(P(L_{\parallel}^{+}, S_{\perp}^{-}) + P(L_{\parallel}^{+}, S_{\perp}^{+})\Big) \\ & - \Big(P(L_{\parallel}^{-}, S_{\perp}^{-}) + P(L_{\parallel}^{-}, S_{\perp}^{+})\Big) \\ & - \Big(P(L_{\perp}^{+}, S_{\parallel}^{-}) + P(L_{\perp}^{+}, S_{\parallel}^{+})\Big) \\ & + \Big(P(L_{\perp}^{-}, S_{\parallel}^{-}) + P(L_{\perp}^{-}, S_{\parallel}^{+})\Big) \,. \end{aligned} \tag{3.4.3}$$

This sum is approximate as I have not included the contribution from areas around the anharmonic central barrier where the wavefunction amplitude is very small. Previous work calculated $T_{0\to 3}$ to be approximately zero [89], but that $T_{0\to 2}$ was non-zero. From this one can infer that $P(L_l^{+}, S_s^{\pm}) - P(L_l^{-}, S_s^{\pm})$ is non-zero, as the $0 \to 2$ transition is non-zero, so for $T_{0\to 3}$ the contributions from each side of the barrier cancel out. Simply put, the derivative of the polarizability is symmetric with respect to a reflection about $d_{\mathrm{C}} = 0$. This is potentially unexpected, as it means that the polarizability response when the long bonds are aligned parallel to the electric field, is the same as when the short bonds are aligned parallel. What can be interpreted from this is that the long and short bonds are not separable because the polarizability must be dependent on the conformation of the whole ring. This puts cyclobutadiene in the same category as long alkene chains, in which the polarizability is dependent on the interactions between bonds, and cannot be isolated in individual bonds or sub-systems [131].

The energy differences between the symmetric and antisymmetric states are about 5 meV, and as a result I expect these properties of the system to be sensitive with respect to interactions with the surrounding environment. To analyse how thermal and symmetry-breaking external potentials have an effect on the system, I divide the

possible effects on the Raman spectrum of a symmetry-breaking external potential into three different classes when there is a i) negligible, ii) weak, or iii) large external potential, compared to the energy splitting caused by tunnelling.

When there is no external potential, there will be no localization into rectangular states. Optical excitations from symmetric to antisymmetric wavefunctions cannot be observed, and this means that the energy splitting caused by tunnelling is not observable. However if the temperature is high enough ($k_{\mathrm{B}}T \approx$ tunnelling separation energy), then there is a thermal occupation of the antisymmetric pair of the ground state, and the Raman permitted transitions between antisymmetric pairs will be observable as excitations from the antisymmetric state to higher energy antisymmetric states are possible.

When the external potential is slightly larger than the lowest symmetric/antisymmetric pair energy difference, only those lowest energy states will be localized into a specific rectangular state, as these have the lowest nuclear momentum and the weakest tunnelling, and a small energetic perturbation will localise them. To first order the wavefunctions of these low energy states will be approximately, in terms of the free-state wavefunctions $\psi_{\pm} = \psi_0 \pm \psi_1$. The higher energy states will retain most of their tunnelling characteristics. The ground state will completely lose its square symmetry. This localisation means that the transition amplitude $T_{0\to 3}$ changes, and instead is

$$\begin{aligned} T_{0\to 3} \approx & \sqrt{2}\left(P(L_{\parallel}^{+}, S_{\perp}^{-}) + P(L_{\parallel}^{+}, S_{\perp}^{+})\right) \\ & - \sqrt{2}\left(P(L_{\parallel}^{-}, S_{\perp}^{-}) + P(L_{\parallel}^{-}, S_{\perp}^{+})\right) \end{aligned} \tag{3.4.4}$$

and excitations to all the high energy states will be observable regardless of the temperature. This enhancement is reminiscent of catalysis, in which a metastable binding to another medium enables transitions to new states without the need for an increase in temperature.

When the external potential is larger than the highest symmetric/antisymmetric pair energy difference, all the energy states accessible from a ground-state transition

will be localized. There will be very little tunnelling across the barrier in any of the states. Due to the localization each state has a rectangular configuration and since all the states will be strongly localised, optical excitations between the two rectangular configurations will be strongly suppressed. Additionally at temperatures high enough to cause transitions between the two low energy rectangular states, tunnelling effects will not be found since tunnelling is suppressed for all states. Instead, depending on the exact form of the external potential, there may be vibrational differences between states in which either the long or short bonds are aligned parallel to the gradient of the potential.

3.5 Conclusion

Quantum mechanical tunnelling is important in many chemical reactions [132, 100] and structural phenomena. However while tunnelling in one dimension is easy to calculate, the extension to a multi-dimensional system like a coupled molecule represents a significant challenge [133]. A method of reducing this complexity is by choosing a suitable tunnelling pathway [132, 134]. In cyclobutadiene, as in ammonia [124], the tunnelling of particular states is sensitive to the distribution of momentum. The effect of this is that particular vibration states tunnel through the barrier along different paths, and so the calculation space must include these different tunnelling routes. The rates of tunnelling reactions that proceed via an adiabatic pathway are therefore dependent on eigenstates of the nuclear motion and their momentum distribution. I have shown that in some cases these can be understood as anharmonic extensions of the well understood harmonic resonance approximation, that is used to classify the resonances [43, 44]. This means that the nuclear motions under the well known harmonic approximation can be used to qualitatively understand the rates and pathways of tunnelling reactions, despite the multidimensional complexity of the problem.

Calculations performed here show that the square symmetry of cyclobutadiene is due

to quantum tunnelling, comprised of correlated nuclear motion through an energetic barrier. This tunnelling leads to a small correction in the energies of the vibrational frequencies of the molecule calculated under an assumed rectangular symmetry. Each energy level separates into a symmetric and an antisymmetric pair, and by analogy to the 1D double well potential, the size of the energy separation between these symmetric and antisymmetric pairs is related to the tunnelling rate across the barrier. From a comparison of the different vibrational states I find that the tunnelling rate across the barrier is sensitive to the distribution of momentum in the molecule, and the correlations between the motion of the nuclei. Our expectations about the motion of the molecule, for example tunnelling suppression in the out-of-phase waggle state, is able to give an accurate account for the strength of the tunnelling process. I also find that despite the overall square symmetry a combination of square and rectangular labels is most appropriate to classify the dominant system excitations and the Raman spectrum. This is because the square potential is so anharmonic that the usual assumption, that at the symmetry point there is an energetic minimum, fails. Instead the global energetic minima are at points that have rectangular symmetry.

The tunnelling effects are sensitive to an external potential, and a small external interaction can enable transitions to states that would otherwise be forbidden without a thermal excitation, while a large external interaction will again suppress that transition. This process is reminiscent of catalysis activation, and over-binding where a catalyst suppresses a reaction by trapping the reactants in a bound state. I have demonstrated that this method of calculating wavefunctions and energies can incorporate and enable the analysis of many complex quantum mechanical phenomena under a single approach. Perhaps more importantly, it can successfully inform our qualitative understanding and intuition about molecular motion as it generates quantitative results.

3.5.1 Conclusions about emergence

I have found that cyclobutadiene is not historically emergent in a meaningful sense. Instead it is a small, eight atom molecule with a restricted set of available states. While there are many excitations, there is no reason to suggest that beyond the point group symmetry of the molecule and the various symmetry breaking modes, each excitation has distinct properties which make it worthy of special study. No explanandum other than symmetry-breaking excitations is demanded of cyclobutadiene which would mean that each of these states would need to be considered separately. This means that there is no large multiplicity of different states required in any explanandum, so the molecule cannot be historically emergent.

However in this study of cyclobutadiene, it is the breaking of the symmetry that leads to an observation of a specific chemical structure as detailed in chapter 3.4.1. Although the properties of these structures can be cast in a combined form in a symmetric ground state, in order to realise the broken symmetries that are observed in a chemical molecules, the different symmetry-breaking operations that result in different molecular structures cannot be mutually reconciled into a single account. This means that the irreducible multiplicity of different chemical structures that is observed in chemistry must also be reflected in the properties of the underlying physics equations.

If, for an explanatory set-up, one chooses the explanandum "explain the functional properties of molecules", as there is a great multiplicity of molecular structures, each structure will have its own functional properties such that they must be considered separately. This means the explanatory set-up must be historically emergent. This will be the case regardless of whether or not the explanation is grounded in either a quantum mechanical or chemical description. The implications of this are that the different molecules must be studied independently. That is to say that all the diverse properties of chemical molecules cannot be predicted using a single generic method, as some imply [135, 8].

Chapter 4

Iron arsenide

4.1 Introduction

In condensed matter physics, it has been suggested that correlated electron phenomena may be emergent. This is usually done with respect to phenomena that is unexpected or novel with respect to usual electron behaviour. Examples include the fractional quantum hall effect (FQHE) [45] and the magnetic excitations Skyrmions [46]. These phenomena are usually emergent under conceptions like Batterman's, discussed in chapter 1.1.1, since when a material exhibits these phenomena the correlated electrons become qualitatively different to the properties of individual electrons. However the materials form these coherent states predictably[1], so it is not clear if historical emergence can add anything to discussions of correlated electron behaviour. In particular in an explanatory set-up relevant to these systems, the different states all share similar properties, and exhibit these properties in a predictable fashion.

In some incommensurate systems, for example GdSi [136], Ho[137], Cr[138], there are many different magnetic phases. As such examination of incommensurate materials may yield a system in which there are a large number of different magnetic structures, each with qualitatively distinct properties, that would be relevant to historical

[1]Predictable in the sense that an experiment can be reliably repeated.

emergence. Of especial interest would be a system in which there are a large number of different structures, in which the mechanism that drives and maintains each of the structures can only be explained by recourse to the magnetic structure itself. This is salient to historical emergence, because to explain the behaviour in such a system it would be necessary to treat each of the different states independently, rather than by reference to a single model about the collective behaviour.

In order to inform the relationship that correlated electronic and magnetic states have with historical emergence, I will study iron arsenide. Iron arsenide (FeAs) is related to the iron arsenide superconductors [139], in which the correlated electrons form a coherent superconducting state. Although it is not superconducting, FeAs has been found to have a noncollinear incommensurate spin spiral structure [140]. The periodicity of this structure is also known to change with temperature [47], so iron arsenide at least satisfies the requirement that in a historically emergent explanatory set-up there are a large number of different states. It has been suggested that the magnetic structure originates as a result of frustration between different magnetic configurations [48], and so it may be possible that the change in the magnetic periodicity originates from changes in interactions between these competing configurations.

4.1.1 Physical background

Iron arsenide is a material that displays an elliptic incommensurate helimagnetism that changes with temperature. It has been suggested that this is a result of competing low-energy magnetic states [48], and since the energetic contribution of the spin-orbit interaction in iron systems only around 1 meV in elemental iron [141], it is unlikely that the second-order Dzyaloshinskii-Moriya interaction drives the helimagnetism. Further this helimagnetic order breaks a number of crystal symmetries. These properties make it a reasonable candidate for emergent phenomena.

Additionally FeAs is currently of research interest in the physics research community,

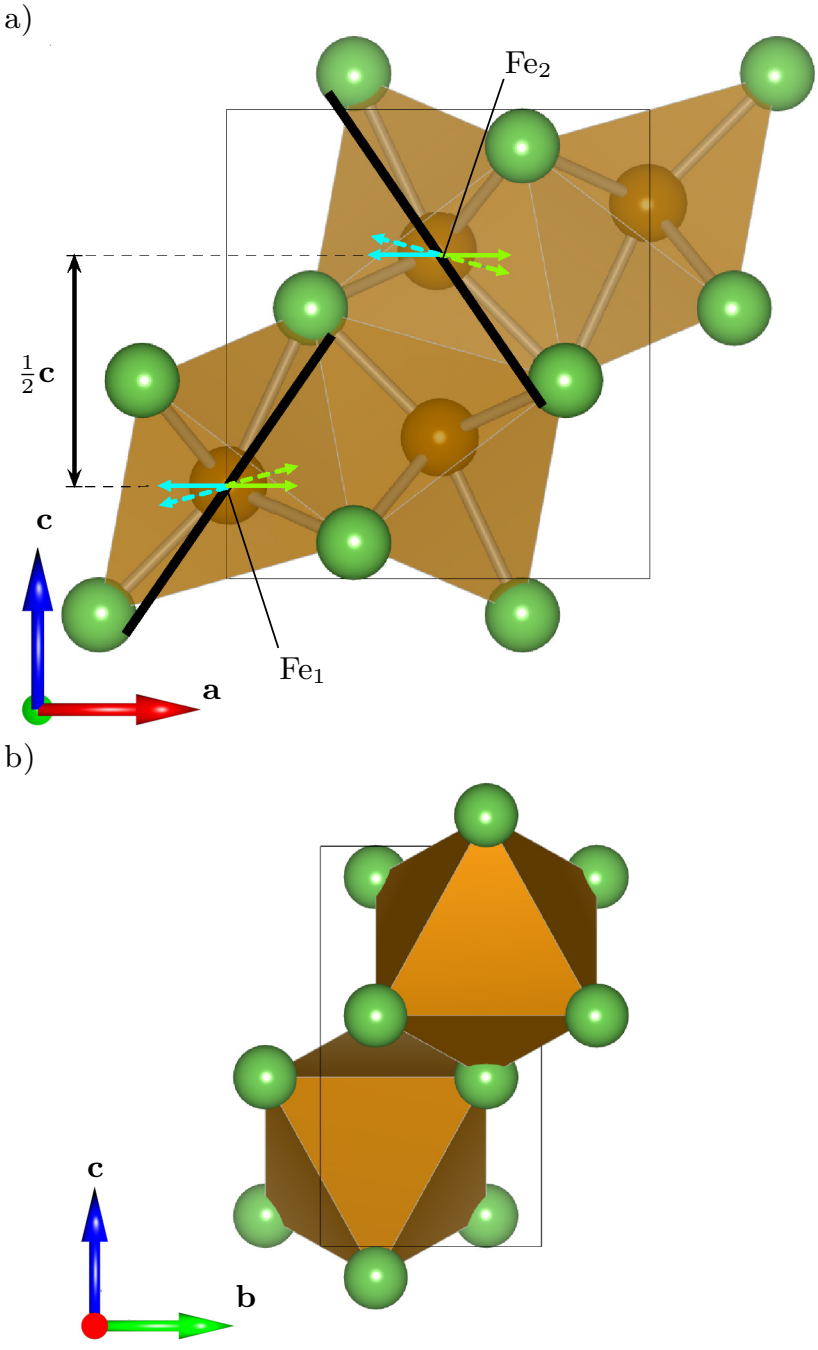

Figure 4.1: The structure of FeAs, showing the irregular face-sharing octahedra linked by arsenic atoms (green) with Fe atoms (brown) near their centers. Also shown in a) are a set of example axes along which the spin may preferentially align, confined in the a-c plane.

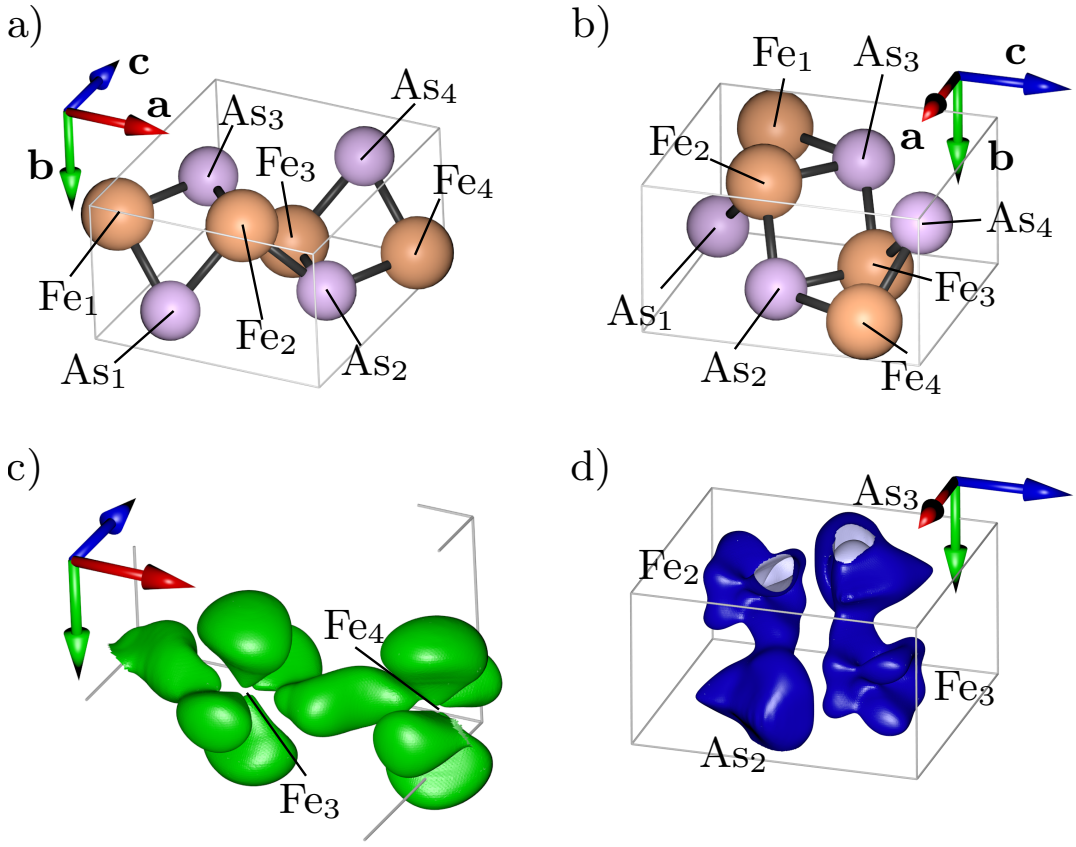

Figure 4.2: a), b) The crystal structure of FeAs shown from two different orientations, c), d) the differences in electron chage density between the zero-spin state, and the AFM1 state. c) shows selected regions around two Fe atoms where the electron density is lower in the AFM1 state, and d) where it is higher.

due to the similarity with the compounds of the iron pnictide superconductor family, in which the superconductivity is localized in planes of $FeAs_4$ tetrahedra [139]. However while FeAs shares the same Fe-Fe linkages, it crystallises in the B31 (MnP-type) structure (space group *Pnma*) [142] which is composed of $FeAs_6$ octahedra. These octahedra are face sharing along the *a*-axis and edge sharing along the *b*- and *c*-axes (fig. 4.1). The iron atoms sit at the *4c* Wyckoff site, giving rise to four positions in the unit cell: Fe1 at [140] (x, $\frac{1}{4}$, z), Fe2 at ($\bar{x}+\frac{1}{2}$, $\frac{3}{4}$,$z+\frac{1}{2}$), Fe3 at ($\bar{x}$, $\frac{3}{4}$, $\bar{z}$) and Fe4 at ($x+\frac{1}{2}$, $\frac{1}{4}$, $\bar{z}+\frac{1}{2}$), where $x = 0.004$ and $z = 0.199$ as shown in fig. 4.2.

Neutron powder diffraction measurements found a magnetic state that was best decribed by a nearly antiferromagnetic incommensurate magnetic order. The periodicity of the magnetic order can be described by a wavevector $q = [0, 0, 0.375]$ and an ordered magnetic moment of 0.5 μ_B. The onset temperature of the magnetic order is $T_N = 77\,K$, and as the material is cooled further below this temperature the size of wavevector changes, until it stabilizes at around 30 K [140].

Heat capacity measurements on FeAs [143] confirmed the value of T_N, and found that the transition is accompanied by only a small change in the Debye temperature from 351.3 K at 90 K to 350.2 K at 50 K. This behaviour contrasts with the incommensurate antiferromagnet chromium in which Fermi surface nesting accompanied by a lattice expansion drives the magnetic ordering [50, 144], and also by the very similar material CrAs in which the magnetic order is accompanied by a structural transition [145]. This implies that the nuclei are mostly unaffected by the transition to magnetic order, and that the order is driven primarily by purely electronic interactions.

With regard to the electronic properties, FeAs is best described as a correlated metal. This is borne out in DFT calculations show that the Fermi surface is strongly distorted by comparison to materials with nearly free electrons like sodium or copper. Experimental measurements on the transport properties of FeAs find that as the material is cooled through the magnetic transition, there is a derivative discontinutity in the resistivity. Upon further cooling, the resistivity displays neither a T^2 or

$T^2 e^{-\frac{\gamma}{T}}$ dependence typical of isotropic or anisotropic gapped magnon scattering in a Fermi liquid [146, 147], nor a T^5 Bloch-Gruneisen dependence typical of phonon scattering [148]. Instead my analysis of the results [149] in appendix A.2 indicates that it is matches closely to a T^n dependence beween 5K and 60K, where n =3.11 for resistivity in the **c** direction, and n = 3.66 for the **b** direction. This is a temperature dependence typical for a highly correlated metals, as it is caused by multiple bands of different masses with different interactions, which leads to a breakdown in assumptions about the interactions between excited electrons that underly the Fermi liquid model [148]. Further transport measurements on the Hall coefficient also indicate a complex Fermi surface, as the dominant carriers between 50 K and 150 K are hole-like, and outside of this range are electron-like. There is a derivative discontinuity of the Hall coefficient with respect to temperature at T_{N}, revealing that the transition to magnetic order involves a reconfiguration of the Fermi surface [149].

As concerns the magnetic properties, the axis-aligned magnetic susceptibilities $\chi_{\mathbf{a}}, \chi_{\mathbf{b}}, \chi_{\mathbf{c}}$ change as the material passes through T_{N}. At temperatures above 200 K, $\chi_{\mathbf{a}}$ and $\chi_{\mathbf{c}}$ are very similar, while $\chi_{\mathbf{b}}$ is lower [149]. These high-temperature susceptibilities can be explained if one assumes that the distorted $FeAs_6$ octahedra are the source of the spin-anisotropy. These octahedra shown in fig. 4.1, are angled at approximately 50^0 away from the **a** axis in the **a**-**c** plane. This angle means the octahedra are roughly equivalently aligned towards each of the **a** and **c** axes, which correlates with the rough equivalence of their magnetic susceptibilities. As the temperature is reduced below 200 K, the susceptibilities begin to fall, and $\chi_{\mathbf{a}}$ and $\chi_{\mathbf{c}}$ begin to diverge from each other. With the onset of magnetic order, there is a derivative discontinuity in $\chi_{\mathbf{a}}$ and $\chi_{\mathbf{b}}$, which is to be expected from a spin-spiral with moments localized in the **a**-**b** plane. For $\chi_{\mathbf{c}}$, there is no kink, but its second-order derivative abruptly changes sign, which indicates that the **c**-axis alignment of the moments interacts with the magnetic order [149].

In the magnetic susceptibility there is also evidence for interactions between magnetic

order and impurities or crystal defects. A study of single crystals with different structural disorder found that despite similar gross structure, the application of a magnetic field of 10 mT as the sample is cooled through T_N was able to significantly disrupt the formation of the magnetic ordered phase, but only in the structurally disordered sample [150]. In a single crystal with less disorder, they found only a small difference in the susceptibility measured between zero-field cooled and field cooled under the application of an external field of 100 mT, and this only below the 60 K, some 17 K below T_N. This behaviour was explored further in an earlier study [149] which found that under 300 mT of external field, the susceptibility behaviour matched that of the disordered crystal in which $\chi_{\mathbf{b}}$ drops below 25 K, by comparison to the zero-field cooled crystal in which the susceptibility increases until $\chi_{\mathbf{b}} \approx \chi_{\mathbf{a}}$. This behaviour indicates that the magnetic state continues to change and is not completely stabilized until at least 40 K, the temperature at which ZFC and FC measurements begin to diverge from each other. This behaviour may be due to the behaviour of the low-lying magnonic excitations, and their ability to form mesoscopic spin-structures under different environmental and crystalline perturbations similar to Bloch or Néel walls found in other materials.

More recent diffraction experiments by Frawley et al. used x-ray resonant electron scattering to probe the magnetic order [47]. Due to self-interaction between the excited electron and the hole in the nuclear core, this technique is unable to give energetic information, though it is sensitive to orbital and spin occupation near the Fermi surface for specific atoms [151, 152]. Excitations from the $2p \rightarrow 3d$ orbitals in iron at the Fermi surface provides a direct probe of the spins. They were able to identify new Bragg peaks which they attributed to be satellite peaks of the $[0, 0, 1]$ reflection caused by the magnetic order, $[0, 0, 1 \pm |q|]$. However $[0, 0, 1]$ reflections are symmetry-forbidden by the screw-symmetry along the **c**-axis, and this additional peak was not consistent with the helical or collinear spin structures proposed previously [140].

The relationship between the Fe nuclei and the spin structure is also of interest,

and a recent Mössbauer study by Blachowski et al. has found that upon transition to the magnetic ordered state, interactions between an iron nucleus and the rest of the crystal change [153]. They were able to fit experimental data by assuming that two distinct iron with differing environments exist in the unit cell. However since Mössbauer is purely a local probe, they were not able to identify the precise nature of this structural shift. They instead inferred that the Fe_1 and Fe_2 atoms were partially displaced in the reflection plane perpendicular to **b**, which like the proposed spiral ordering breaks the *Pnma* screw symmetry along **c**. A particular feature of Mössbauer is also its ability to probe the local magnetic environment, and they found a continuing change in the field anisotropy as the material is cooled past T_N to 40 K in agreement with the ongoing changes in the electronic and magnetic structure below the transition temperature discussed previously. The change in the nuclear interactions leads to an increase in the recoilless fraction in the Mössbauer results, which was attributed to an increased rigidity of the lattice on transition to the magnetically ordered state. In summary the Mössbauer studies suggest that the magnetic state is similar to chromium, in which the incommensurate magnetic order is accompanied by shifts in the positions of the nuclei, and their electron-mediated interaction with the crystal.

In iron arsenide the magnetic structure is not understood, as resonant x-ray results measures periodicities incompatible with previously proposed structures, and studies to date have not been able to point to a Fermi-surface instability [48] or a localized coupled-spin system [143] as the mechansim that drives the magnetic order. Here I propose a magnetic structure based on local environment and symmetry arguments, in which the magnetic moments canted out of the **a**-**b** plane. I justify how this correction arises in the material using arguments based on the projection of orbitals at the Fermi surface calculated under DFT, and probe the local Fe atom environment using spin-orbit coupling as a perturbation. Based on an analysis of the different spin configurations and their relative energies, I conclude that the magnetism in the system has its origin in a Stoner-type Fermi surface instability, which must be

significantly complicated by correlations in the material. With DFT I also examine the local Fe-potentials for different magnetic states, and these suggest that magnetic order in the system causes a distortion in the crystal lattice positions, similar to that occuring in chromium. I further discuss the implications of these findings and the experimental studies on the role of emergence in this incommensurate magnetic material.

Historical emergence These results of the physical investigation reveal that the different periodicities in the material are unlikely to require a historically emergent explanatory set-up. Instead if one constructs a free energy equation under Landau theory [154], the periodicity and canting of the magnetic moment are likely to be included in some form in the order parameter. This is possible because all of the different periodicities have qualitatively similar properties.

4.2 Methods

4.2.1 DFT parameters

Calculations were performed on the single unit cell of iron arsenide shown in fig. 4.1 a), b), where $a = 5.4560$ Å$, b = 3.3284$ Å$, c = 6.0310$ Å[140]. Collinear and zero-spin DFT calculations of FeAs were run with the CASTEP electronic structure code using the PBE exchange-correlation functional [155, 87], as LDA often has problems accounting for the d-orbitals in iron [156]. Energy differences between spin configurations were converged to 1 part in 10,000, and to generate the Fermi-surface a MP k-point grid of $23 \times 27 \times 19$ was used. To account for core state contributions on atoms an ultrasoft core-corrected iron pseudopotential with 8 valence electrons and an arsenic pseudopotential with 15 valence electrons were used. A non-magnetic configuration and a range of collinear ordered spin-structures were considered.

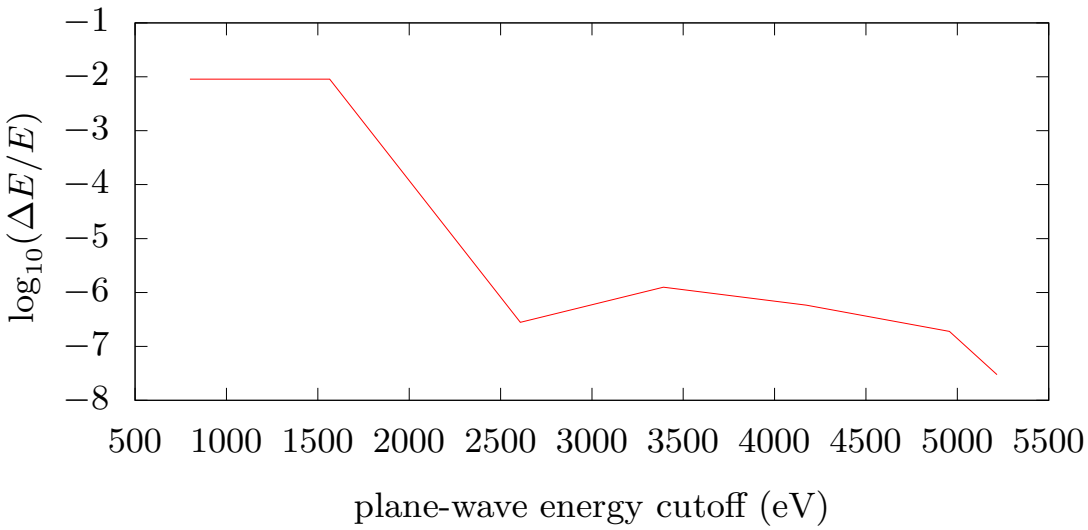

Figure 4.3: Convergence of energy differences between magnetic configurations, with respect to the energy cutoff of the plane waves.

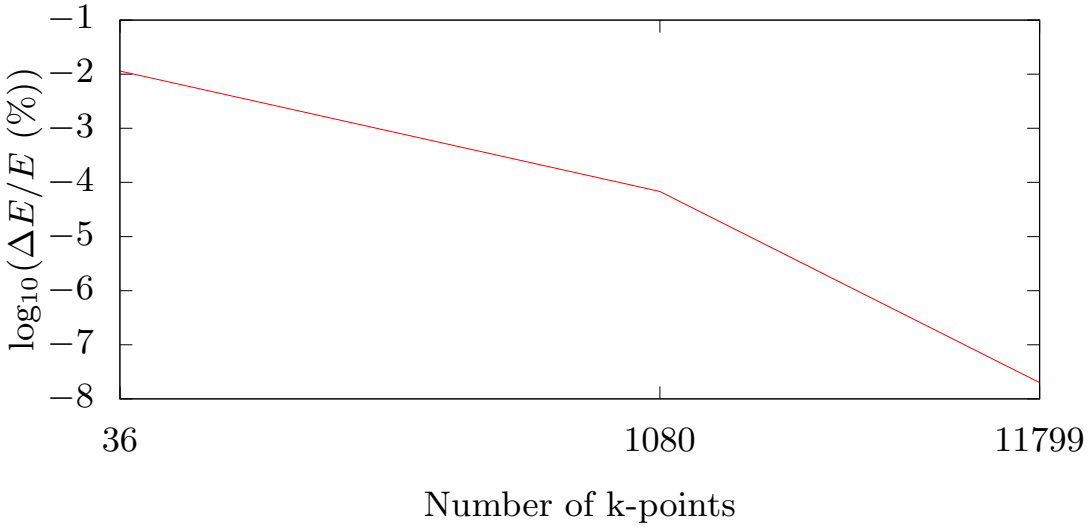

Figure 4.4: Convergence of energy differences between magnetic configurations, with respect to the total number of optimally spaced k-points in the MP grid.

Convergences As a periodic crystal FeAs calculations under plane-wave code need to be converged with respect to the cutoff energy of the plane-waves and the kpoint density. The values of these parameters that are required for our calculations are determined using my convergence function in chapter 2.4. The energy differences of interest are between magnetic states, so I use the energy difference between a calculation with no spins, and the lowest-energy collinear magnetic configuration as the energy parameter in the convergence function.

The convergence for the energy cutoff of the plane waves is shown in fig. 4.3, and I note two points of interest. A plane-wave cutoff value of 800 eV will be adequate for many systems with an accuracy of 1 part in 100, and a higher cutoff of 2000 eV will be used for fine-detail calculations as this gives accuracy to one part in 10,000, or as an absolute energy about 0.1 meV.

Convergence with respect to the number of kpoints is shown in fig. 4.4. Similar to the plane wave cutoff I note two points, 36 kpoints give a convergence of 1 part in 100, and 1080 to one part in 10,000.

4.2.2 Calculating spin-orbit perturbations

In order to see the effect of the spin orbit interaction or a similar perturbation on the ordered magnetic structure, I calculate the energetic perturbation of the spin-orbit interaction between the iron electron spins and the projected atomic orbitals. This is used to estimate the preferred direction of Fe spin alignment.

The perturbation to the ground state energy can be calculated using the minimization of the energy density functional given by

$$H = H_0[\rho] + \varepsilon H_{\text{spin-orbit}}[\rho], \tag{4.2.1}$$

where $H_0[\rho]$ is our unperturbed density functional for the energy and ρ is the electron density. In the Kohn-Sham representation one can use the usual electronic formulation for the spin-orbit interaction, including it as a correction term to the electrostatic

field around a given atom. The energetic perturbation on the Kohn-Sham orbitals to lowest order is given by

$$\begin{aligned} H_{\text{spin-orbit}}[\rho] &= \sum_{i,k} \langle \Psi_{i,k} | \hat{H}_{\text{LS}} | \Psi_{i,k} \rangle, \\ &= \sum_{k} \sum_{n=0}^{N_{\text{F}}} \sum_{n'>N_{\text{F},k}}^{\infty} \frac{\left| \langle \Psi_{n,k} | \hat{H}_{\text{LS}} | \Psi_{n',k} \rangle \right|^2}{E_{n'} - E_n} \end{aligned} \tag{4.2.2}$$

where the sum is over the Kohn-Sham orbitals $\Psi_{i,k}$ labelled by band i and kpoint k, n is the sum over occupied orbitals, with $N_{\text{F},k}$ the number of occupied orbitals at k . The first term in this equation is the paramagnetic response, and the second term is the diamagnetic response. The paramagnetic term will produce a change in the energy of the system by shifting the energy of the bands. This will lead to a change in the energy of the orbitals to first order, and can be positive or negative depending on the relationship between the spin orientation and the orbitals. By contrast the second diamagnetic term is always positive as it involves a second-order mixing of the higher-energy Kohn-Sham orbitals. For conductors the diamagnetic term is usually much smaller than the paramagnetic term as the presence of the Fermi surface additionally allows a reorganisation of the occupancies of the bands. As FeAs is a conductor, I will only consider the paramagnetic term here. The spin-orbit operator is

$$\hat{H}_{\text{LS}} = -\frac{\mu_{\text{B}}}{e\hbar c^2} \hat{\mathbf{s}} \cdot \hat{\mathbf{L}} \frac{\mathrm{d}\hat{V}}{\mathrm{d}r_{\text{atom}}} \frac{1}{\hat{r}_{\text{atom}} m}, \tag{4.2.3}$$

where $\hat{V}$ is the electrostatic potential around the atomic nucleus, $\hat{r}_{\text{atom}}$ is the distance to the centre of the atom, and m is the band mass of the Kohn-Sham orbitals.

In FeAs, the electrostatic potential around the iron atoms, for which an isosurface is shown in fig. 4.5, is almost completely spherical around the location of the iron atom. This is because the core orbitals that play the most important role in shielding the nuclear charge are not affected by the bonding. If one approximates the dependence of the potential around the iron atom to be entirely radial, this leads to the condition $\left[\hat{\mathbf{L}}, \frac{\mathrm{d}\hat{V}}{\mathrm{d}r_{\text{atom}}}\right] = 0$. When one only considers the Fe3d orbitals which are the dominant bands at the Fermi surface. These two constraints permit a significant simplification

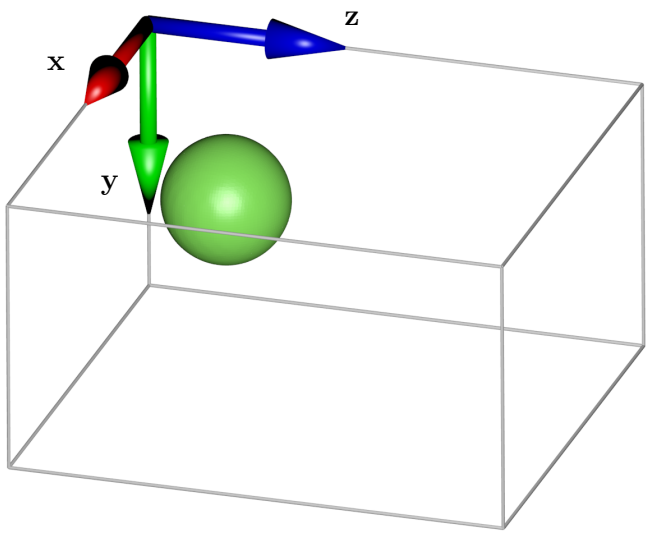

Figure 4.5: The isosurface of the electrostatic potential $V = 0$ in FeAs, around the Fe2 atom

of the calculation.

For zero-spin calculations where $\rho_\uparrow = \rho_\downarrow$, the energetic perturbation $H_{\text{spin-orbit}}[\rho]$, which I abbreviate to α, is second-order in the perturbation parameter [157, p.291] ε. This is because the energetic response of the spin up and spin down electrons must be equivalent, as in equation 4.2.2, $|\Psi_\uparrow\rangle = |\Psi_\downarrow\rangle$ and $\mathbf{s}_\uparrow = -\mathbf{s}_\downarrow$. One can calculate this effect using the diagram shown in fig. 4.6. Without loss of generality, one can label the band that increases in energy the spin-up band, and the one that decreases spin-down. Both bands shift by the same energy $\delta E_{\text{LS}} = \langle\Psi|\hat{L}_{z'}/m|\Psi\rangle$, where z' is the direction of the spin moment an atom and $L_{z'}$ is the component of angular momentum in this direction. These energetic shifts lead to a re-organisation of the band-occupation around the Fermi-surface (a transition from the red region to the blue in the diagram), and so for all kpoints at the Fermi surface, this change is given by

$$\alpha \propto -\varepsilon^2 \int \frac{|\langle\Psi|L_{z'}/m|\Psi\rangle|^2}{|\nabla U|} \mathrm{d}\Psi, \tag{4.2.4}$$

The integral is over all orbitals Ψ that lie on the Fermi surface, and is dependent on the gradient of the energy U of those orbitals $|\nabla U(\Psi)|$. One finds that the diamagnetic contribution of the orbitals is small compared to α and has therefore

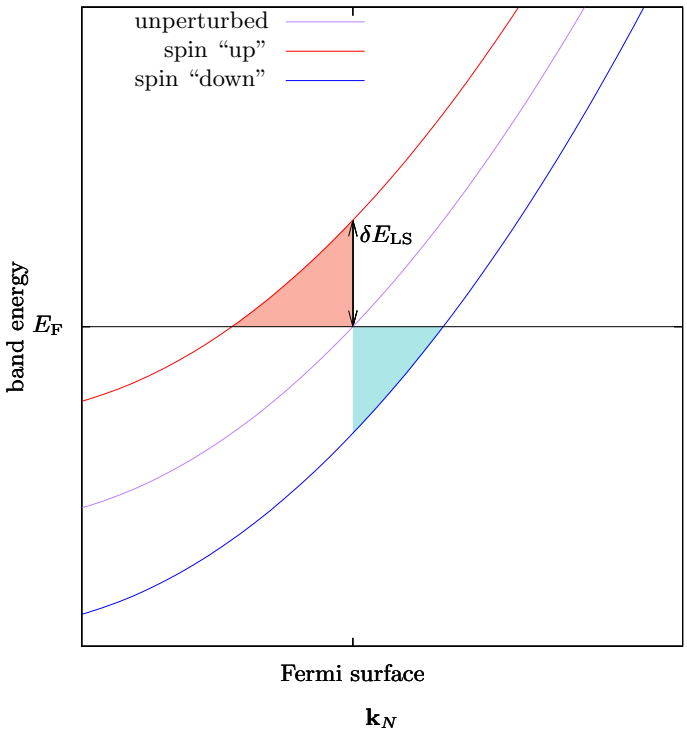

Figure 4.6: Diagram of the affect of a perturbation on the reorganisation of model quadratic bands around the Fermi Surface, in the direction normal to the Fermi surface $\mathbf{k}_{\mathrm{N}}$. The shaded area above the fermi surface is the energy saved by shifting the occupancy to the lower band, and the shaded area below is the energy gained by occupying the lower bands. The total energy change at a point on the Fermi surface is the difference betwen these two shaded areas.

been neglected. This perturbation will change the density to second order, and since according to Janak's theorem $\frac{\mathrm{d}E}{\mathrm{d}\rho} = 0$ [67], and so density changes will only have a third-order contribution to the energy. As such one is free to choose the value of z' and calculate a physically meaningful energetic perturbation for this chosen spin orientation, and create a full map of the energetic perturbation for different spin alignments. This allows us to assess the spin anisotropy of a specific atom, providing there is no band crossing at the Fermi surface.

The principal parts of a plane-wave pseudopotential calculation are the projections of the Kohn-Sham orbitals onto the atomic basis set. The atomic orbital projections do not necessarily obey crystal symmetries. To generate the full set of projections the relevant local symmetry operators are calculated from the Wigner-d matrices [158] and, if required, the application of a reflection. From this complete orbital projection, projection amplitudes for points at the Fermi surface are calculated using a B-spline interpolation [159]. The points are chosen using an algorithm detailed in appendix A.1 .This projection of the Fermi surface is then used as the basis for the energetic perturbation computation.

The final result is calculated by applying Eq. 4.2.4 to each Fermi surface point, and $\mathbf{L}_{z'}$ is calculated using a Mulliken orbital projection [160], and the use of Wigner-d matrices to include a rotation from the z-direction to z' [158]. This is performed successively for each value of z' to generate a full map (in energy) of the perturbation, which is chosen to be a polar map with regular intervals in both θ and ϕ coordinates. I take the unperturbed state (corresponding to $H_0[\rho]$) to be the zero spin configuration.

Computational implementation I use here the area as a proxy for all the surface properties. The convergence for this is shown in figure 4.7. Due to the nature of the grid chosen, it converges slowly for the surfaces with the most curvature. The graph shows that these areas are converged to one part in 30. Fortunately, due to the shape of the Fermi surface, it was not necessary to introduce additional functions to deal with singularities, such as if $|\nabla U| \to 0$ or $m \to 0$ in equation 4.2.4.

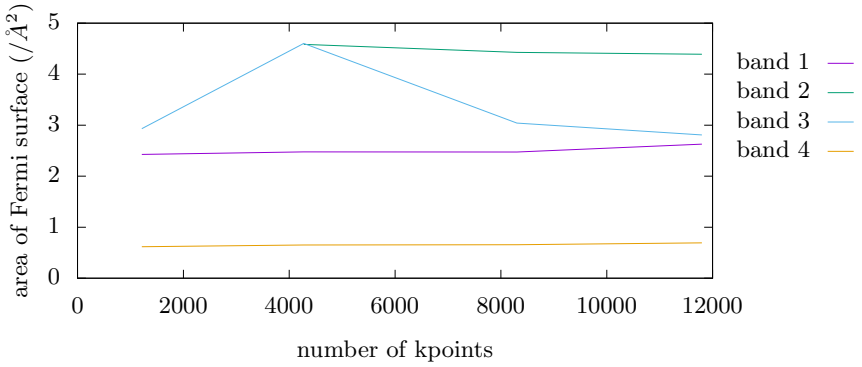

Figure 4.7: Convergence of the area using the method detailed in appendix A.1

4.3 Study and results

4.3.1 Structure of the magnetic order

To provide an explanation for the magnetic structure, I examined the local environment of the iron atoms as it is their magnetic moments that are used to experimentally determine the structure. The new structure must be a correction to the previously proposed spiral structure, since this matches with all the other observations. The new peaks of interest, that must be accommodated are the satellite peaks around $[0, 0, 1]$ reflection, that is forbidden due to the two-fold screw symmetry along the **c** axis. This screw symmetry relates Fe_1 to Fe_2, so the magnetic moment must interact differently with the local environment on each atom to generate the satellite peaks. To provide the argument I refer to fig. 4.1, in which I examine the interaction of constant spin moment pointing in the **a** direction with a proposed easy axis aligned with the arsenic octahedra (the black lines in the diagram). The spin moment will be canted towards the easy axis. It can be seen that the local iron environment provided by the distorted arsenic octahedra will interact with the spin moment differently in each case. The presence of a reflection in the **a**-**c** plane means that an easy-axis must be restricted to that plane, and the spiral symmetry means the Fe_1 and Fe_2 axes will be related by rotation around **c**. As the Fe_1 and Fe_2 easy axes point in different directions, the spins will be canted into different directions on each atom. This would break the screw symmetry in the magnetic structure, and permit

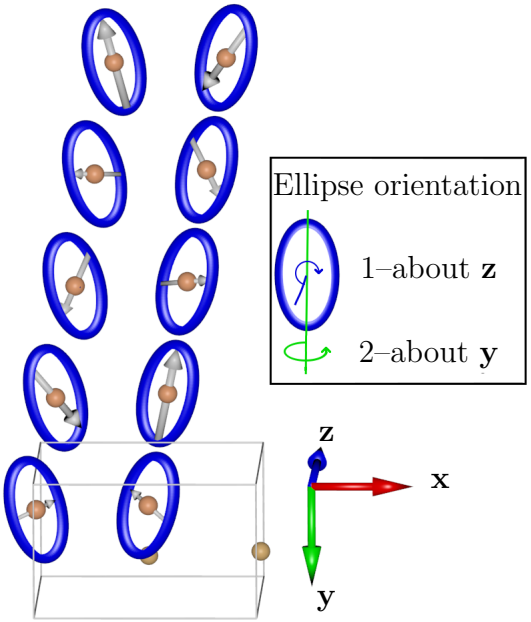

Figure 4.8: The proposed spin structure of FeAs, with arrows represeting the spin-direction and magnitude on Fe_1 and Fe_2 in successive unit cells. Blue ellipses around the atoms show the permitted amplitudes around the respective atoms for any given spin orientation. (image needs modification)

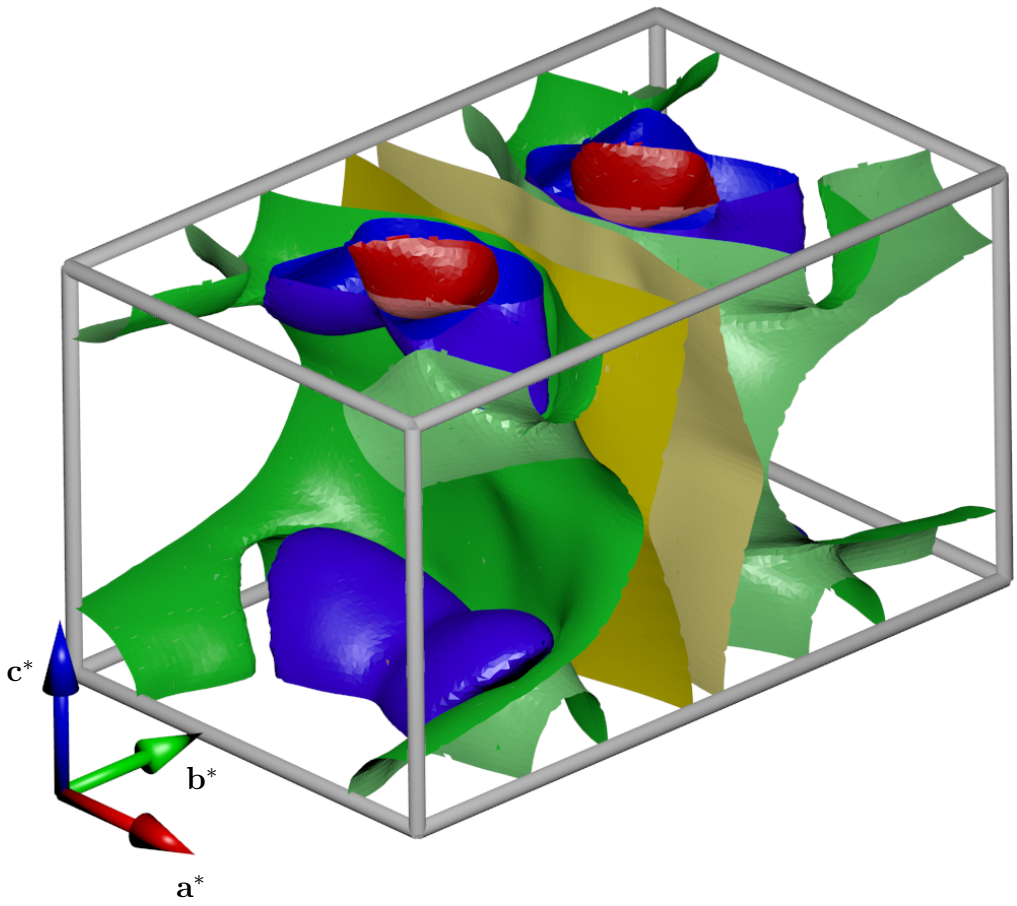

Figure 4.9: The Fermi surface for the zero-spin calculation, showing crossing bands 1 (red) through to 4 (yellow). Unoccupied bands are on the lighter side of each surface.

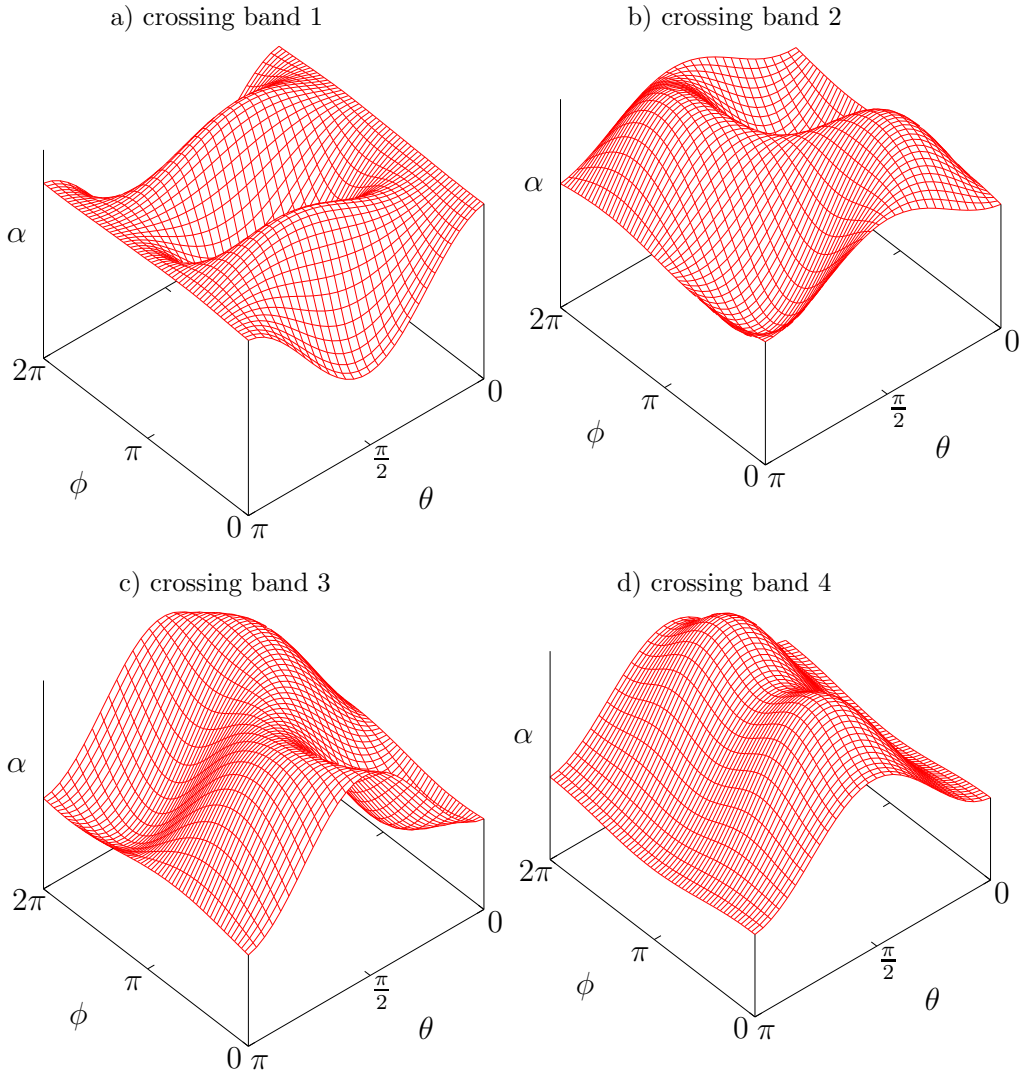

Figure 4.10: Orbital susceptibilities presented by band, calculated using equation 4.2.4.

otherwise forbidden satellite peaks. This proposed structure shown in fig. 4.8 generates a testable hypothesis; that the forbidden peaks are predominantly the result of magnetisation in the **c**-axis. This has been verified by X-ray scattering results [47], which found that the satellite peaks are entirely polarised in the **c** direction. Further these satellite peaks are found at [0,0,1$\pm q$], providing evidence that they are related to the helical magnetic order in the **a**-**b** plane.

The success of the above argument about moment-canting motivates us to examine the electronic structure to provide a theoretical justification. Usually spin-orbit interactions are weak in iron, but as the wave-vector of the magnetic spiral order changes with temperature, this constitutes evidence that the magnetic order is sensitive to small perturbations. To this end I applied the LS-perturbation technique detailed in section 4.2.2 to the spin-zero DFT calculations, as this will probe the orbital structure in iron arsenide. The choice of the nonmagnetic calculation means that I will only obtain qualitative results, as the band masses and gradients will be incorrect. However as the character of the orbitals will remain the same after reformation, the calculation will be an accurate probe of how the iron d-orbitals interact with the local crystal environment. I expect the iron d-orbitals to drive the magnetic structure, as the magnetism occurs on the iron atoms, and of the iron orbitals the d-orbitals comprise the largest component of bands around the Fermi surface [48]. The Fermi surface is shown in fig. 4.9. The results of the LS-perturbation on this Fermi surface are shown in fig. 4.10, of these bands crossing bands 3 and 4 (the green and yellow surfaces in fig. 4.9) give much larger responses, as their Fermi surfaces are large and they have a higher density of Fe d-orbitals. On band 3 the highest energy perturbation occurs when the Fe spin points in the **a**-**c** plane, at an angle of 23° from the **c**-direction (towards **a**). I find that spin alignment along the **b**-axis is energetically unfavourable. The results for band 3 compare favourably with the measured susceptibilities in the high temperature paramagnetic spin state, in which $\chi_{\mathbf{a}} \approx \chi_{\mathbf{c}} > \chi_{\mathbf{b}}$ [149].

While fig. 4.10 gives useful information about the angular dependence of the suscept-

ibilities, it does not give information about the directional anisotropy of the susceptibility, as α is represented only in arbitrary units. Instead to discuss this, I calculated the anisotropy from the second order correction energy $\alpha(\theta, \phi)$ as $(1 - \alpha_{\min}/\alpha_{\max})$. This quantity, on band 3, is high in the **a**-**c** plane, at 81%. This means that the local environment strongly affects the Fe *d*-orbitals in this band. The other bands have anisotropies of 77% (band 1), 51% (band 2) and 97% (band 4). For crossing band 2 the lowest energy spin direction lies exactly midway between **a** and $-$**c**; and in crossing band 4 it lies along **c**. The moment on the iron cannot satisfy all of these conditions simultaneously, but by far the largest proportion of *d*-orbitals lie on crossing band 3. However, it is notable that the optimal direction of spin alignment lies off-axis in the **a**-**c** plane, and that spin-orbit effects will couple ordering in the **a** and **c** directions, with the relative orientation dependent on the iron site.

From this I conclude that the orbital structure around the iron atom at the Fermi surface is anisotropic, as a result of the distorted arsenic ocatehdra around the iron. This provides a theoretical justification for the canting of the spin into the **c** axis, in a form that will break the screw symmetry in and allow otherwise forbidden satellite peaks to be observed.

4.3.2 Mechanism of magnetic order

Non-collinear calculations of iron arsenide were unable to reproduce the spin-spiral in the material [161]. However while DFT is unable to model this phenomenon, I do expect it to inform the type of physics present in the material. Both the AFM and zero-spin calculations give Fermi-surfaces in iron arsenide, in agreement with conductivity measurements which found that the material remains a conductor through the onset of magnetic order [162]. The Fermi surface undergoes a large change, from 4 bands in the zero-spin calculation to 2 in the AFM calculation, this is consistent with the multiple changes of the dominant current carriers as the material is cooled.

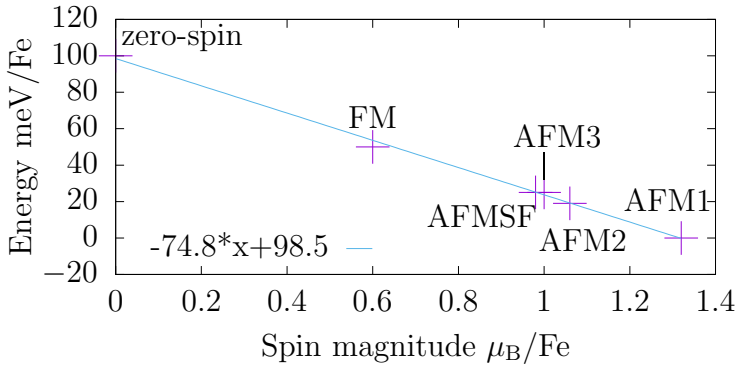

Figure 4.11: Comparison of relative energies and spin magnitudes for different states calculated with PBE, which show an almost linear relation between the two. The AFMSF state has varying spin magnitudes, so the mean value of these is used.

Collinear spin-polarized calculations were performed on iron arsenide. Under collinear constraints there are 5 possible magnetic configurations in the unit cell, for all spin parallel-antiparallel pairings in the unit cell. There are three antiferromagnetic states, a ferromagnetic state (FM), and a ferrimagnetic state where one spin is flipped from the FM state (AFMSF). The antiferromagnetic states are identified by the iron atoms which have parallel spins: $Fe_1 \parallel Fe_3$ (AFM1), $Fe_1 \parallel Fe_4$ (AFM2), and $Fe_1 \parallel Fe_2$ (AFM3). The relative energies and ordered spin moment for these states and the zero-spin state using PBE are shown in Figure 4.11. These agree with previous calculations [48]. The LDA results follow the same trends as the PBE results, but with lower ordered moments.

The magnitude of the ordered moment is found to increase with the number of antiferromagnetically aligned pairs of Fe moments. I also find that the energy of the states varies linearly with ordered moment. The energy relative to the AFM3 state is best fitted by $E = \gamma \sum_i |s_i| + \beta$, where the sum is over spins i, $\gamma = -74.8$ meV/μ_B and $\beta = 394$ meV. The observed linear energy dependence on spin magnitude contrasts sharply with the Heisenberg and Ising models which have a quadratic energy dependence, and is instead reminiscent of a Stoner instability as found in ferromagnetic metals [163]. Examination of the electron density in the system also shows that it changes with the transition to the ordered spin-state. From this I

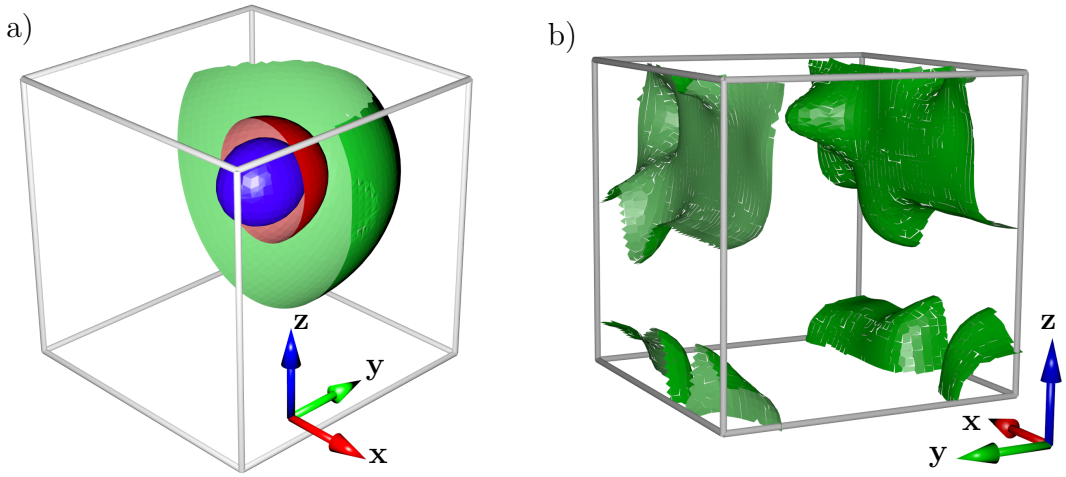

Figure 4.12: a)Isosurfaces of the potential experienced by the Fe_2 atom moving independently from the rest of the nuclei. Silver bounding box indicates the limits of the calculation, each edge is of length 0.2Å. The centre of the box is the coordinate observed by Selte [142]. Isosurfaces are at energies of 50, 100 and 300 meV. b) Isosurface of the sum of the spin-moment magnitudes of the iron atoms. Silver bounding box is as for a). Isosurface is at 3.5 μ_B, moments are small on the light side of the isosurface.

conclude that despite the absence of nesting in the calculated Fermi surface, the magnetic order is likely still driven by a reorganisation of states at the Fermi surface.

4.4 Discussion

Because the Fermi surface is highly distorted by comparison to nearly ideal metallic Fermi surfaces such as that of sodium, and because the bands at the Fermi surface have both hole and electron character, iron arsenide can be described as a correlated metal. The restructuring of the Fermi surface through the different magnetic orders indicates that it is closely linked to the magnetic order. This indicates a similarity with the incommensurate magnetic order found in chromium. In chromium this order can be explained using using the random phase approximation [49, 50] in a calculation of the susceptibility. In this case the susceptibility of the electronic structure to a periodic perturbation of wavevector $\boldsymbol{\lambda}$ can be estimated in DFT by

using the nesting vector technique, as the perturbation will cause orbitals seperated by a wavevector $\boldsymbol{\lambda}$ in reciprocal space to combine, and in so doing the energy of the system changes. This method can be used to detect a Stoner instability, as when the perturbation response of the system is large enough, the first order response will itself drive a larger second order response (and so on).

However this method has not been successful for FeAs [48]. Despite this, the strength of the local moment on the iron atoms is linearly correlated with the energy of the state, a behaviour that is found in magnetic structures driven by a Fermi surface Stoner instability [163]. This is possibly because while in chromium the density of states at the Fermi surface is 0.06 $\mathrm{eV}^{-1}\mathrm{Å}^{-3}$ [144, 50], in nonmagnetic FeAs the density of states was calculated to be more than double at 0.13 $\mathrm{eV}^{-1}\mathrm{Å}^{-3}$. Additionally the energy difference between the AFM states in chromium was found to be around 10 meV (per Cr) [144] whereas in FeAs I find it to be 19 meV (per Fe) between AFM1 and AFM2. This implies a larger reorganisation of states around the Fermi level between magnetic calculations in FeAs. The failure of a nesting-vector argument does not rule out the Fermi-surface as the principle driving mechanism, as the Lindhard function only calculates the response of the electron gas to first order, and has been calculated under the assumption that the energies associated with the applied perturbation λ are very small so that $\int \delta\lambda \frac{\partial E}{\partial \rho}\frac{\partial \rho}{\partial \lambda} << \int \delta\lambda \frac{\mathrm{d}E}{\mathrm{d}\lambda}$, as $\delta\rho \approx 0$. [48]. Under the above conditions, and given that the magnetic order is both helical and elliptical, it should perhaps be expected that a collinear spin state with one magnetic moment is not a good starting point for a Lindhard susceptibility argument, in the same way that the ferromagnetism in iron cannot be described by this method [164].

The reorganization of electronic states at the Fermi surface is corroborated by differences in electron density between the non-magnetic and magnetic calculations, shown in fig. 4.2. Relative to the nonmagnetic calculation, the magnetic calculation has reduced density between the Fe pairs 1&2 , and 3&4. This electron density moves to the Fe-As bonds between Fe_n-As_n pairs. However due to the Hellman-Feynman theorem the forces on the nuclei and their projected positions will change as well [165].

While a shift in the iron position as the material enters the magnetic phase was not observed in X-ray or neutron studies, Mössbauer studies did observe qualitative differences in the iron environment between the disordered and ordered phases [153]. Additionally they found that the onset of magnetic order was accompanied by an enhancement in the recoilless fraction, measured as the fraction of iron nuclei that remain stationary after the emmision of a gamma ray. This indicates that the single iron atoms are able to transfer momentum to the rest of the material more effectively, and that the magnetic order does in fact interact with the crystal structure.

If the magnetic and crystal structures are linked, I can study this with DFT. To this end I calculated the local potential of the Fe_3 atom for both the zero-spin and antiferromagnetic states. Isosurfaces of the zero-spin potential are shown in fig. 4.12 a). This shows that the potential is slightly anisotropic as the surfaces are ellipses, and indicates that the electronic structure does not change dramatically under motion of the Fe atom. The calculations of the potential on the antiferromagnetic states required the breaking of symmetry conditions. This led to a scatter of different energies, similar to that found in ferromagnetic iron in section 5.2. However the potential isosurfaces remained mostly unchanged from the zero-spin calculation. In these calculations however, it was found that the spin of the unit cell changed as the Fe_3 atom was moved around the unit cell. I also examined the sum of the spin moment magnitudes in the unit cell, as I found this was a useful proxy for the energy of the spin ordering of the system. An isosurface for this property of the iron atoms is shown in fig. 4.12 b). Due to the relaxation of the symmetry, there was a fair amount of scatter in the magnetisation as well. However one can discern certain trends, as motion of the atom in the x-z plane, or in an x-y plane translated by [0,0,-0.1Å] from the lowest energy position, causes little change in the sum over the spin moment magnitude. However motions away from these areas leads to a fall in the sum of the iron atoms' spin moment magnitude. This means that the magnetism is linked to the crystal structure of the lattice. The energies implied by these shifts in the spin moment are comparable to the energies of the zero-spin motions, with the

isosurface in fig. 4.12 corresponding to an energy of around 130 meV. On the basis that the nuclear position and the spin moment magnitudes are linked, it is therefore at least plausible that this could be due to interactions between the position of the iron nucleus and the magnetic order in the system.

4.4.1 Emergence

This study is predicated on the experimental results about the nature of the magnetic order in FeAs. Without that knowlege, the method of orbital projection would not have been performed. However while this appears to be "novelty" in the sense of emergence, there is no reason to suggest that all methods would be unable to predict the noncollinear structure *ab initio*. This is because the calculations that were used to justify the presence of canted moments were based on non-spin-polarised calculations. Taken on their own these calculations do not mean that a full noncollinear magnetic calculation will exhibit canted moments. This explanatory set-up this cannot be considered an example of historical emergence, as the novelty arises from an inadequacy of the "laws" used in the model collinear calculations.

I conclude that magnetic order in FeAs arises from a Fermi surface instability, coupled with a distortion of the crystal lattice.Under this model, each of the different periodicities and their associated canted structures share the same physical mechanism. It is therefore not the case that each of the different magnetic orders in FeAs need to be treated differently, and so there is no reason to think that a historically emergent explanatory set-up exists, which relates to the different magnetic periodicities. However there are specific phenomena in FeAs that deserve a discussion; the low-temperature susceptibility when cooled in a magnetic field, and the observed chirality of the magnetic order [47]. Each of these behaviours are particular to the magnetic state in FeAs.

The low temperature magnetic susceptibility $\chi_{\mathbf{b}}$ differs between when the material is cooled in a magnetic field, and when it is not [149]. This was attributed to small

regions in which there is a different magnetic order to that of the bulk. Presumably the presence of the magnetic field stabilises this phase in certain regions of the material. What is particularly interesting about this phenomena is that it is robust, as both field-cooled and zero-field-cooled measurements were performed in a magnetic field of the same intensity. This means that the magnetic properties of the material are path-dependent, so that different structures can be stabilised as the sample is subjected to different temperatures and magnetic fields. Since the dominant interaction between the magnetic field and the sample is via the term $\mathbf{B} \cdot \mathbf{S}$, it is likely that these structures are stabilized and "frozen in" at the temperature the susceptibilities begin to diverge. The divergence in the susceptibility is seen in the so-called spin glasses [166], and it is possible that structural defects in the crystals change the properties of the magnetic phase [150]. The temperature at which the susceptibilities diverge is around 50 K, 27 K below the transition temperature T_{N} =77 K, which means that above this temperature the system is ordered, but is also fluid in the sense that it is possible to move from one structure to another without a significant barrier. It is possible that this is indicative of interesting behaviour and dynamics in FeAs, although in the current absence of a full model of the material's magnetism more experimental investigation is needed to determine if these structures are of interest to a student of emergence.

A probe of the electronic states of FeAs indicates that it is chiral. Moriya has observed that a preference for a specific chirality must come from interactions between electrons and the effective magnetic field that they experience [167]. This means that in iron arsenide, spin-orbit coupling could provide an explanation for the chirality. Another explanation could also be the interaction of the spin with a macroscopic field generated by electron currents on neighbouring atoms, but this is likely very weak as the magnetic order is close to antiferromagnetic in iron arsenide.

4.5 Conclusions

FeAs forms a spiral magnetic structure. On the basis of symmetry arguments and anomalous diffraction peaks that have been observed [47], a modified magnetic spiral structure was proposed in which the spins were canted out of the a-b plane into the c-direction. Using DFT calculations I show that the d-orbitals around the iron atoms are susceptible to anisotropic perturbations off-axis in the a-c plane. A potential source for these perturbations is interactions between the spin and the motion of the electrons.

I have also performed calculations to asses the origin of the magnetic order in FeAs. Under DFT the magnitude of the spin moment on the iron atoms is linearly correlated with the energy of the magnetic configuration, and this suggests that the magnetic order has its origins in a Fermi surface instability despite the failure of a nesting condition [48]. If this is the case the instability will likely also redistribute the electronic charge in the material, and this in turn will affect the crystal symmetry of the material. There is additional evidence of this from Mössbauer studies [153], and using DFT calculations I was able to show that the electronic state and the position of the iron nuclei are closely linked. From these considerations, it seems that the origin of magnetic order in FeAs is similar to that in Cr, even if the nesting condition of the Fermi surface is not satisfied.

From this it is difficult to definitively point to a property that can be described as emergent in FeAs. Since I conclude that the crystal structure and the magnetic order are linked to each other, their behaviour cannot be seperated into different parts; they share a common cause. This means that the helimagnetic structure is fully and singly determined by the nuclear positions in the material. Since the structure is uniquely determined, under the definition of emergence I have proposed, it is not emergent. Finally that the crystal lattice symmetry is broken, it is a non-starter for levels-based emergence, since any lower level in the material is deformed, and the periodicity of the crystal lattice is destroyed by the magnetic order. However there

are a number of phenomena that indicate there is further complexity in FeAs that may be related to emergence, in particular the formation of novel structures that arise when the sample is cooled in a magnetic field.

Future experimental work on FeAs could involve revisiting neutron diffraction studies on the magnetic structure, to determine if the $[0, 0, 1 - \tau]$ peak observed at 40K in XRES studies [47] is only found in the orbital structure of the material, or if it is also found in the spin even if it is only a minor contribution. A closer study of field-cooled samples would also be of interest, to determine the thermodynamic properties and robustness of the structures that increase the susceptibility. From a theoretical perspective, if the magnetic order is linked to the structure of the crystal, it should be possible to replicate this in DFT. This could be done by simultaneously performing a non-collinear calculation in tandem with a structural relaxation. Finally while work performed here suggests that interactions between electron spins and the orbitals are present, how this occurs is unclear. It is possible that they play an important role in how the magnetic order is formed. However it is also possible that the system performs like a simple broken-symmetry system that can be treated under Landau theory, such that the observed preference for right-handed chirality was only a result of the measured sample's particular state at the time of the experiment.

4.5.1 Philosophical conclusions

It seems that there is no reason to expect that explanations of iron arsenide's behaviour are historically emergent in a meaningful way. This is because although the periodicity of the magnetic order changes as it continues to be cooled below T_{N}, these changes do not appear discretely. If each of the magnetic periodicities were discrete, semi-stable and displayed a hysteresis as the temperature changed, then it might at least be possible for the dynamics of the different orders to be separable and qualitatively distinct [168]. Instead the periodicity varies continuously with temperature, and this work indicates that it is unlikely that the dynamics

qualitatively change many times as the temperature is lowered.

The only behaviours of FeAs that might reasonably lend themselves to an account of historical emergence, are the promises of complex behaviour that originate in the zero-field/field cooling experiments [149]. These imply that upon the application of a magnetic field, as the material is cooled through the magnetic transition, different structures will form. However it is not yet clear whether it would be meaningful to isolate and analyse an exact instantiation of any of these structures. While there may be specific objects of interest, like the form of boundaries between the structures, there is no gaurantee that these would display historical emergence. Put another way, while one might be able to construct an experimental set-up that could support a vast number of different microstates, it is not clear what the value of such an experiment would be or if each of these microstates would have important, qualitatively different properties.

For these reasons it is not appropriate to treat iron arsenide as a system that displays historical emergence. Instead it appears that the complexity of the system lends itself towards a consideration using Batterman's theory of emergence, in which the quality of the physical description changes and instead of individual electrons some quasiparticle or perhaps long-range magnon quasiparticle is used. The only conclusion that one can come to is that any particular structure which may be observed in field-cooled system, is not likely to be repeatable. While such a system would very likely be historically emergent, unless these magnetic defects were shown to be long lasting and robust so that they might be put to practical use, a close study of these systems and their dynamics and behaviour is unlikely to be performed.

Chapter 5

Spin initialisation in noncollinear DFT

Although there is no guarantee that the same functional of the ground state can be applied to different magnetic configurations, in practice DFT can model many different metastable magnetic magnetic configurations, which are manifestly not ground states [78]. However this flexibility raises a problem, as in a particular calculation although while one might aim to calculate the properties of a specific magnetic configuration, due to the multiplicity of different metastable configurations the density search algorithm may return the configuration of a different local energy minimum.

To investigate systems, in the application of DFT it is important to implement a method of spin initialisation which can drive the density search algorithm towards a specific configuration. However there are important differences in the technical application of DFT methods to collinear and noncollinear systems. In collinear calculations it is possible to fix the net spin moment of a system, by varying the Fermi energy, for each of the up and down bands. In noncollinear systems all the electrons form a single system, so this is not possible. Instead only methods which change the spin and charge densities that determine the KS Hamiltonian can be used. As was detailed in the introduction to chapter 4, it is most often noncollinear

systems that are though to host emergent phenomenon, and so it this area deserves special attention for the purposes of this work.

A number of methods of spin initialisation have been developed for noncollinear systems [54, 55, 56, 57, 58], but they usually enforce strong constraints on the permitted charge and spin configurations and these may consistently bias a calculation towards an incorrect configuration. It is particularly important to avoid such a bias in noncollinear systems which are often frustrated or sensitive to small perturbations, as for these systems a small initial bias can be decisive. To address this problem I develop a new spin initialisation method which I call the spin setting procedure, based on a Wick rotation of the exchange-correlation potential. This biases a calculation towards a specific spin configuration using a perturbation based on the exhange and correlation energies intrinsic to the system. As the calculation approaches the desired configuration, the method reduces the magnitude of the corrective perturbation and allows the convergence algorithm to explore the space of states near to the desired spin configuration.

Here I detail the spin setting procedure and apply the method to a pair of well understood collinear systems, elemental iron and manganese oxide, to test if the method is able to initialise the desired spin state in certain conditions. I find that in manganese oxide, which has a metastable configuration quite robust to perturbations, this initialisation procedure is too weak to force the search algorithm towards the desired configuration. However in iron it is effective at initialising the correct orientation and desired magnetic configuration. In the application of the spin setting procedure to these magnetic systems, there is evidence for historical emergence. It is not found in manganese oxide, with its stable configurations, but in iron. This is the case because there are a multiplicity of different self-consistent and metastable states that the iron system can be found in, if the crystal symmetries are relaxed.

5.1 A method: the spin setting procedure

When magnetic materials are treated under DFT, there are often many magnetic configurations that are metastable. As a result it is often necessary in a calculation to bias the outcome of the calculation, so that a specific configuration is found. The usual method for collinear calculations relies on the separation of electrons into two coupled band structures, one each for electrons of up and down spins. Different Fermi energies can be set for each of these bandstrucutres, which allows the user to manipulate the total spin density. However this method is not available for noncollinear calculations, since all the electrons are treated together in a single bandstructure. Instead other methods have been employed, such as: 1) modifying the noncollinear spin-polarization potential in the region around ions so that it is aligns along a certain direction [54, 55], 2) energetically penalising deviations from desired orientation [56], 3) initialising a trial state which superficially displays the desired spin configuration [57], and 4) generation of a trial wavefunction by application of an unphysical magnetic field that interacts only with the spin component of the wavefunction in the area around an atom [58].

However these methods come with drawbacks. One drawback, relevant for methods 1) and 2), is the assumption that the spin localised on specific atoms is aligned only in one direction. This is often a reasonable assumption; in addition to the atomic orbital effects discussed in chapter 5.4, in an itinerant system there is a kinetic energy penalty incurred when the spinor changes direction. As such spin density is locally correlated and tends to locally be aligned in the same direction. However there are magnetic materials in which some atoms, even though they are important to the mechanisms of spin order, host no net spin moment. Materials which exhibit Anderson superexchange [169], in which the atom over which the spin exchanges has no net moment, are good examples. In these sorts of materials, initialisation of the net spin moment along a specific direction will probably fail since there is no net spin moment around the important atom. A second drawback, relevant to systems

2) an 4), is that methods that change the energetic landscape have the potential to push the spin distribution of the system towards the wrong state. To compensate for such a failure, they often contain parameters that can be varied, but the parameters add to the complexity of the calculation and so it would be preferable to get rid of them. A third drawback relevant to methods 3) and 4), is that if one consistently initialises the wavefunction to a specific configuration, one may regularly initialise an incorrect configuration regarding either the spin or charge-density, especially in systems where the different spin configurations are sensitive to perturbation. These initialisations therefore require special attention to ensure that they do not regularly cause convergence to a metastable or otherwise undesired state.

In addition to these methods based on the initialisation of local moments, it is possible to constrain magnetic configuration with the imposition of symmetry. This method either involves the use of the usual symmetry transformations, albeit usually a restricted set as the spinor wavefunctions are altered by the symmetry transformations, or the use of generalised Bloch waves to account for incommensurate or long-range ordered states [170, 171, 56]. These methods have been very successful in their application to simple noncollinear states such as circular helimagnets [172, 173], as in addition to reducing the size and length of the calculation, they are able to effectively constrain the range of available magnetic states. However for other systems such as elliptical helimagnets, or those that include canting such as iron arsenide found in chapter 4, they are inapplicable as even with a rotation of the spin density, there is no symmetry operator aside from a periodic translation that makes the spin sites equivalent. Such a structure cannot be modelled with a reduced unit cell.

To provide an improvement, I have developed the spin setting procedure, based on the method of altering the spin potential [54, 55] that is designed to avoid the difficulty in application to systems in which the magnetic moment varies on the atom. In the method a bias to a chose spin orientation is acheived by rotating the noncollinear spin-polarization potential in the region around ions, by the same angle in the entire region. This means that the spin polarization is not biased to be

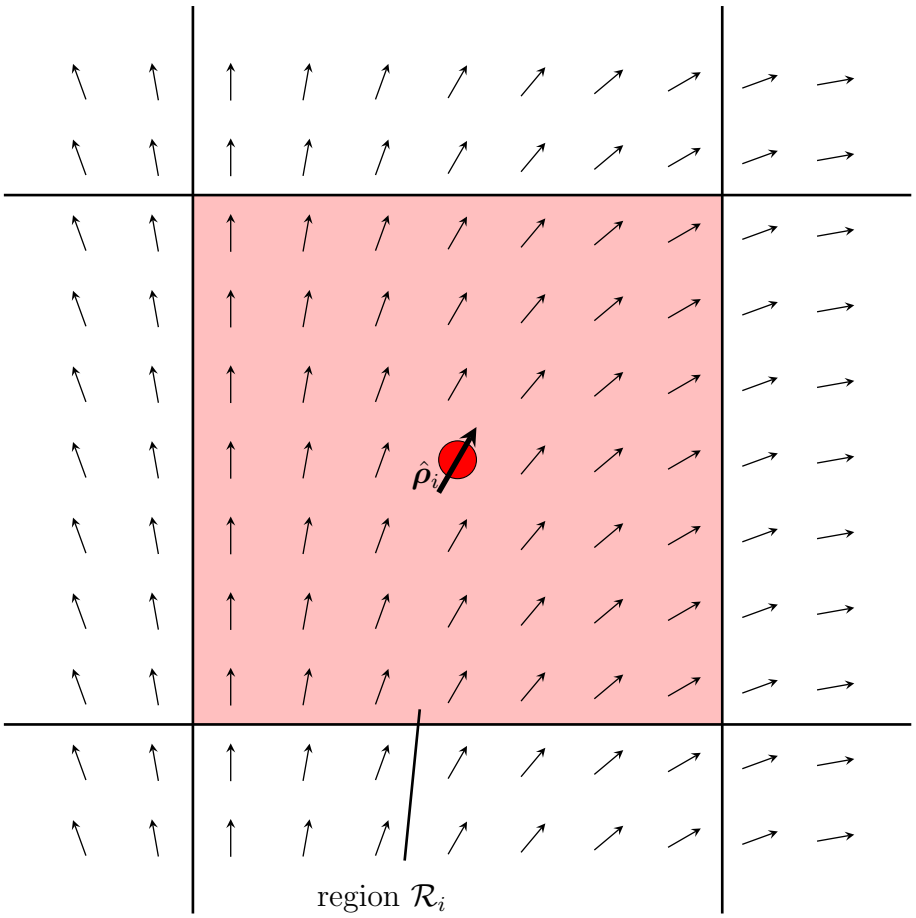

Figure 5.1: Illustration of ar region in an example square array of atoms, and the net spin of that region, as detailed in the spin setting procedure

aligned all in the same direction, but is free to deviate as the calculation approaches self-consistency.

Concerning the specific implementation, the volume of the unit cell is divided into regions $\mathcal{R}_i$ as shown in fig.5.1. For simplicity these regions are divided by the planes equidistant to the ions in a Wigner-Seitz construction[174, p. 118]. The purpose of the method is to align the net spin in each region along the chosen directions $\hat{\boldsymbol{\rho}}'_i$. In the calculation the total spin for each region $\boldsymbol{\rho}_i$ is calculated by

$$\boldsymbol{\rho}_i = \oint_{\mathcal{R}_i} \mathrm{d}V \boldsymbol{\rho}(\boldsymbol{r}), \tag{5.1.1}$$

where $\boldsymbol{\rho}(\boldsymbol{r})$ is the spin-polarized density of the electrons as defined in equation**??**.

From the the total spin density, the net spin $\hat{\boldsymbol{\rho}}_i$ is

$$\hat{\boldsymbol{\rho}}_i = \boldsymbol{\rho}_i / |\boldsymbol{\rho}_i|. \tag{5.1.2}$$

Rotation operators $\mathbf{R}_i$ are chosen so that

$$\mathbf{R}_i \hat{\boldsymbol{\rho}}_i = \hat{\boldsymbol{\rho}}'_i, \tag{5.1.3}$$

and these are used to create a rotated spin polarized density field$\boldsymbol{\rho}'(\boldsymbol{r})$ which is defined such that within each region i

$$\boldsymbol{\rho}'(\boldsymbol{r}) = \mathcal{R}_i \boldsymbol{\rho}(\boldsymbol{r}). \tag{5.1.4}$$

This modified field $\boldsymbol{\rho}'(\boldsymbol{r})$ is used in place of the usual spin polarized density field $\boldsymbol{\rho}_\sigma(\boldsymbol{r})$ in the calculation of the exchange correlation energy in equation 2.3.3. This method minimizes changes in the potential, and regardless of the spin structure around the atoms, the modification of the x-c functional to tends to zero as the orientation of the *net* spin polarisation around the atom tends to desired direction. In this way it contrasts with other methods that continue to affect the energetic landscape as a calculation reaches self-consistency.

A possible drawback to this method is the convergence onto a false state, for example one in which the spins of the K-S wavefunction anti-align with the desired spin direction. Fortunately such a failure is easy to check, as one should expect that over the duration of the calculation the angle of rotation of the spins tends to zero. If this condition is not satisfied, one will know that the state of the calculation is unstable if the spins are released, and therefore is not self-consistent, a condition required by DFT. There is a second drawback as well. The DFT Hamiltonian can be divided into three terms: the potential energy, the kinetic energy, and the x-c correction. Spin order can be determined by both the kinetic energy and the x-c correction. However the spin-alignment procedure only affects the x-c correction. Therefore in cases where the kinetic energy contributions are much larger than the x-c correction, the spin alignment procedure will be insufficient to bias the calculation towards the

desired configuration.

An important part of current DFT calculations is the convergence algorithm used to find a self consistent low energy state. As these form an important part of a calculation, I will test how the spin setting procedure is affected by the use of different density search algorithms presented in chapter 2.2.4. Also as discussed previously, noncollinear systems are sensitive to symmetry. However the effect of releasing symmetry constraints on noncollinear DFT calculations will change the efficacy of the convergence algorithm, as a relaxation of symmetry increases the number of directions in configuration space that the convergence algorithm must consider. In particular in noncollinear systems there are often many competing energetic phenomena and states, often with similar energies. In such cases it is not clear if the existing convergence algorithms will be effective at finding the ground state, or if they will interact with these multiple states, and so be unable to find a state, or instead find the wrong state. I will examine two common convergence algorithms, density mixing (DM) and (EDFT), and examine how they interact with symmetry-relaxed non-collinear systems.

There are therefore three things to investigate for the calculation of noncollinear magnetic phenomena in DFT. The validity of the spin setting procedure, the effect of relaxing symmetry, and the effectiveness of the convergence algorithms. In order to do this I have chosen two contrasting case studies, the conducting ferromagnet Fe, and the insulating antiferromagnet MnO, and applied these methods to a DFT calculation of their properties.

5.2 Method example: iron

5.2.1 Material background

To test the spin setting procedure, I calculate the properties of elemental iron. It has two stable cubic structures, either face (fcc) or body (bcc) centred [175, 176]. The

ferromagnetic bcc phase shown in fig. 5.2a) was chosen for the calculation as spiral magnetic structures in the FCC phase may complicate the calculations[177]. Like the other magnetic metals nickel, cobalt, and chromium, the magnetism arises from a Fermi surface Stoner-type instability of the nonmagnetic state, that leads to a reconstruction of the Fermi surface [144, 163, 154]. However the Fermi surface instability is insufficient to describe all the properties of iron, as it is not a simple electron gas; instead most of the magnetisation is localized around the iron nucleus [164]. In the magnetic phase, iron displays a spin-orbit dependent magnetic anisotropy which has led it to be the subject of noncollinear calculations ranging from rudimentary band-character calculations to ab-initio under DFT [178, 179, 180, 141, 181]. Due to the existence of previous noncollinear calculations, and the simple crystal and magnetic structure of iron it is a good test case for our implementation of non-collinear spin.

Since DFT calculations are usually ab-initio, it is not important to choose between different Stoner instability models. Instead the properties of bcc iron in DFT are strongly dependent on the choice of x-c functional. LDA predicts the wrong bulk properties for iron as calculations find that an antiferromagnetic FCC state is of a lower energy than the ferromagnetic bcc state [182]. This directly conflicts with experimental evidence in which the fcc state is only thermodynamically stable at high temperatures, although the PBE functional does obtain the correct relationship between the two [156, 183, 184]. These studies also show differences in the spin density between PBE and LDA, these are shown in the zero-spin density isosurfaces in fig. 5.2 b). In LDA, the spin on the iron atoms is, at 2.13 μ_B per iron atom, by comparison to 2.17 μ_B calculated in PBE. These are both similar to the experimentally observed value of 2.12 μ_B.

To compare the efficacy of noncollinear calculations, I first summarize the results of collinear calculations on iron. As an itinerant ferromagnet, the magnetism originates in a reorganization of the states around the Fermi level. In this reorganisation there is an accompanying change in the both the spin and the charge density through the unit cell. Isosurfaces for the changes in spin and charge density, when the zero-spin

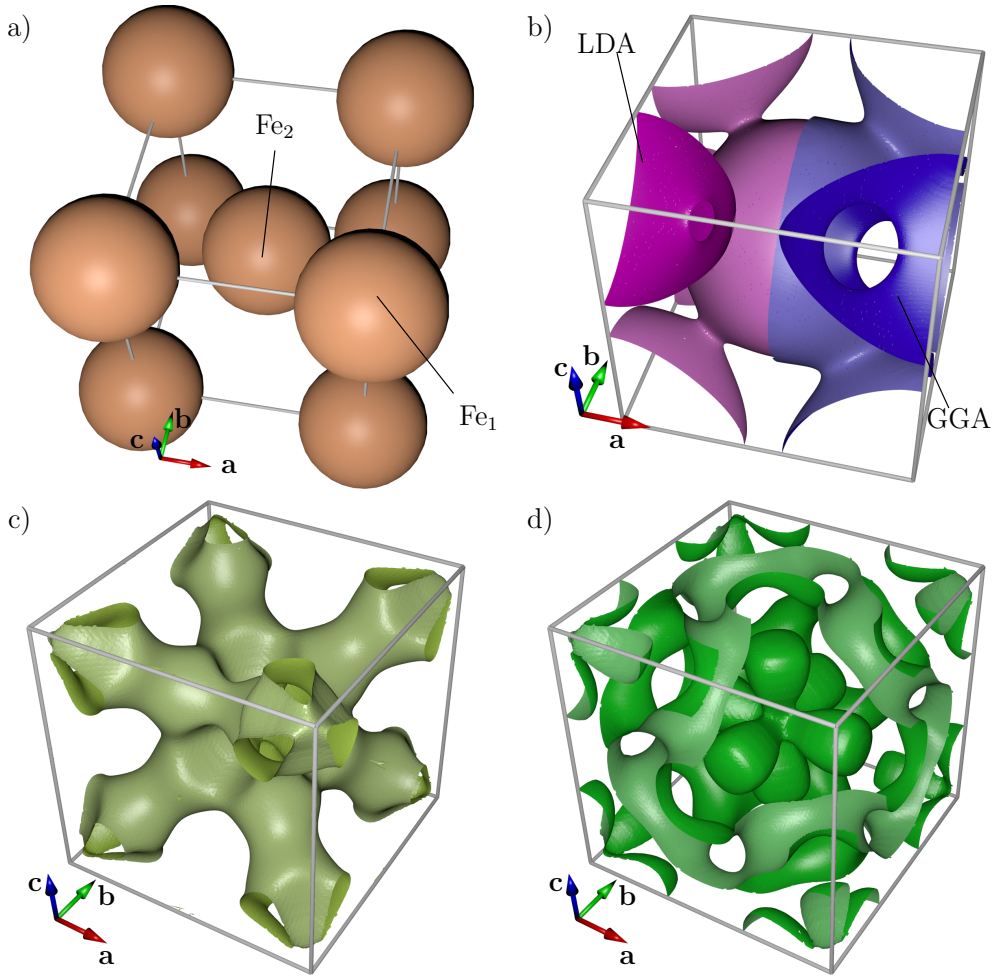

Figure 5.2: a) Structure of the unit cell of bcc iron. b) The zero spin density isosurface of BCC iron, calculated here using the LDA (left, purple) and PBE (right, blue) X-C functionals. c) Regions in which the charge density increases and d) decreases, upon transition to the magnetic state.

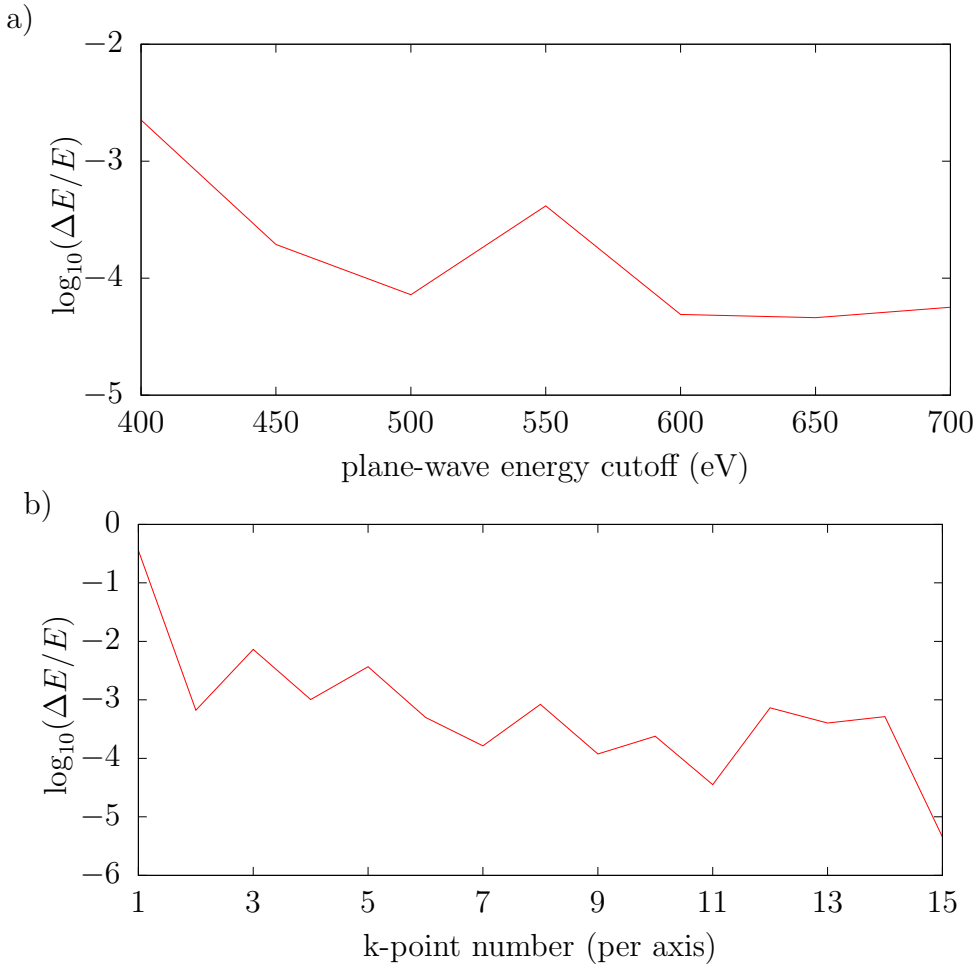

Figure 5.3: The convergence of energies between distorted states, as the a) energy cut-off of the plane waves is varied b) the number of kpoints is varied

constraint is relaxed in DFT calculations are shown in fig. 5.2 c) and d). From these changes in the charge density one can observe that the relaxation of the spin-zero symmetry principally allows the redistribution of electrons among the Fe d-orbitals and a slight reduction in the occupation of the s-orbitals. The d-orbitals with increased occupation are coordinated towards the iron nearest-neighbours, which increases the charge density on these bonds and reduces the interstitial density in the rest of the unit cell.

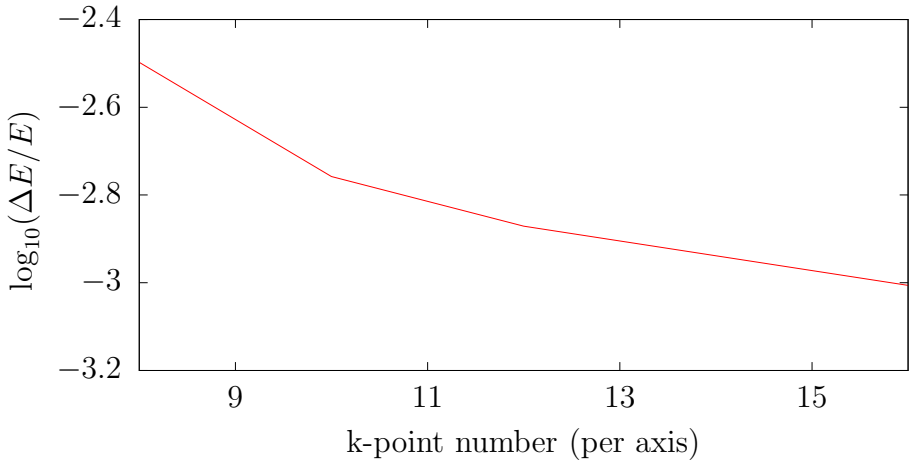

Figure 5.4: The convergence of energies between different the ferromagnetic and non-magnetic states, as the number of kpoints per axis is varied

5.2.2 Initial results

As a periodic crystal bcc Fe calculations under plane-wave code need to be converged with respect to the cutoff energy of the plane-waves and the kpoint density. Convergence calculations performed on bcc iron were performed to take the difference in energy between two similar structural configurations of iron, with the same symmetry. The values of these converged parameters are determined using the convergence function found in chapter 2.4. The convergence for the energy cutoff of the plane waves is shown in fig. 5.3 a). A plane-wave cutoff value of 600 eV will be adequate for an accuracy of 1 part in 1000.

Convergence with respect to the number of k-points is shown in fig. 5.3 b). Similar to the plane wave cutoff preliminary calculations based on a difference in structural conformations found that 512 k-points, corresponding to an $8 \times 8 \times 8$ k-point grid is adequate with an accuracy of 1 part in 1000, 0.3meV. However further convergence tests found that the difference in energies between magnetic (rather than structural) states converged more slowly. For energy differences between the spin-zero and ferromagnetic calculations, shown in fig. 5.4, an accuracy of 1 part in 1000 (again 0.3meV) is not reached until a $16 \times 16 \times 16$ kpoint grid is used. However in order to balance the load between computing resources and accuracy, for the inititial

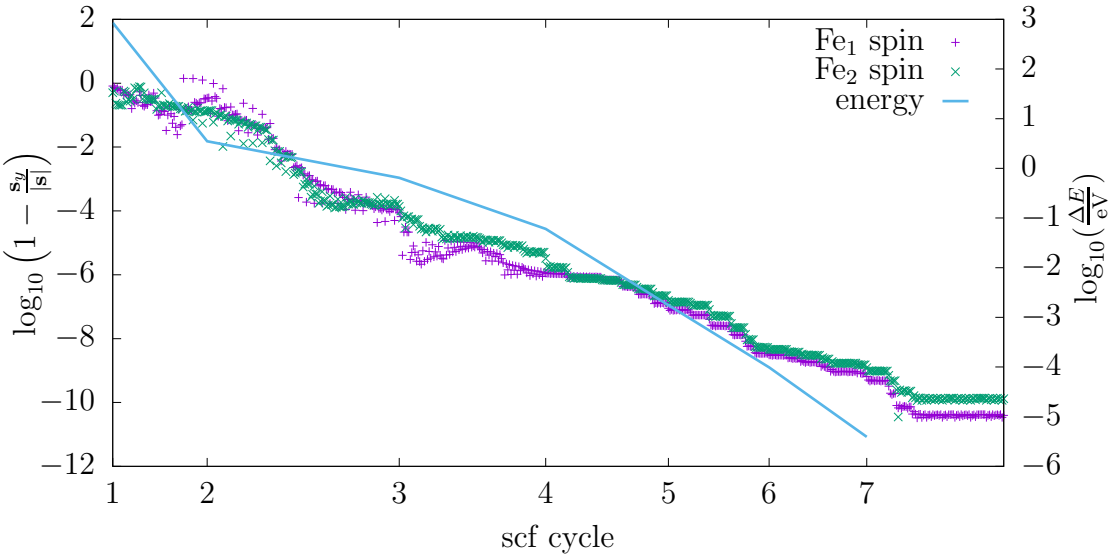

Figure 5.5: convergence of the spin onto the y-direction, using the spin-align method and EDFT.

calculations I used a $12 \times 12 \times 12$ k-point grid, which gives an accuracy of one part in 740.

The spin alignment procedure was able to effectively align the spin along a specific direction. The convergence of the spin onto a specific direction is shown in fig. 5.5 and this reveals two features. First is that it only takes 2 scf cycles under the EDFT, for the spin to align along the chosen direction from a random initial configuration to one part in 10,000. Second is that in the first scf cycle there is hardly any convergence at all, for while the Fe_2 atom has converged the spin to one part in ten, the Fe_1 atom is still unstable and jumps about through the cycle, sometimes reversing direction. The stabilisation of the spin moment and its alignment occurs in the second scf cycle, likely because in the first SCF loop most of the minimisation is due to changes in the charge density, since the Coulombic terms are much larger than spin polarisation terms in the x-c potential. While the charge density is still being minimised, the ensemble DFT (EDFT) minimisation algorithm used neglects optimisation of the spin-direction in favour of finding an accurate charge density. As can be seen in fig. 5.5, by the end of the first scf cycle the energy is converged to about 3 eV, and by the end of the second scf cycle it is converged to 0.5 eV. The energy at the end of the second cycle is less than the energy difference between the nonmagnetic and

	DM LDA	DM PBE	EFDT LDA	EDFT PBE
NCM*+A	no issue	non-convergent	no issue	scattered, other state
NCM*	no issue	non-convergent	no issue	scattered, other state
CM*	–	converges slowly	–	scattered, other states
CM	–	converges	–	converges single state

Table 5.1: Calculations performed on bcc iron, star indicates that no symmetry constraints have been applied. The "+A" calculation used the spin alignment procedure.

ferromagnetic calculations of 0.9 eV.

The remainder of fig. 5.5 shows that the spin alignment procedure is very effective at aligning the spins. By the end of the 7th scf loop the deviation flatlines at around one part in 10^{10}, a negligible quantity at the limit of double precision. Indeed further scf cycles lead to only very small reductions in the overall energy less than 10^{-6} eV. Such rapid and effective convergence shows that the spin alignment procedure does not affect the convergence to the lowest energy state of the system.

To test whether the spin alignment procedure made an impact on any of the calculation properties, three different types of calculations were performed: a standard collinear calculation with symmetry and occupancy constraints (CM), a collinear calculation with only occupancy constraints (CM*), and a noncollinear calculation with spin-settling (NCM*). Each of these types of calculation was performed with two convergence methods, density mixing (DM), and EDFT, and the two functionals, LDA and PBE. For each of these calculations, between 90 and 100 different initializations or spin-setting configurations was used. A qualitative summary from each of these calculations is found in table 5.1. The results show that the spin-setting procedure does not affect the calculation properties or convergence from the collinear calculations.

However the results show that the symmetry constraints in iron do not only reduce the cost of computation; they also affect the convergence to low energy states. For the LDA x-c functional there is no difference between calculations with or without the constraints. However for the PBE calculations, the relaxation of symmetry leads to differences between the DM and EDFT calculations. For the DM method the

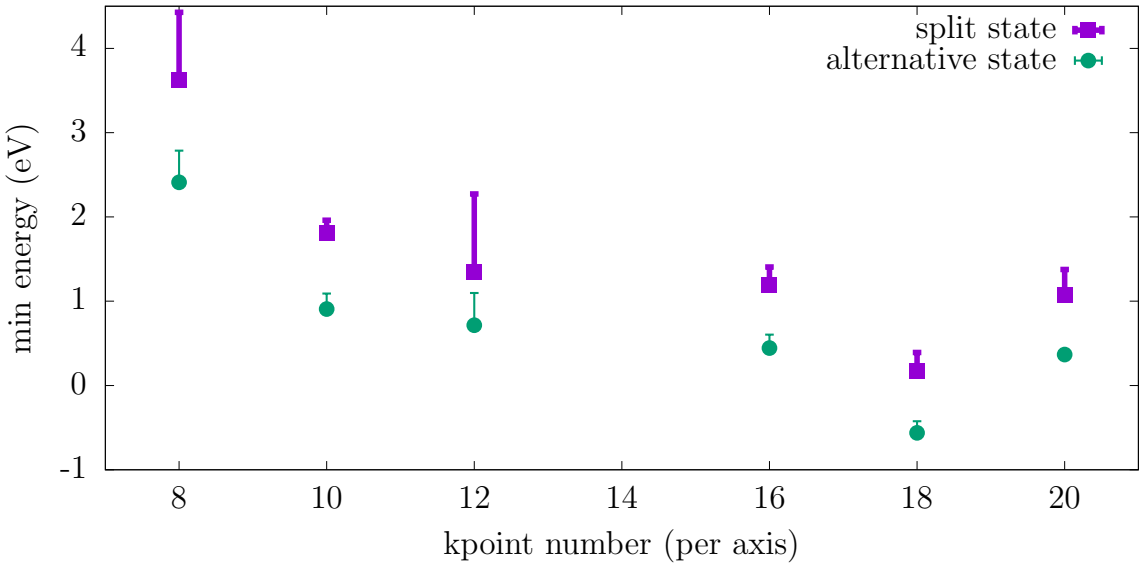

Figure 5.6: Energy differences between the principal bcc FM state, and the lowest energy calculations of the low-spin and split states against the number of kpoints per axis. The scatter of the states is indicated by the length of the bars, and calculated as the standard deviation of the associated energies multiplied by a factor of ten. For the 2nd bcc state at 20 kpoints, only 3 points and so the standard deviation is not calculated and is omitted.

relaxation of symmetry the algorithm converges onto the same symmetric state, though this requires a longer convergence time. The EDFT algorithm does not converge onto a completely symmetric state. Instead I find two features in the calculation results: there are a number of new low energy states that differ in energy by about 1 meV, and the algorithm converges onto a scatter of configurations which are localised around these low energy states. This energy difference is so small that I need to perform additional convergence tests. The differences between these magnetic configurations need to be examined, as small energy differences are often in noncollinear magnetic systems. I find three of these new states, two in the collinear calculations, and one in the noncollinear calculations.

5.2.3 New PBE states

Two new states were observable in the collinear calculations without symmetry constraints using EDFT and PBE. These can be distinguished from their energies

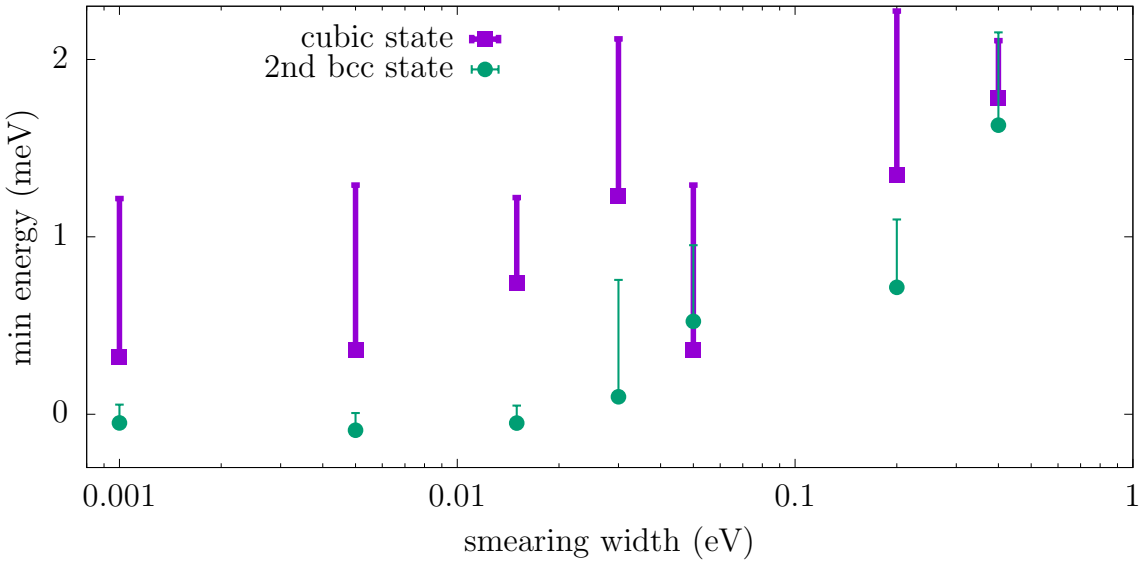

Figure 5.7: Energy differences between the principal bcc FM state, and the lowest energy calculations of the low-spin and split states against the smearing width. The scatter of the states is indicated by the length of the bars, and calculated as the standard deviation of the associated energies multiplied by a factor of ten.

and the spin densities on the Fe atoms. A state of energy 1.5-2.0 meV above the symmetric state was found in which the iron atoms were split into two distinct sites of atomic moments 2.24 and 2.26 μ_B, where the symmetry-constrained state had a moment of 2.23 μ_B per iron atom. I call this state the split state. The other state had an energy of 1.2 meV above the symmetric state, and retained the primitive unit cell of bcc iron but still broke cubic symmetries. It had a magnetic moment of 2.22 μ_B per atom. These two new states only obeyed inversion symmetry, possibly due to the inclusion of time-reversal symmetry as a the only remaining symmetry condition on reciprocal space.[1]

While there are differences in the number k-points required to calculate structural and magnetic energy differences in iron, the differences between these new states are small enough that they need to be converged in their own right. These states are very low-lying in energy and are strongly dependent on itinerant phenomenon,

[1]Spin polarisation in many DFT systems is the most important component of magnetic structure. This means I ignore the magnetic field as exchange-correlation, charge, and kinetic terms are much larger. Due to this the calculations preserve time reversal symmetry, despite the magnetisation.

so they must also be converged with respect to the smearing width of the EDFT algorithm. The smearing width is a tool that aids the convergence onto a single state in EDFT, because having a sharp cut-off in the band occupation at the Fermi level can lead to the convergence onto undesirable metastable states. However it is similar in its effect to raising the temperature of the material, and so for these low energy states that are dependent on small band shifts, it must be considered.

Since the converged energies can be extremely small, the formula for convergence in section 2.4 is not appropriate and so I compare the convergence of energy differences between states on a linear scale. For repeatability all energy differences are taken with respect to the symmetry-constrained calculation, as this does not display any scatter. For the convergence with respect to k-points in fig. 5.6, the convergence is slower than the convergences in section 5.2.2 and it takes until 20 k-points per axis to converge to within one-tenth of an meV. The convergence with respect to the smearing width calculated at 12 k-points per axis, is shown in fig. 5.7. The energy difference only begins to meaningfully converge to one-tenth of an meV when the smearing width is below 10 meV. Concerning the scatter of the different states, there is no meaningful trend as the k-points are varied.

Of particular note in these calculations is that independent random initialisations of the multi-electron wavefunction did not converge onto completely identical configurations. Instead each of the different states hosts a scatter of different similar configurations, so it is difficult to isolate the properties of each of the states. Further as show in fig. 5.7, as the different parameters are converged, the scatter does not disappear, although it does converge. Fortunately I found that the scatter is sufficiently small that the different states can be distinguished both by their energy and also by their magnetic configuration, so the particular properties of the state can be determined, on the condition that a large enough number of different randomly initialised calculations are performed. However this is undesirable as it considerably increases the computation load of the calculations, additionally if hidden in the scatter there are competing states of very similar energy, calculations like those

performed here are unable to isolate them.

The data suggest that the energy of the symmetric state was calculated to within 0.05 meV. Energy differences between these states were not converged with respect to the energy cutoff of the basis set. This was both because performing a convergence between these new states is costly due to the need to perform many calculations to confirm that the scatter does not bias the result, and also because it was already found that the energies between magnetic states were previously converged to one tenth of a milli-electronvolt at 800 eV. The convergence parameters required are equivalent with the calculations performed elsewhere, which found that 4000 k-points in the primitive unit cell ($13\times13\times13$ in the unit cell used here) gave an energy convergence of 0.5 meV per unit cell, and found that a smearing width (or effective temperature) of 0.04 eV gave a convergence of 0.5 meV per unit cell [172].

In order to find the origins of these low energy states, I must examine the details of their spin and charge densities. The difference between the symmetric and split states is shown in fig. 5.8. This shows that transition from the alternative to the split state increases the charge density in the second-nearest neighbour bonds between atoms with a lower spin moment magnitude. The charge density on the same bonds between the atoms with a high spin moment magnitude is instead reduced. This charge redistribution of the bonds appears to satisfy cubic symmetries. The cubic symmetry is only visibly broken close to the Fe nuclei, in which both iron sites show a redistribution of charge density in their d-orbital states. This reorganisation satisfies inversion symmetry, with the centre of inversion on the iron atom. The lobes of the d-orbital density increase are coordinated in the $\pm\mathbf{b}$ direction, and towards the second nearest neighbour bonds between Fe_1 atoms, which are parallel to $\mathbf{b}$. However the orientation of these lobes of density change do not obey a cubic symmetry. This behaviour of the d-orbitals is the same for both iron sites. The orientation of these regions is the same for both iron sites. The non-cubic redistribution of the core states contrasts with the approximately cubic redistribution of the charge density in the interstitial regions. What this implies is that these two phenomena are independent,

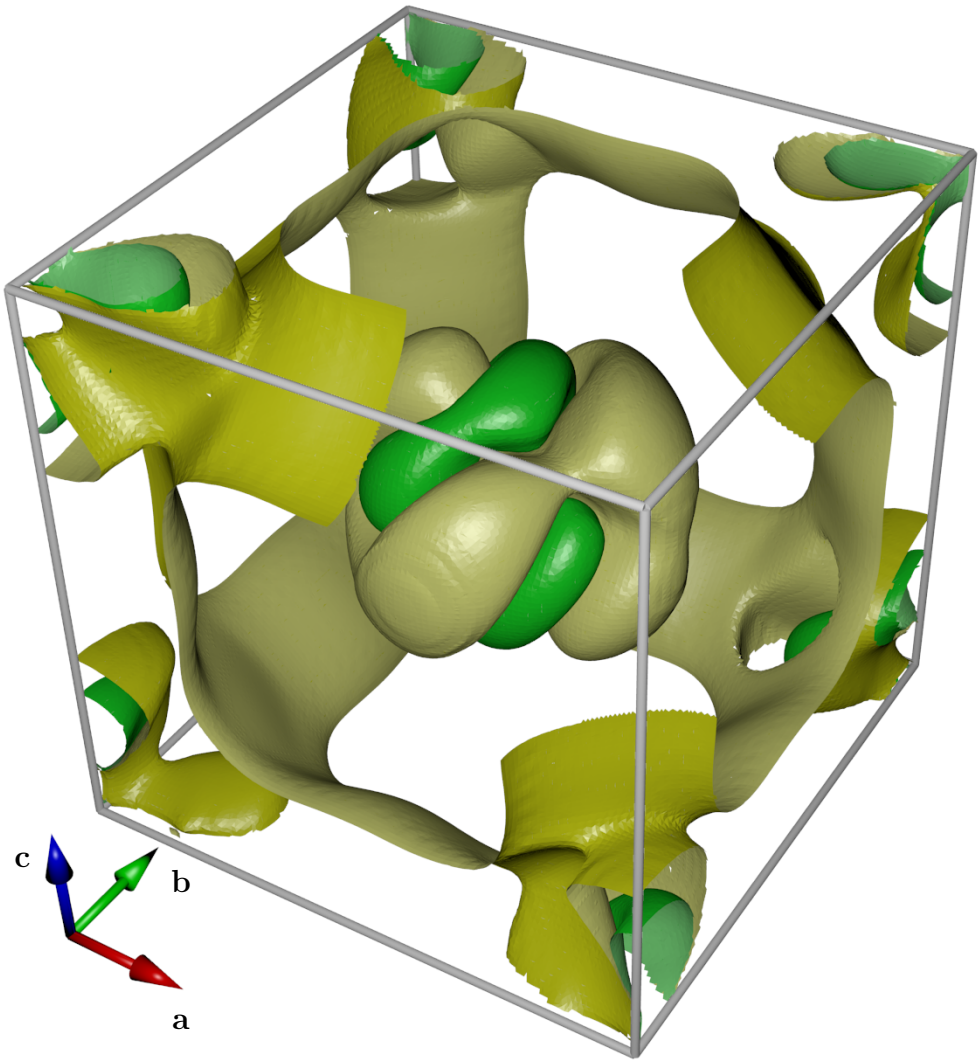

Figure 5.8: Density differences between the split and symmetry constrained states in PBE, computed as a change from the transition from the split to the symmetry constrained state. Shows selected regions of density change, yellow surfaces enclose regions of increase, green surfaces enclose regions of decrease, charge density increases more or decreases less on the darker side of the isosurface. Portions of surfaces in the octant of the unit cell closest to the viewer have been removed for clarity.

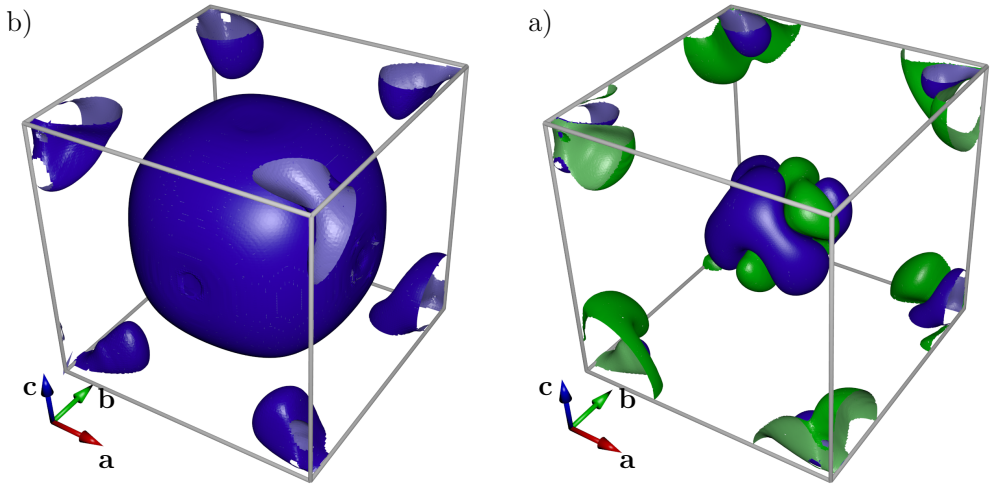

Figure 5.9: Spin differences between the split and symmetry constrained states in PBE, computed as a change from the transition from the split to the symmetry constrained state. a) zero-spin isosurface, spin density decreases in the regions on the bold side of the isosurface. b) selected regions of spin density change, blue represents regions of increase, green represents regions of decrease (Fe atoms have positive spin) In b) portions of surfaces in the octant of the unit cell closest to the viewer have been removed for clarity.

or at least represent independent responses of the material to a common cause.

As regards the spin in the split state, the difference between the symmetric and split state is shown in fig. 5.9. Most apparent from fig. 5.9 a) is the inequivalence of the Fe_1 and Fe_2 sites, as they have differing spin magnitudes. Like the interstitial changes in charge density the interstitial spin-zero isosurface roughly satisfies cubic symmetries and is similar in for the isosurfaces observed in the transition from the zero-spin to symmetric ferromagnetic states, shown in fig. 5.2 b). However this isosurface in the region between the atoms hides changes to the spin moment magnitude on the d-orbitals of the iron atom. It seems these variations near to the nucleus are likely related to the density changes, since they obey the same inversion symmetry, however the lobes are not aligned along any of the same directions. There are similar features on the low spin iron atom. While the spin densities changes near the nucleus are different between the two iron sites, it seems that they differ by only an almost constant shift in the spin polarisation, as they retain the same

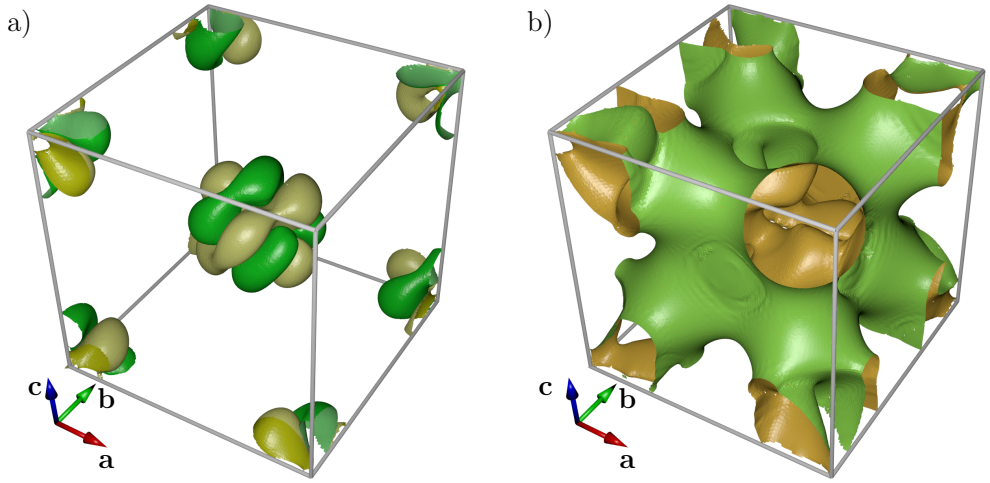

Figure 5.10: Charge density differences between the alternative and symmetry constrained states in PBE, computed as a change from the transition from the cubic to BCC state. a) Selected regions of density change, yellow surfaces enclose regions of increase, green surfaces enclose regions of decrease, charge density increases more or decreases less on the darker side of the isosurface b) isosurface of zero charge density change, regions on the yellow side of the face are regions of charge increase. In both images portions of surfaces in the octant of the unit cell closest to the viewer have been removed for clarity.

structure near to the nucleus. This behaviour provides evidence that this state is a combination of both independent itinerant and localised interactions.

The charge density changes for the alternative state are shown in fig. 5.10. The two iron sites are equivalent in this state. Outside the iron cores, a transition from the symmetric to the alternative state leads to small increases in the density of the nearest-neighbour bonds, and a small reduction in the density elswhere. However in the core of the atomic orbitals, the density changes are extremely similar to those present in the split state.

The spin density changes for the alternative state are shown in fig. 5.11. As for all the previous changes, these changes can be divided into core and interstitial structures. Outside the core, the spin density isosurface is very similar to the spin density isosurface from fig. 5.2 b), except this time the blue regions enclose regions of spin density increase. This means that there is a drop in the confinement of the spin

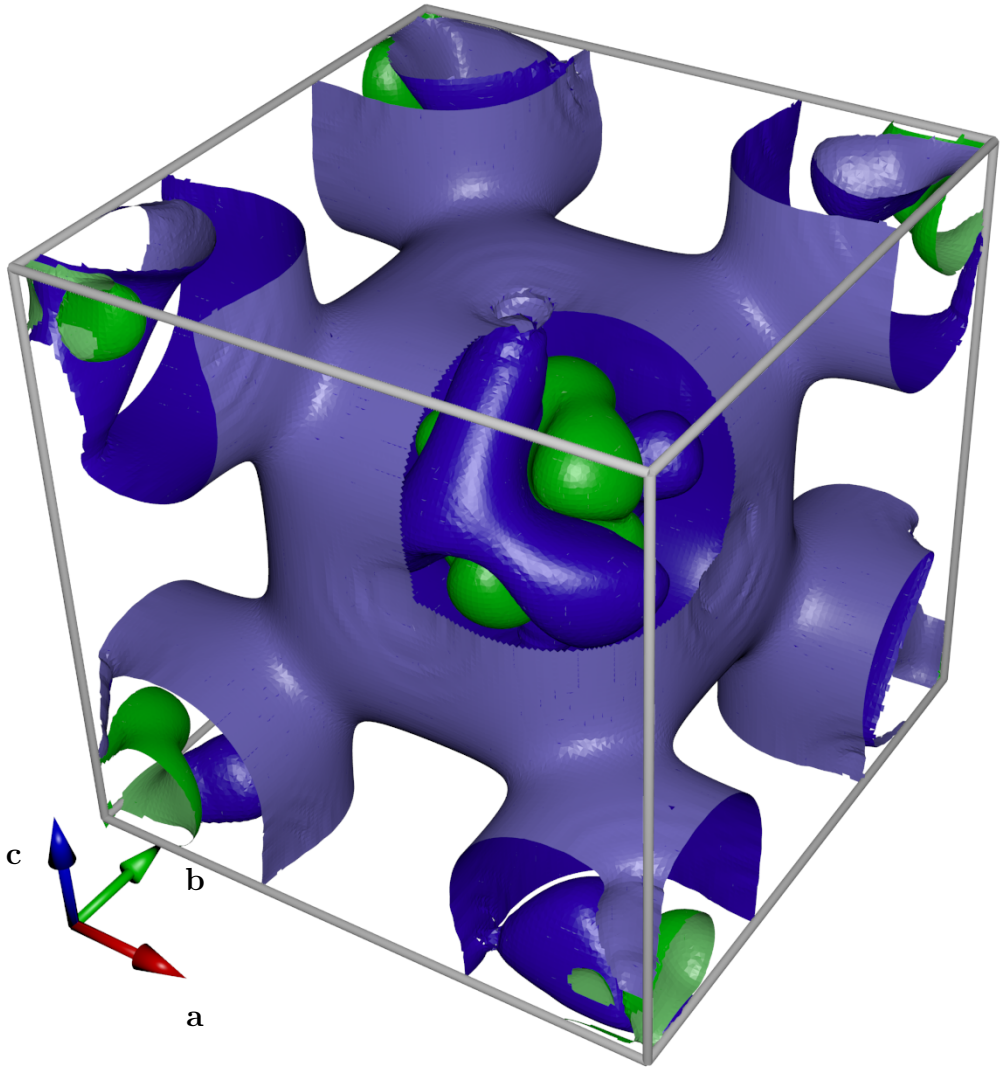

Figure 5.11: Spin differences between the alternative and symmetry constrained states in PBE, computed as a change from the transition from the cubic to BCC state. Shown are selected regions of spin density change, blue represents regions of increase, green represents regions of decrease (Fe atoms have positive spin). Portions of surfaces in the octant of the unit cell closest to the viewer have been removed for clarity.

density, as it moves from regions close to the iron atom to regions far away. Close to the iron atom, there are regions of both increased and decreased spin density. Both of these regions form structures with six lobes around each atom, which indicates the d-character of the orbitals involved. The isosurfaces almost show three-fold and two-fold symmetry, with the two-fold rotation about **b**, and the three-fold rotation about [1,0,-1]. However while the two-fold rotation is shared with one of the cubic four-fold rotations, the three-fold symmetry is not aligned along any of the cubic three-fold rotation axes.

From these results I can distinguish that there are two separable contributions to the differences between the states, a reconfiguration of the core states driven by localised d-electrons, and changes that affect the interstitial regions, which leave the cubic symmetry unchanged. The alternative state is very similar to the symmetry state in the non-core regions; it has the same magnetic moment, and only differs by a slight transfer of electrons from near the iron atom to regions further away. The only significant differences originate in the reconfiguration of d-orbitals in the core region. In the split state, there is a similar reconfiguration of d-orbitals in the core region. However this is accompanied by an expansion of the primitive unit cell to one that contains two iron atoms. In common between to all the calculations is the reconfiguration of d-orbitals in the core region, although this reconfiguration incurs an energy penalty. From this I conclude that the EDFT convergence algorithm is being consistently misled towards this high energy configuration.

Hubbard previously observed that the localised interactions are determined mostly by Coulombic interactions, and the itinerant phenomena by electron exchange between the nuclei [164, 185]. Additionally I am able to distinguish phenomena with two distinct symmetries in Fe, changes in the d-orbitals localised around the nuclei that obey only inversion symmetry, and changes that affect the interstitial regions as well which satisfy a cubic symmetry. From this I conclude that the changes that satisfy the cubic symmetry are caused by itinerant phenomena, and that they can be separated from the localised changes. It might therefore be expected that there is a third

low-energy state in which the two iron sites are inequivalent like in the split state, but in which the localised d-orbitals are the same as in the symmetry-constrained state. Its energy would be the difference between the split and alternative states, about 0.3-0.8 meV.

noncollinear state The noncollinear state that was found had an energy of 5.1 meV. In this state the two iron sites are equivalent like in the alternative state, however the sites are equivalent only under an inversion about $[\frac{1}{4},\frac{1}{4},\frac{1}{4}]$, the primitive unit cell contains two iron atoms. The noncollinear state has a higher spin moment per iron atom of 2.26 μ_{B}, as such I call this state the increased spin state. For the increased spin state the energetic, and spin and charge density differences with respect to the symmetry constrainted state are similar to the same differences calculated for the split and alternative states, therefore previous convergence tests apply to this state.

This state was only found in the noncollinear calculations, which implies that the noncollinear moments are important for the properties of this state. A graph of the energy scatter against the residual noncollinear magnetic moment magnitudes is shown in fig. 5.13. It shows that there is no relationship between the energy of a state and the magnitude of the residual magnetic moment. Typical regions of noncollinear residuals are shown in fig. 5.14. These show that much of the noncollinear spin is located in the core regions. Noncollinear spins display a preference for antiferromagnetic configurations. These are the longest-range perturbations permitted in the unit cell used, and since the lowest energy magnetic excitations occur in iron occur over long ranges [186], one would expect to find such deviations at low energies. One other region where nonzero magnitudes of noncollinear spins are found is on the zero-density spin isosurface which is shown in fig. 5.2 b). However the extremely low magnitudes and the lack of correlation between their direction implies that noncollinear spin density residuals are energetically and functionally negligible by comparison to other effects, and that their presence is merely a result

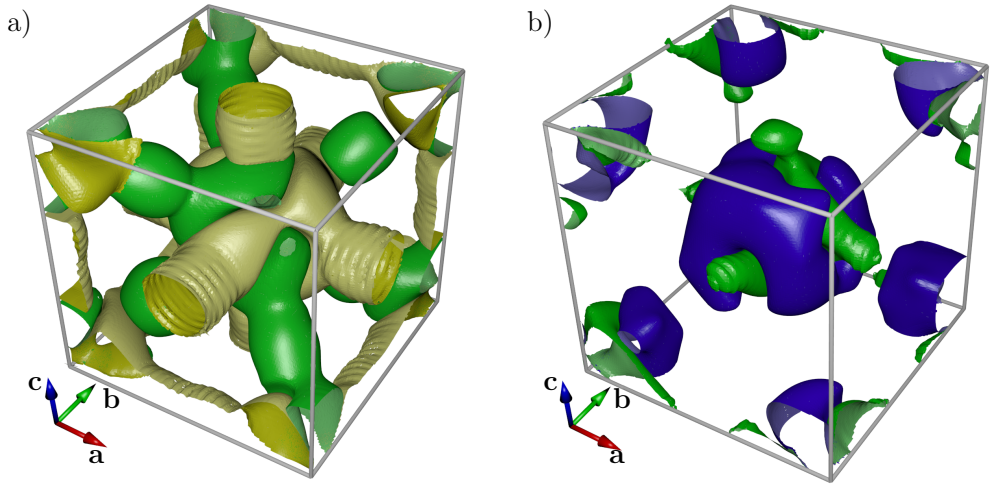

Figure 5.12: Differences between the increased spin and symmetry constrained states in PBE, computed as a change from the transition from the increased spin to the symmetry constrained state. a) Selected regions of density change, yellow surfaces enclose regions of increase, green surfaces enclose regions of decrease, charge density increases more or decreases less on the darker side of the isosurface. Ribbing caused by interpolation. b) Selected regions of density change, blue represents regions of increase, green represents regions of decrease (Fe atoms have positive spin). Portions of surfaces in the octant of the unit cell closest to the viewer have been removed for clarity. In both images portions of surfaces in the octant of the unit cell closest to the viewer have been removed for clarity.

of the negligible penalty for localised noncollinear spin polarisation in these regions.

The differences between the increased spin state and the symmetry constrained state must therefore be caused by differences in the spin charge density. The change in the charge density on the transition from the symmetry constrained to the increased spin state are shown in fig. 5.12 a). As before I can separate the charge density changes into core and non-core changes. Near the nuclei the same d-orbital structure found in the split and alternative states is present. Outside the core there is more electron density on the next-nearest-neighbour bonds than in the symmetry constrained state, and less electron density on the nearest-neighbour bonds. Transition from the symmetry constrained state to the increased spin state, while also strengthening the magnitude of the spin moment, reduces the electron density on these nearest-

neighbour bonds. This behaviour contrasts with the expected behaviour, as the transition from the nonmagnetic to the magnetic state, shown in fig. 5.2, involves an increase of the charge density on the nearest-neighbour bonds, yet the increased spin state has a higher spin polarisation. It is this behaviour that distinguishes the increased spin state from the split state, for while the atoms have the same magnetic moment as the high-spin atom in the split state, it is the next nearest neighbour bonds between low spin atoms that have an increased electron density in the split state. Due to these differences, as well as the higher energy of the increased spin state, it is at least partly independent from the split and alternative states.

The spin density changes on a transition from the symmetry constrained state to the high-spin state is shown in fig. 5.12 b). This gives insight into how the density changes lead to a higher overall spin. The d-orbitals coordinated along the second nearest neighbour bonds have a reduced spin moment magnitude. This means all the increase in the spin density is localised on those orbitals oriented in the direction of the nearest-neighbour bonds. In the core regions around the iron atom, the spin density changes have the same three-lobed regions of increased electron density around the nucleus, but unlike the split and alternative states these density changes are contiguous to the non-core regions. It is possible therefore that this state has been isolated in the calculation by a rapid convergence in the density of the core regions to a low energy state, which is then followed later in the calculation by convergences in the non-core regions.

All three new iron states are of very slightly higher energy than the symmetry-constrained ground state, between 1 and 5meV, and display a scatter as many self-consistent states of similar energy were found. These energies follow a trend: the more degrees of freedom that are permitted, the higher the energy. The obvious conclusion to draw here is that the EDFT algorithm used is unable to fully explore the energy space of the different electronic configurations. The larger the number of degrees of freedom that are permitted, the less effective the EDFT algorithm is. However the different energy states follow specific patterns. These small deviations

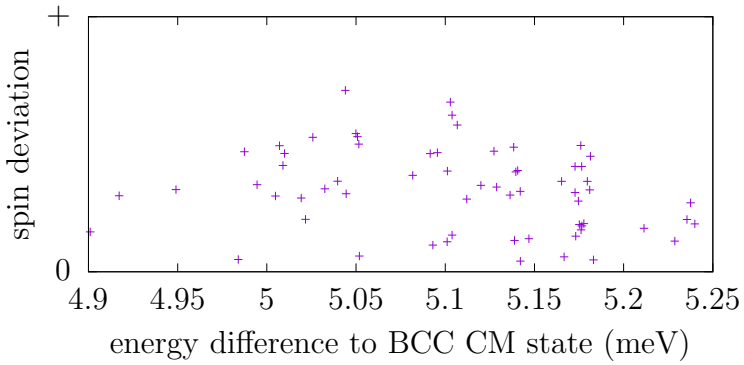

Figure 5.13: scatter plot of the residual noncollinear moment magnitudes against the energy in the different calculations under which NCM* under EFDT and PBE converged, energy differences are calculated to within 10 neV.

from the symmetry of the lowest-energy configuration can be divided into deviations near the nucleus, and deviations that affect the whole of the unit cell. These two types of deviation match with Hubbard's results [164, 185]. He found that the energies of localised and itinerant deviations were comparable, though the energy changes from localised deviations were mostly caused by Coulombic forces, and the energy changes from itinerant deviation were mostly caused by internuclear exchange processes.

5.3 Discussion of iron

The motivations of this work were to test the spin-setting procedure, and to examine the effect a relaxation of symmetry constraints has. The spin setting procedure was effective in iron calculations performed here: in conjunction with the EDFT method it was able to align the spins rapidly onto the desired direction in only 3 self-consistent field iteration loops. As the calculation results in table 5.1 show, it did not affect the ability of the algorithm to converge onto low-energy states. Further, as the calculation proceeds, if the initial directions specified are correct and the calculation converges onto a self-consistent state, the perturbation induced by the spin alignment procedure tends to zero. This means that it also provides a straightforward way to test if the spin orientation specified is in fact a ground state. In cases of a poor choice

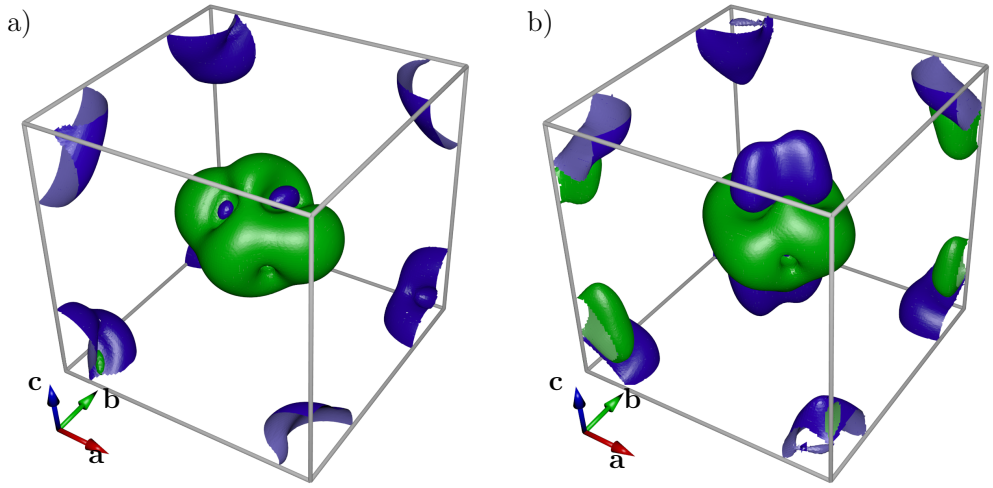

Figure 5.14: Selected regions of residual noncollinear magnetic moments. Blue and green regions have opposing moments. Portions of surfaces in the octant of the unit cell closest to the viewer have been removed for clarity.. In both images portions of surfaces in the octant of the unit cell closest to the viewer have been removed for clarity.

of spin orientation, the spin alignment procedure will continue to have a discernable effect as the calculation proceeds to its conclusion. This means that it can be applied to test the stability of chosen spin configurations, and determine if they instead need to be canted like in the noncollinear U_3X_4 (X=P,As) compounds [56]. This is an advantage over fixed spin or initialisation methods that enforce particular symmetries, when they initialise a spin configuration.

However the relaxation of the symmetry condition revealed that noncollinear calculations suffer from a problem: the failure of a convergence algorithm to find low energy states. The existing EDFT and DM convergence algorithms have been developed to function in collinear and symmetric calculations. Their straightforward application to a collinear symmetry-unconstrained calculation revealed that for metallic Fe, while the DM algorithm was able to occasionally find the ground state after a large number of iterations, EDFT converged fairly rapidly onto metastable higher energy states (1-2 meV). As the symmetry was relaxed further so spins were allowed to become noncollinear, these problems intensified and the DM algorithm was unable to converge onto any states in 60 iterations, and the EDFT algorithm converged

onto an even higher energy state (5 meV).

This sort of failure in the convergence is typical for itinerant systems. In such systems the DM algorithm suffers from "charge sloshing" as the charge moves relatively fluidly between each of the different low energy states. It is for this reason that EDFT is preferable to DM in itinerant systems. However while the EDFT algorithm is extremely effective at converging onto specific states, in so doing it risks converging onto the wrong state. An important observation however, was that the energetic deviation from the lowest energy state increased, as a larger number of degrees of freedom were permitted. According to DFT, as detailed in chapter 2, the energy gradient $\frac{\mathrm{d}E}{\mathrm{d}\rho(\mathbf{r})} = 0$ for any position $\mathbf{r}$ in the unit cell. Increasing the number of degrees of freedom therefore needlessly increases the complexity of the solution space by permitting energetically and configurationally equivalent deviations from the correct ground state. When one observes that the self-consistent deviations from the correct ground state were linked to the electronic structure in iron, one must expect that in an asymmetric system, the physical processes that lead to the asymmetry will distort the energy gradient $\frac{\mathrm{d}E}{\mathrm{d}\rho(\mathbf{r})}$, lift the degeneracy, and remove the problem.

However this line of reasoning does not extend to frustrated systems. In these systems there are processes that cannot be mutually satisfied. In such cases there are often many states of similar energy. While EDFT is effective at finding a self consistent state, the calculations on iron suggest that for a sufficiently frustrated system, in which there must be many degrees of freedom corresponding to the different mutually unsatisfiable physical processes, the correct ground state may be very difficult to find. I will therefore examine these deviations from the ground state.

There are two distinct sources of difficulty in the search for the ground state. Throughout the calcuations I find a small scatter as the EDFT algorithm converges onto a variety of different states. These scattered states are tightly localised around different metastable configurations. The scatter causes problems as it can lead to the mis-identification of states: if a scattered state is found which is very different in energy from the intended state, this can cause an incorrect assessment of the prop-

erties of the configuration. The second and larger problem is the convergence onto the metastable configurations, as these prevent the algorithm's convergence onto the ground state that one desires, and are unlikely to be solved by some incremental improvement to the EDFT algorithm.

How might these problems be overcome? The scatter can only successfuly be dealt with through the improvement of the algorithm's convergence behaviour, as difference in energy between the scattered states is too small. However the convergence onto the metastable configurations ought to be tackled using a different procedure, as from a noncollinear perspective one will often be interested in the energies and properties of these configurations. This would imply that one either uses a different convergence algorithm to search for the ground state, or that one constructs a series of different initialisations, each tailored to converge onto the desired state.

However a tailored initialisation of the calculation requires advance knowledge about the sorts of states that are required. This means that this approach will necessarily require advance knowledge of the system in question. As DFT has proven itself to be useful as a method to accompany and drive, rather than simply verify research. While an exhaustive search of different states may be performed, it would be a time consuming task that may be computationally unfeasible or impossible, so while a restricted search over the permitted configurations may be performed, it will not guarantee that the lowest energy state is actually found.

This behaviour of these itinerant electrons therefore also highlights the success of the symmetry-fixing method for determining specific noncollinear spin configurations [170, 171]. In iron, if the symmetry of the system is restricted to the correct bcc configuration, this improves the speed of convergence onto the correct low-energy state and the size of the calculation (see chapter 2.2). What I interpret from this, is that even if the correct symmetry of the system is not known, due to the relative ease of performing a high symmetry calculation, structure searches will be much easier to interpret and compare if the high-symmetry state is used as a reference, even if it does not have the lowest energy.

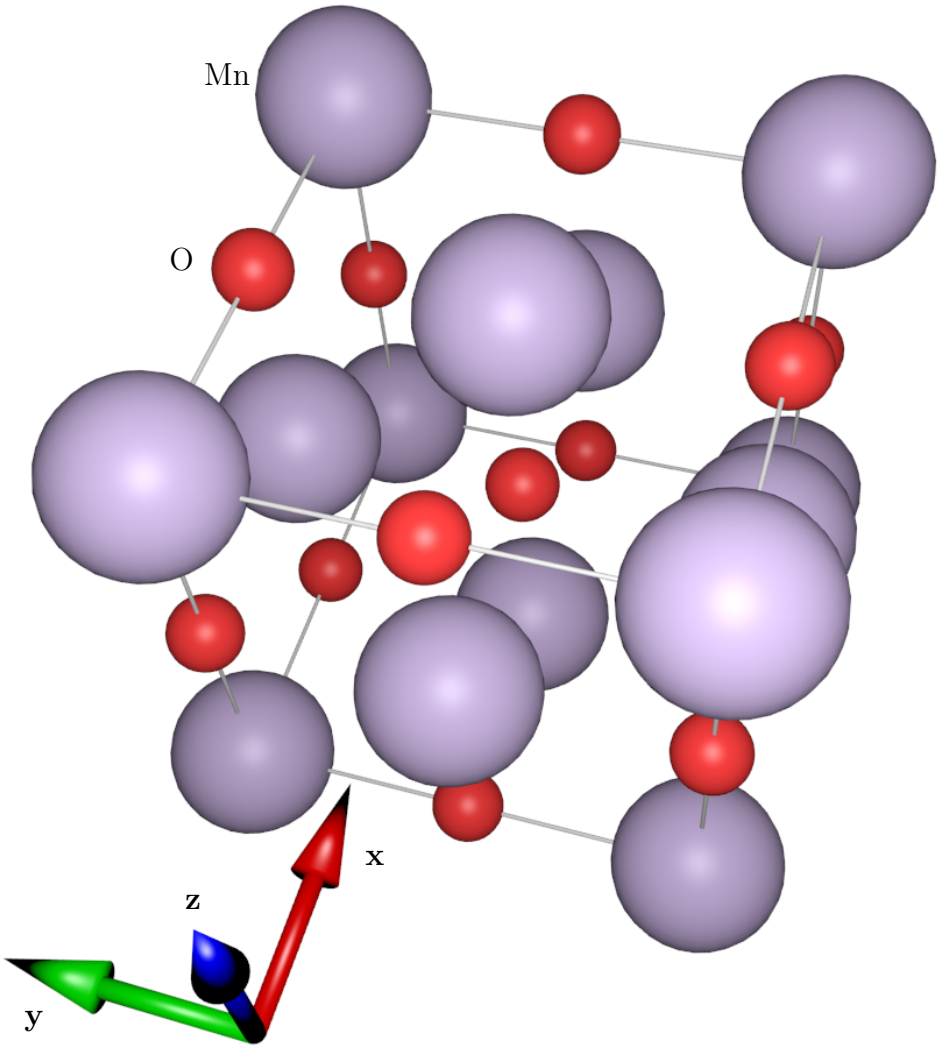

Figure 5.15: Crystal structure of MnO, showing the FCC arrangement of alternating planes of oxygen and Mn atoms.

This analysis indicates that the largest hurdle to low-symmetry calculations is the multiplicity of states available, and the tendency for algorithms to converge onto metastable states. The spin-setting procedure developed can be effective at orienting the spin moment along the desired direction, and additionally does not bias or otherwise affect the convergence algorithm.

5.4 Method example: manganese oxide

The spin setting procedure was found to be able to effectively initialise specific magnetic configurations in iron, in which the reorganisation of the Fermi surface

drives magnetic order. However magnetic phenomena caused by spin polarization are also found in insulators. Among these insulators there is a large class of system which can be analysed using the Ising model, in which most of the spin polarisation is localised in the electron density around individual nuclei, and in which the spin moment magnitude of this polarisation is fixed for each nucleus. This occurs because the electrostatic interaction of electrons on incompletely filled atomic orbital shells is strongly repulsive while the nuclear potential is strongly attractive, and the overall energy is minimised when the electron orbitals are made to be antisymmetric under exchange. This means a spin-polarized atomic configuration, in which the electrons have parallel spins and the wavefunction is antisymmetric, has a lower overall energy [187, Ch. 11]. These on-atom exchange and correlation interactions are typically quite large, and so the magnetisation on individual atoms can persist well beyond room temperature and is resilient to perturbation by inter-atomic interactions that affect spin polarisation. As a result magnetic order in these materials arises from interactions between on-atom spins, instead of from correlations between itinerant quasiparticles as in iron.

As in the case of iron I will test the use of the spin-setting procedure and the relaxation of symmetry constraints on manganese oxide (MnO), which is an example of an Ising-like system. MnO crystallises in the fcc rock-salt type structure at room temperature [188], this structure is shown in fig. 5.15. The manganese atoms host a net spin moment magnitude of about 4.6 μ_B [189, 190]. This value is close to the value of 5 μ_B expected for a half-full d-electron shell. According to Hund's rules this half-filled shell is stable to perturbation, and MnO is also an insulator with a band gap of nearly 4 eV [191]. These properties have allowed theorists to successfully use Ising-like spins in which the spin moment magnitude on each atom is fixed [192, 169], in contrast to itinerant magnetic systems like iron. Additionally these properties led Anderson to consider it as an ideal example of superexchange.

As MnO is an insulating Ising-like system the electrons around the atoms are localised, and so there is only a small overlap between adjacent atomic orbitals. Anderson [169]

found that this small overlap between adjacent orbitals determines the magnetic order. The important interactions between these orbitals are the same exchange processes that cause the localised Ising-like spins, except that the electron orbitals relevant to the magnetic behaviour are on separate atoms rather than the same one. Anderson identified two distinct types of interaction in spin polarised systems. The largest is direct exchange between adjacent magnetic ions, which usually dominates when it is present and like for on-atom orbitals results in a ferromagnetic spin configuration. The second is superexchange, which is so named because the relevant orbital overlap between magnetic ions occurs on top of a third atom with no net spin. Superexchange results in an antiferromagnetic configuration since it is energetically unfavourable for a net spin to exist on the neutral atom. It is only decisive in cases where direct exchange is negligible, as in the case of a half-filled d-shell like MnO.

As MnO is cooled below $T_{\mathrm{N}} = 118$ K, the magnetic moments order into an antiferromagnetic configuration, in which the spin moment direction alternates in planes perpendicular to the [1,1,1] direction. This magnetic order is accompanied by a structural change that occurs at the same temperature, in which the crystal contracts slightly in the same [1,1,1] direction, which results in an overall $R\bar{3}m$ symmetry [188, 193]. This structure is further complicated by interactions between the lattice and the spin structure, that result in an overall local monoclinic symmetry[194, 192], from which the rhombohedral $R\bar{3}m$ is recovered over approximately 0.1 μm.

As both the rhombohedral and monoclinic deviations from the cubic symmetry are small, they can usually be ignored in computational and theoretical works on the mechanism behind drives magnetic order [169, 195, 196]. When these additional effects are discounted, the magnetic unit cell is relatively simple and comprises only 4 atoms, and this simplicity has led it to be used as a test case for a range of different methods [169, 192].

5.4.1 Computational background

In computational studies MnO can be treated as part of a broader group of antiferromagnetic transition metal oxides, which includes FeO, CoO, and NiO. This is because all these materials are insulators with magnetic order determined by exchange processes. Further, their properties are strongly dependent on the d-orbitals on the metal ion, which are difficult to model in DFT. Early DFT calculations on the transition metal oxides by Mattheis [197, 198] that used Hartree-Fock provided important information about the structure of the d-orbitals, namely that the excitation of an electron to the unoccupied d-orbitals was energetically very costly (around 5 eV) in accordance with Hund's rules. This suggested that magnetic order will not cause large changes in d-orbital occupation, and the magnetic moment on the transition metal ion. However Mattheis' work was unable to determine whether a band theory approach that contained delocalised electrons, was the appropriate means to study the magnetic order.

However a short communication by Anderson which detailed the success of a band structure approach in the modelling of core orbitals, inspired calculations in the early 1980's based on the LDA [196]. These constituted a substantial improvement, as they were able to model the antiferromagnetic order and provided evidence for the superexchange processes, in addition to confirming the high energy of bands that contained unoccupied d-orbitals. However these calculations had a single notable failing, namely the prediction that MnO is a conductor with a Fermi surface, except when in the antiferromagnetic configuration. This conflicts with experimental observations that MnO is an insulator even when there is no magnetic order.

The inability of the LDA to effectively model the d-electrons came to be a particular problem with the discovery of the cuprate superconductors [199], which necessitated the development of new methods to account for these d-electrons. Particular success was obtained for the transition metal oxides with the parameter based LDA+U method [200]. However while in MnO a good choice of the relevant parameters is

able to predict a band gap of 3.8 eV, compared to the experimentally measured band gap of 4 eV [191], this is accompanied by a much worse prediction of the magnetic moment at 1.7 μ_B [201]. The field has therefore continued to develop, and contemporary work uses perturbative corrections on a DFT basis to obtain the correct band gap [195], though these methods are beyond the scope of a study which focuses only on methods in DFT.

Due to the wealth of comparable calculations on MnO, and its properties as an insulating magnetic system driven by exchange processes, I have chosen it as the second example for the use of the spin-setting method. This will allow a comparison between magnetic order driven by either itinerant or localised physical processes.

5.4.2 Convergences

To account for exchange and correlation, I will use PBE's exchange and correlation functional, which gives a marginally higher band gap of 0.9 over 0.8 eV for the LDA. While these values are small by comparison to experiment [191], the presence of a band gap for both functionals indicates DFT does at least succesfully obtain the conductive properties. Convergence calculations were performed on MnO. The convergence of the cutoff energy of the plane waves, shown in fig. 5.16 a), was performed comparing the energies of zero-spin calculations, and the ground AFM state. Using the method chapter 2.4, it was found that this energy difference was converged to one part in 10,000 at 1300 eV. This corresponded to a convergence in the relative energy of below 1 meV. For the convergence with respect to k-points it was found that the zero-spin calculations converged much more slowly than the AFM state, since it does not have a band gap. Therefore for the convergence calculations I used the total energy of the AFM state. Energy differences between states must converge at least as fast as this quantity. The convergences, shown in fig. 5.16 b), show that at 512 k-points, the energy is converged to below 1 meV.

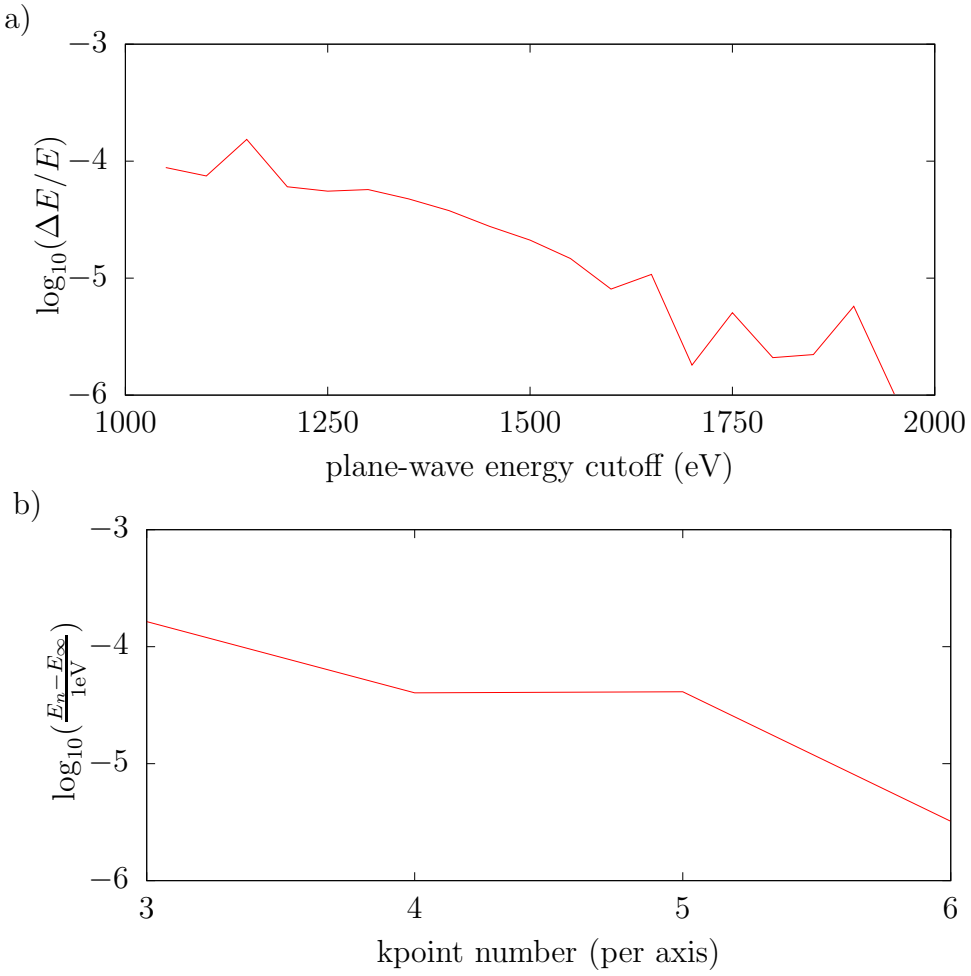

Figure 5.16: Convergence graphs a) the convergence of the energy difference between spin-zero calculations and the ground state b)Convergence of the energy of the ground state with respect to the number of kpoints, n. Here E_∞ taken as E_{1331}.

	DM	EDFT
NCM*+A	occasional convergence	two states
NCM*	occasional convergence, FM state	FM state
CM*	converges slowly	converges
CM	converges	converges

Table 5.2: A table of the calculations performed on MnO, star indicates that no symmetry constraints have been applied. The "+A" calculation used the spin alignment procedure.

5.4.3 Results

Noncollinear spin alignment results To start, it is useful to examine the electronic structure of MnO, calculated under collinear and symmetry constraints. The most important quantity for the determination of magnetic order is the spin density shown in fig. 5.17. The figure shows 4 isosurfaces of the spin density, the green and red spheres surround the manganese nuclei and are regions of high up, or down spin. The purple and blue surfaces are regions of lower spin density. The calculation shows that as expected from Hund's rules, the manganese atoms have a large spin that points in a uniform direction. In the theory of superexchange, the interactions which drive the antiferromagnetic order are localised on the oxygen atom. However while the oxygen atom has no overall spin moment, there is spin density around the oxygen atoms. It can be seen that the spin polarised orbitals that extend from the manganese atoms onto the oxygen, on which there is are complex structures in spin density.

From the spin density in fig. 5.17, one can observe that the important orbitals to consider on the oxygen are the p-orbitals, as the lobes of spin density close to the nucleus come in pairs. What is most striking is that the spin density around the oxygen oscillates: near to the oxygen nucleus the net spin density is aligned with the nearest manganese plane, but in between the oxygen nucleus and the manganese plane, the net spin density reverses and is instead anti-aligned with the Mn plane. Anderson in his theory of superexchange inferred that the antiferromagnetic configuration is preferred since it reduces the kinetic energy of the spin up and down

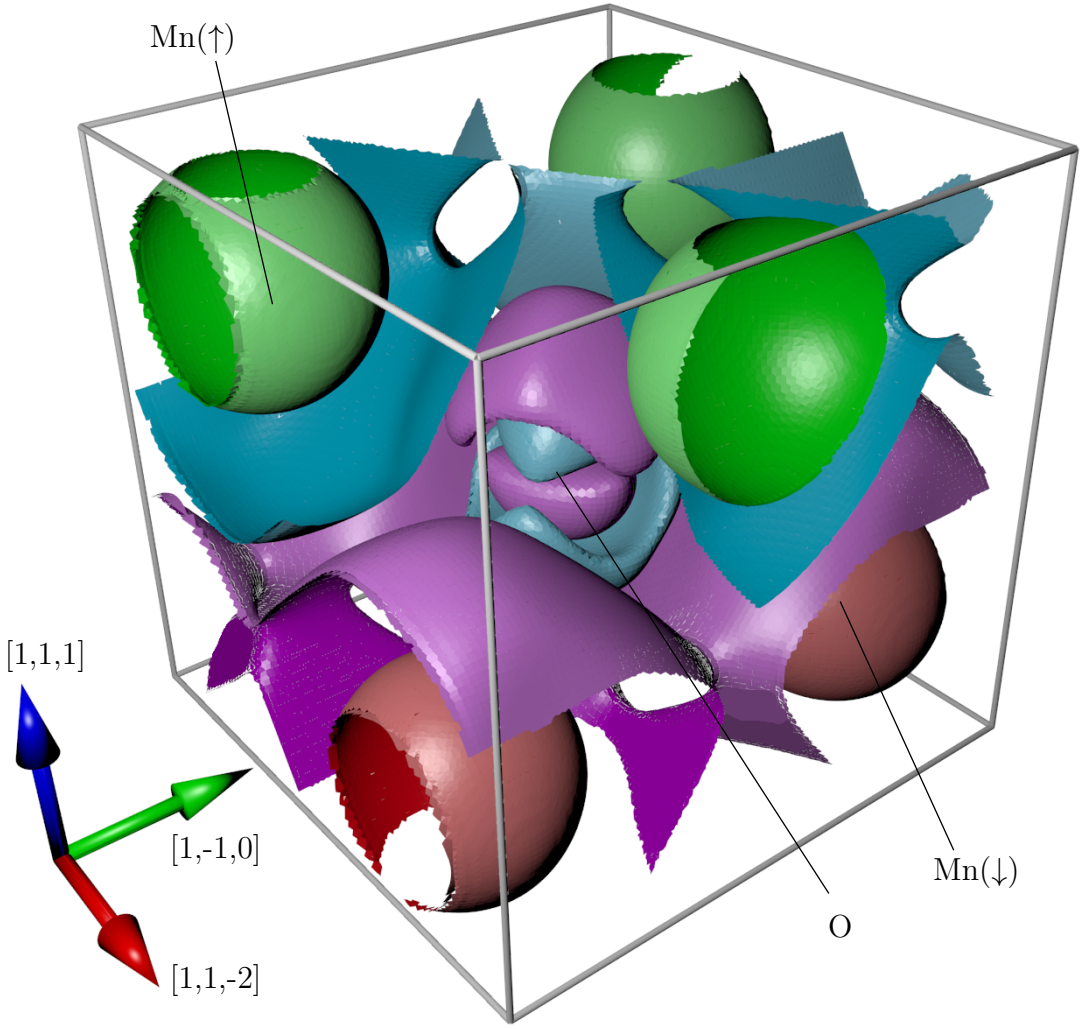

Figure 5.17: Isosurfaces of the spin density in Mn, around the Mn atoms at the centre of red and green isosurfaces and the oxygen atom in the centre of the image. Green/red isosurfaces are for high spin up/down densities, and blue/purple are for low spin up/down densities. Spin polarisation is always larger on the darker side of the isosurface.

orbitals, by allowing them to extend onto and share low energy orbitals on the oxygen atom [169]. However a spin-up orbital cannot extend onto a net spin-down Mn atom, so must be be curtailed before this point. It may be that the orbital that is most effectively curtailed actually extends further away from the oxygen nucleus, since there is a significant spin-up polarisation in between the oxygen atom and the spin-down maganese atom. However regardless of the mechanism, the oxygen orbitals which drive the exchange process have an occupation cannot be explained by a simply in terms of atomic oxygen orbitals, since these have reflection symmetry and there is a clear anisotropy in the spin density.

A range of different types of calculations were performed on MnO in order to test how the spin-setting procedure affected the final result. The results of the calculations are shown in table 5.2. For each of these types, at least ten calculations were performed. They show that collinear calculations converged, even when the symmetry conditions were relaxed and DM was used. Instead the relaxation of the collinear restriction was more significant. For the DM calculations, the algorithm was successfully able to converge onto an antiferromagnetic state. However this state was higher in energy than the true ground state of the system by 20 meV. The use of the spin alignment procedure with DM calculations did not change this result. For EDFT calculations, an unconstrained NCM calculation regularly converged onto a ferromagnetic arrangement, and was unable to find to the AFM ground state. The use of the spin alignment procedure partially solved the problem, as when it was used, the system found the AFM state in roughly half of the performed calculations, when the system was randomly initialised.

It was found that when symmetry constraints were relaxed the DM algorithm was still able to find the low energy states of the system. However it was unreliable. While the EDFT found a self-consistent state in every calculation, the DM calculation did not. It appears that the convergence of the DM algorithm is sensitive to the initial randomised wavefunction of the system, and the size of the parameter space that must minimised. Where EDFT uses the gradient of the Hamiltonian to find a low

energy state, DM uses an approach that weights different density configurations according to an estimate of their energy. While this can be very efficient, in cases where the energy landscape is quite complex with many similar configurations, as the density configurations are not self-consistent the estimate of the energy is not precise enough to allow the algorithm to converge.

Starting from a randomly initialised state is not unbiased towards antiferromagnetic or ferromagnetic order. To explain this one can recall that the largest energy contributions that concern the magnetism arise from satisfying the high-spin state on the Mn atom. This is because the energy difference between the FM/AFM configurations is about 0.31 eV, but the energy difference between a zero-spin constrained state and a spin state is much larger, at around 4.5 eV. As discussed by Anderson [169], indirect antiferromagnetic exchange processes are much smaller than ferromagnetic direct exchange processes, except in the special case of the half-full d shell when direct exchange is not permitted. What this means is that early in a calculation, when the spin and charge densities are not in the lowest-energy half-full d configuration, the spin states on adjacent Mn ion will tend to align. Once the spins on the manganese have aligned, the remainder of the calculation will be biased towards a ferromagnetic configuration.

When the spin-setting procedure is used, the situation is improved as around half of the calculations find the antiferromagnetic ground state. What this indicates is that for the process that biases the ferromagnetic order, the electrostatic and kinetic energy contributions are roughly the same as the spin-polarised part of the local exchange and correlation energy contributions. As only the self-consistent half-full d configuration has a physical analogue, this fact is not very interesting in itself. However what it does indicate is that the spin-setting procedure is not appropriate for this class of system. The inadequacy is caused by two phenomena: that the local x-c correlation energy associated with the spin polarisation is less that the kinetic and electrostatic energy that maintains the particular stability of a particular configuration, and in which there are processes early in a calculation that bias the

results towards a particular configuration that are larger than or comparable to the x-c correlation energies for that part of the calculation.

In MnO the resilience of the spin configuration, when subjected to even an inversion of the spin-polarised part of the x-c functional, indicates the resilience of the configuration to perturbation. For these reasons the problems associated with other spin initialisation methods detailed in chapter 5.1, specifically that they will bias the calculation to converge onto a specific incorrect electronic state, are no longer important. This is because the resultant possible states are so resilient to perturbation that even a relatively poorly chosen initialisation will still give a good result, at least after the perturbation is removed. Therefore while the spin-setting procedure is better than nothing, it is not likely to be the best choice for the initialisation of Ising-like systems with ordered magnetic structures resistant to perturbation.

5.4.4 Future work and preliminary study of $YMnO_3$

MnO is an insulator with a large band gap and a stable magnetic configuration that is resistant to perturbation of the order of eV in the spatial potential[2]. However persistence of the insulating behaviour of MnO into the high temperature disordered phase indicates that an insulating band structure may not necessarily lead to a resilient ground state spin configuration. This kind of behaviour is to be expected in frustrated systems, in which there are competing magnetic interactions that cannot all be satisfied. An example of such a material is $YMnO_3$, which is composed of manganese atoms arranged on the corners of a triangle. The magnetic interactions between these atoms are mediated in the same way as in MnO, via a superexchange process over nearby oxygen atoms.

Neutron studies on $YMnO_3$ have revealed that the lowest energy state is the same as that for a classical system with an Ising Hamiltonian, that is the spins are all angled by 120^o with respect to each other [202]. Recently performed DFT calculations

[2]excluding the structural distortions from cubic symmetry present in the ordered magnetic phase

suggest that density functional theory is able to replicate this triangular arrangment, however there are a large range of different configurations, and the study only explicitly included all the symmetry states that were compatible with the neutron results [203], so it is possible that DFT is in fact unable to replicate the correct results. Of additional concern is that the states in $YMnO_3$ may like MnO have the wrong electronic properties, for example they may be conductive when the material is reality an insulator [195].

However preliminary calculations on $YMnO_3$ that do not constrain the symmetry find that the state space is too large to permit a consistent minimisation. Foremost among them appears to be that the spin on the manganese is not accurately reproduced; while a spin is present it does not point in a uniform direction. Due to the nature of the spin setting procedure, it does not reorient moments on the Mn atom, so that they all point in the same direction. Due to the nature of the system, density mixing is not effective. Therefore this inconsistency is possibly a failure of the EDFT minimisation algorithm, as is converges onto a metastable configuration that very dissimilar to the true ground state.

The potentially most fruitful, but possibly most complex task, would be to develop an improved convergence algorithm that is able to take account of at least the many small metastable states like those found in iron. The principle challenge is that EDFT is extremely effective at finding a nearby self-consistent state, even when a user is not in fact interested in a *nearby* state, but instead in the lowest energy state. Noncollinear systems are especially prone to falling into a particular local well, since the range of available configurations is so large, and a rigorous search of them all is difficult. For example the DFT calculations on $YMnO_3$ indicate that the moment is canted slightly out of the plane [203]. However there this implies that there are nearby states in which not all the moments are all canted in the same direction, which likely have a similar energy. The development of an algorithm that can consistently find the low energy state regardless of these traps or pitfalls is therefore highly desirable.

5.5 Conclusions

This work has examined the efficacy of the spin setting procedure in initialisation of the magnetic structures of iron and MnO, and the relaxation of symmetry constraints. It was found that its effectiveness was dependent on the physical properties of the system in question. In iron the spin-setting procedure could be used to calculate a ferromagnetic configuration, and aligned the spin in the desired direction effectively after roughly the correct charge density had been found.

However relaxation of symmetry constraints led to difficulties in the search for the correct ground state in iron. It was found that when the PBE x-c functional was used the DM algorithm was unable find the correct ground state, and when the EDFT algorithm was used the calculations were consistently misled towards a number of low symmetry self consistent states. These states were up to 5 meV in energy above the ground state. In the case of the iron unit cell used, there are 96 different symmetry operations. This results in a large space of degenerate configurations when the symmetry constraints are relaxed, and it is likely that the degeneracy causes the difficulty in the convergence to the correct state. As a result in many asymmetric noncollinear systems a low symmetry state is unlikely to cause the same problems.

Such reasoning will not apply to certain frustrated systems. This is because in iron, the properties of the asymmetric states could be explained by reference to two distinct physical phenomena present in the system. As a result in a multiply frustrated system, it may be possible that there are many states of similar energy, which results in an even larger solution space, in which the lowest energy state is not symmetric like in iron. It is feasable that in such a system the DM algorithm may fail, and the EDFT algorithm might be consistently misled. This will make the study of such systems under DFT difficult. For these systems a new convergence algorithm may be needed.

In MnO I found that a random initialisation of the calculation does not lead to an unbiased search of the different spin configurations of the system. Instead based

on a consideration of exchange processes [169], it is likely that the preferred spin configuration of a high-energy charge density configuration is different to that of the correct ground state, which causes an inherent bias to a calculations. It was found that the spin setting procedure is not able to consistently push the calculation towards the correct ground state configuration, and this was both because the energy of the spin-polarised part of the exchange and correlation potential is comparable to other energies in the system, and because the different configurations are resilient to changes in, and of the order of, the x-c potential. One of the motivations behind using the spin setting procedure was to avoid the biasing the convergence onto a similar configuration, but which was not the correct ground state. However the spin states in MnO are resistant to changes in the x-c potential, in that the different available spin configurations are well-separated in energy and it is difficult to transition between them. This means that the use of one of the other spin initialistion methods is unlikely to bias the calculation to a particular incorrect configuration. It therefore seems the spin setting procedure is not the best choice of initialisation procedure for systems such as MnO.

Calculations on MnO performed here show how in DFT the mechanism of super-exchange causes the small pockets of the electron density around the oxygen atom to become spin polarised, as the orbitals on the manganese reduce their kinetic energy by extending onto the neighbouring oxygen orbitals. The small unit cell of manganese oxide makes it an appropriate material to test new calculation methods, and I have shown that the current widely used DM and EDFT algorithms are both able to function in symmetry unconstrained non-collinear systems. As MnO is an insulator, the band gap means that the ground state spin configuration of the system is more stable to with respect to changes in the combined effective potential $V_{\mathrm{H,n}} + V_{\mathrm{xc}}$, and this makes it possible for DM to find self consistent states, in contrast to the ferromagnetic iron example.

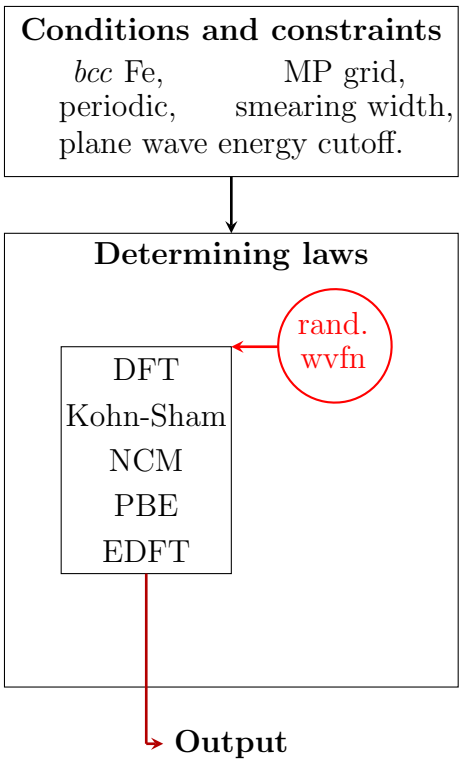

Figure 5.18: the explanatory set-up of the Fe NCM calculations performed here.

5.5.1 Implications for emergence

In the case of MnO, there was no evidence to suggest that a multiplicity of states existed. Instead only an antiferromagnetic and ferromagnetic configuration were found.

For the Fe calculations performed here, a diagrammatic representation of the explanatory set-up is shown in fig. 5.18. For the purposes of historical emergence, the important quality of this set-up is that in the calculation (or determining laws) the initial wavefunction was randomised, and this leads to a multiplicity of different results in the output of the calculation. While in the outputs groups could be identified that had similar magnetisations and energies, none of the different initializations resulted in an identical final state. Further, I was primarily interested in one specific state, the lowest energy state, but during the calculations it was not found.

One additional property was observed, and that was that when the same wavefunction was used in the initialisation of the calculation, the same resultant state was found.

This means that it must be possible to exactly determine how each of the different initialisations relate to final metastable states in the calculation. However it is seems likely that there is at least a very large number of qualitatively different deterministic descriptions, because as can be seen in fig. 5.13, there is very little structure in the energies of the outputs of the calculation. Additionally there are a large number of other states that exist, that have not even been found, such as the cases in which the symmetry is partially or fully constrained, as in the collinear calculations. As a result, for all practical purposes, this set-up must be treated as historically emergent.

This explanatory set-up also satisfies some of the predicted qualities of historical emergence: it is unpredictable, and a particular outcome is vanishingly unlikely to be repeated. As discussed in chapter 1 this makes the value of these calculations limited. To be precise, one can draw only two conclusions, first that the results group into specific sorts of structure, and second that the calculations are unable to give details of these structures past a specific degree of accuracy.

Future work

This set-up is undesirable because we are interested in the precise details of these broad structures into which the different results can be grouped. This provides a motivation to construct modifications to the model in order to remove the historical emergence. There are a number of ways one could make this can happen. The simplest way is to do away with the random wavefunction generator, and instead to include an initial wavefunction as one of the conditions or constraints. However as these calculations show, unless the choice of wavefunction is special in some way, there is no reason to think that the output of the calculation will have the desired qualities, such as the minimum energy condition. Another problem with this approach is that it may also end up biasing the result of the calculation, which will lead to incorrect conclusions about the behaviour of the system. Indeed this was the motivation for the relaxation of the symmetry in the first instance. For this reason this approach is unlikely to be satisfactory in the general case.

The most satisfactory way would be to improve the convergence algorithm, so that it instead consistently converges onto the desired low energy state. However EDFT is well-known to be extremely effective due to its strictly variational nature as detailed in chapter 2.2.4. Such an algorithm would likely need to be variational like EDFT, since it was shown that the DM algorithm was not able to find the state due to the complex state space. EDFT uses a line minimisation algorithm, and the most obvious way to improve this would be to probe other areas of the energy surface of the density functional. However such an algorithm would likely be even more expensive than EDFT, and so may perhaps not be worth the trouble. Alternatively a set of manually initialised calculations with specific symmetries may allow a more detailed search of the state space. However given that there are 96 different symmetry operations in iron, combinatorically the number of different possible symmetry initialisations is too numerous, and it would be preferable to have a method that gets us straight to the desired answer.

What seems likely is that these many different metastable configurations arises from complicated interactions present from small restructuring of the Fermi surface. As such a different Brillouin zone sampling method might lead the system towards a desired state. While the MP method is straightforward to visualise and implement, other schemes exist [204, 205]. Although it seems unlikely that the full range of different metastable configurations might be determinable from any of these methods, it may at least be the case that one of them can precisely determine different progenitor states for each of the broad groups in which the different states reside. This would at least permit a rigorous explanation of how these groups arise.

Conclusions

The analysis of the results of these calculations on iron in the terms of historical emergence show that this theory of emergence has practical use. It provides a natural framework to understand how complexity leads to difficulty in the interpretation of results, and in how an explanation can be provided. Additionally the framework of

historical emergence is able to accommodate descriptions for how a modification or perhaps extension of the set-up used can localise the emergent nature in a particular part of the system, and in so doing isolate the non-emergent parts of the system so as to provide an explanation for how they arise.

The calculations on manganese oxide used a very similar set-up to those on iron. However instead of a multiplicity of states only two were found, as in the calculation the randomness in the initial conditions was systematically reduced by the density search algorithms. Due to this I was able to interpret the results and suggest an explanation for the results that I observed when the spin setting procedure was used. It can therefore be seen that in this case an explanatory description was available, in line with our expectations about set-ups that are not historically emergent.

Chapter 6

Conclusions

6.1 Physical methods

Noncollinear magnetism and spin initialisation DFT can be used to study a wide range of physical systems. However there are some limitations around its implementation, as only approximations have been made for the general Hohenberg-Kohn functionals [81, 155, 82, 206], and the density search algorithms make certain assumptions about the nature of the functional's energy space (see chapter 2.2.4). Although DFT aims to calculate the properties of material in the ground state, in practice it is at least as capable at finding metastable states, even those with the same symmetry.

As a result it is important to have a spin initialisation method that does not inappropriately influence a calculation to converge onto an incorrect spin or charge density state. I developed a new spin initialisation method in chapter 5.2 which worked by modifying the spin-dependent potential generated by the x-c functional, creating a bias toward a particular atomic spin configuration. In this procedure the corrective terms are gauranteed to disappear as the spins align in the desired direction.

The spin setting procedure was effective in iron, but due to the accompanying relaxation of symmetry conditions, a multiplicity of different iron states were found.

I found that these different iron states displayed deviations from the ground state configuration localised in either atomic iron core states, or the interstitial regions. However there were too many of these states to give anything more than a broad characterisation of the behaviour.

If these metastable states in iron are to be studied further, there are some possible steps one might take to address this problem. One solution might be to develop a new density search algorithm. Another solution would be to perform manual initialisations with different symmetries. A third solution might be to use a different method to sample the k-point mesh. Given the large number of different metastable states it is likely that no complete account of the properties of all the states can be given. Although as I was able to identify broad classes of states, it might be possible to calculate progenitor states for each of these classes which exhibits the most salient or important properties shared among each of the broad classes.

It was hypothesised that the large number of different metastable states was facilitated by complex interactions at the Fermi surface. This hypothesis was supported by calculations on MnO, presented in chapter 5.2. MnO is an insulating antiferromagnet, and only two magnetic configurations were found even in symmetry unconstrained calculations. Indeed in MnO interactions between bands which cross the Fermi surface do not neet to be precisely accounted for, as there is no Fermi surface.

However while the spin setting procedure was successful in iron, in MnO it was only partially able to bias the calculation towards the desired configuration. This was because of two reasons, first because the energy scale of the x-c functional is smaller in MnO than the energies of the dominant processes that cause magnetic order. Second because the states in MnO are resistant to perturbation. This means while the spin initialisation procedure developed here has only a limited utility, in those systems where it does not function, less subtle methods can be used without fear of changing the properties of the resultant spin state.

This study of different spin initialisations ought to be extended to other materials. Materials that exhibit noncollinear order like $YMnO_3$ would be particularly interest-

ing to study, as their behaviour is thought to be that of a frustrated antiferromagnetic Manganese atoms arranged in a triangle [202]. While calculations have been performed on $YMnO_3$, these have mostly made use of symmetry constraints [203], and it would be worth investigating if the solution space for $YMnO_3$ was similar to that in iron or manganese oxide, and if the spin setting procedure used here is useful for frustrated systems.

Cyclobutadiene In the calculations on cyclobutadiene presented in chapter 3, the adiabatic separability of the electrons and nuclei allowed an unmodified version of DFT to be used to calculate a potential for the nuclei. It was found that the resulting potential was adequate for a description of the tunelling behaviour of the molecule. For further calculations, the principle challenge to an accurate calculation is the flexibility of the molecule. Most studies of phonon and Raman interactions in molecules seperate motions that break different symmetries, as this is permitted under the harmonic approximation. However in cyclobutadiene the mismatch between experimental and theoretical frequencies implies that this condition must be lifted, as the nuclear wavefunction probes anharmonic parts of the effective nuclear potential.

While the method I proposed could technically be used to perform these calculations, this would be very challenging to implement. The challenge arises because the position basis set that I used was not appropriate for the problem, and because the extension of the method to larger numbers of dimensions, to accommodate the flexing of the molecule in more directions will increase the burden of the calculation beyond reasonable levels. In an improved caluclation a refined basis set in which the states are similar to the eigenstates of the Hamiltonian could be used. The obvious choice of basis set in the case of cyclobutadiene would be orthogonalised energy eigenstates of the semiclassical harmonic model. The anharmonicity of the potential could be included as crossing terms between these different states in the Hamiltonian, and could be calculated using DFT in the same way as was done here.

A calculation set up in this way would have the benefit that it would be much easier to interpret the tunelling behaviour of the different excitations in terms of the semiclassical harmonic states. However it would be more complex to implement due to the requirement that the basis set be composed of orthogonal states.

Iron arsenide In iron arsenide calculations presented in chapter 4, although DFT was unable to reproduce the desired incommensurate behaviour, it was able to provide a justification for the observation of a new diffraction peak. This was aided by symmetry arguments and projections of the wavefunction that detailed suscesptibity of the bandstructure to perturbations localised around the iron atoms. It was suggested that, due to an observed preference for a right-handed chirality in the material, spin-orbit coupling might be the mechanism that drives this behaviour.

However it is not clear if the material displays a preference for right-handed chirality, if the material undergoes a symmetric symmetry breaking process between left- and right-handed chirality, and in the particular experiment that was performed a right-handed chirality was observed. To put it another way, let us construct a free energy equation [154] like

$$\mathcal{F} = b_1\mathcal{C} + a_2\mathcal{C}^2 + b_3\mathcal{C}^3 + a_4\mathcal{C}^4..., \tag{6.1.1}$$

where $\mathcal{C}$ is some magnetic order parameter dependent on the (+ve or −ve) chirality, $\mathcal{F}$ is the free energy, and a_i and b_i are temperature dependent coefficients. It is not clear if the coefficients b_i that would cause a preference for a particular chirality, presumably caused by spin-orbit interactions, are nonzero. This is because only one set of polarised xray diffraction experiments have been performed, and it may be the case that in the particular experiment that was performed a right-handed chirality was observed.

Further work on iron arsenide might therefore include repeating the polarised XRES experiments that were performed to verify that there is a preference for right-handed chirality. However more DFT calculations could also be performed. Previous non-collinear calculations initialised a helical spin-density wave in the material [207].

This could be extended to permit elliptical and canted configurations. As discussed elsewhere [207], these calculations could also be extended to include different structural configurations to determine if a modification of the lattice is critical in the mechanism for the magnetic order, or only coupled to it.

6.2 Historical emergence

Of the four example systems studied here – iron arsenide, cyclobutadiene, noncollinear magnetism in iron, and noncollinear magnetism in manganese oxide – only the noncollinear calculations in iron may deserve to be called historically emergent. These results are encouraging, for they suggest that historical emergence is neither too rare nor too common. Instead it functions as a definition that is able to identify important behaviour that commonly exists in physical systems.

The study of noncollinear magnetism in iron in chapter 5.2, revealed calculations that were for practical purposes historically emergent. A historically emergent set-up is predicted to exhibit unreapeatability in practice, and this was found in the calculations. In the historically emergent set-up the method was no longer able to reliably find the correct ground state properties of iron. As such I was unable to give an unified explanatory account for how each of the different configurations arose. In so doing this explanatory set-up behaved as an historically emergent system.

This behaviour in iron contrasts with other theories of emergence. In Batterman's singular limit emergence he generally calls phenomena that are robust and reliable emergent. By contrast, historical emergence appears to be extremely sensitive, as in the case of iron a small change in the initial conditions resulted in a different ground state. However certain patterns could be observed in the results of the calculation. A complete explanation could not be provided for all the calculation results and their behaviour, I was able to distinguish coarse classes of phenomena. For example I was able to conclude that there were two different mechanisms which originated in core and interstitial electons respectively. This constitutes a notable success of historical

emergence, as it is able to accommodate explanations for reductive patterns, which appear in an otherwise irreducible set of results.

Further work could be performed to investigate if historical emergence is typical to metallic systems in general in symmetry unconstrained calculations, or if iron is in some way unique. Collinear magnetic insulators with band gaps in excess of 0.5eV seem unlikely candidates for historical emergence of this type, based on complex reconfigurations at the Fermi surface. However it is not clear if frustrated noncollinear systems like $YMnO_3$ might have different properties, since calculations show that many different orientations are seperated only by tens of meV in energy [202, 203].

In iron arsenide I was not able to find any new evidence that might indicate that meaningful historical emergence was present. Instead it seems most likely that although there is a continuum in the permitted periodicity of the magnetic order, all these periodicities are related. This is because below T_N there are no further discontinuities in the material's properties with respect to a change in temperature. What this implies is that all the behaviour in the magnetic state can be related through an adiabatic continuation, and for a particular crystal no further information than the temperature is required.

However I restricted the study to iron arsenide's bulk behaviour. Based on experimental results disorder has an important role in the magnetic structure of iron arsenide. Additionally it has been shown that even similar single crystals can have slightly different properties. What this means is that while there is no indication that iron arsenide can host historical emergence, there is still ample scope for further research into the material's properties. The possibility of historical emergence's existence has not been ruled out in this material.

As presented in chapter 3, cyclobutadiene was not found to be historically emergent, but the analysis of the physical properties of the molecule elucidated the relationship between molecules and the physical equations that determine their behaviour. In quantum mechanics chemical isomers have the same governing equations. This implies that it might be possible to explain the different chemical behaviours in a

single explanation. However what the study of cyclobutadiene has shown is that it is still necessary to consider each of the isomers independently even in a quantum mechanical treatment. This is because although the general Schrödinger equation for the system implies that a series of symmetries are held in the material, each of the chemical functions of the isomers cannot be accounted for in a single generalised symmetry calculation. This means that each of the functional properties of the isomers must be described and explained seperately. This sort of multiplicity must therefore, at some level of molecular complexity, become historically emergent.

What this work reveals is that the account of historical emergence describes important details about the interaction between theory and physical systems. It is able to show how an emergent system is wholly dependent on a reductive description, even as it is able to detail how such a reductive description can never be provided. In this way it is able to inform the process of science, so that the explanatory set up can be modified and the unpredictability can be removed. It is additionally able to do this with a definition that can be unambiguously applied to a wide range of physical systems, in a discerning and concise manner.

Further work on historical emergence might also be performed. The philosophy of this work did not extend itself to two areas: the first was in the account of how an explanation can become scientifically satisfying; the second is how an explanatory set-up be emergent *in practice*. I was able to show how the iron example was historically emergent in practice, by reference to wider scientific work and the field of study. However it would be desirable to have a more rigorous set of principles by which an explanatory set-up might be defined to be practically emergent.

The philosophy in this work benefited from a close proximity to physics research. This approach has limitations, as some of the conclusions that were drawn had to concern the practice of science. This means that for some such a work is slightly counter to the goals of philosophy, which is to inform reality independently of practical limitiations [5, 7, 8, 11, 16, 18, 29, 33]. However it must be noted that if a useful philsophical theory is to be applied to science, and meaningfully inform

its process (a deeply practical activity), it must in some way be able to describe and accommodate practical limitations. In this way it is worthy of study in its own right [19, 17, 4].

Appendix A

Appendix

A.1 Isosurface point picker

The points at the Isosurface were chosen by picking paths through the reciprocal space Brillouin zone, and using a B-spline interpolation to find the crossing points on the paths. These paths where chosen to be the paths between nearest-neighbours in the MP grid used in the DFT calculation. Points that were too close to each other (closer than 0.3 of the smallest MP grid spacing) were assumed to be duplicate points, and were consolidated with the most recently generated points deleted. Two-dimensional Voronoi cells projected onto the plane normal to the Isosurface, of the remaining points were constructed. To improve the efficiency of this construction a rough Delauney mesh was constructed, in which vertices were allowed to cross in intermediate cases, and these mesh-connections were used as the basis for the Voronoi cell construction. The resultant points are the triangular faces of the Voronoi cell construction, and each face has a weight proportional to the area of the triangle.

A.2 Dependence of resistivity on temperature

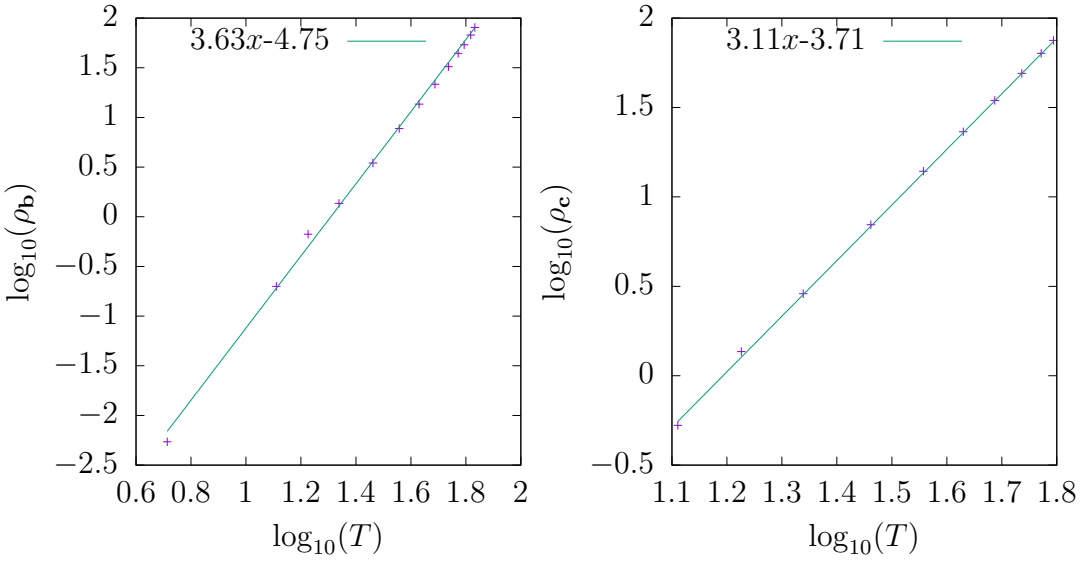

Figure A.1: Analysis of the low-temperature results of the resistivity of iron arsenide. Graphs show the power law relationship exhibited by a straight line on a log-log scale.

Bibliography

[1] P. W. Anderson, *More Is Different*, Science **177**, 393 (1972).

[2] M. Paoletti and F. Orilia, *Philosophical and Scientific Perspectives on Downward Causation* (Taylor & Francis, 2017).

[3] R. M. Dancy, *Plato's Introduction of Forms* (Cambridge University Press, 2004).

[4] R. Watson and M. Grene, *Malebranche's First and Last Critics: Simon Foucher and Dortous de Mairan* (Published for the Journal of the History of Philosophy, Incorporated, Southern Illinois University Press, 1995).

[5] N. S., *The Cambridge Companion to Malebranche* (Cambridge University Press, 2000).

[6] D. Davidson, *The Essential Davidson* (Clarendon Press, 2006).

[7] J. Butterfield, *Less is Different: Emergence and Reduction Reconciled*, Foundations of Physics **41**, 1065 (2011).

[8] S. Weinberg, *Dreams of a Final Theory* (Pantheon Books, 1992).

[9] R. Martin, *Electronic Structure: Basic Theory and Practical Methods* (Cambridge University Press, 2014).

[10] R. Martin, L. Reining, and D. Ceperley, *Interacting Electrons* (Cambridge University Press, 2016).

[11] C. Broad, *The Mind and its Place in Nature* (Routlegde & Kegan Paul, London, UK, 1925).

[12] J. J. Thomson, *Conduction of electricity through gases* (Cambridge University press, 1906).

[13] A. Fleming, *On the history and development of the thermionic valve*, Journal of Scientific Instruments **11**, 44 (1934).

[14] D. Chalmers, *The Conscious Mind: In Search of a Fundamental Theory* (Oxford University Press, 1996).

[15] D. Papineau, *Thinking about Consciousness* (Clarendon Press, 2002).

[16] G. Strawson, *Mental Reality* (MIT Press, 2009).

[17] N. Cartwright, *The dappled world : a study of the boundaries of science.* (Cambridge University Press, Cambridge, 1999), Sample chapter deposited. Chapter 3: 'Nomological machines and the laws they produce', pp. 49-74.

[18] E. Nagel, *The structure of science: problems in the logic of scientific explanation* (Harcourt, Brace & World, 1961).

[19] R. Batterman, *The Devil in the Details: Asymptotic Reasoning in Explanation, Reduction, and Emergence* (Oxford University Press, 2001).

[20] P. C. W. Davies, *Emergent biological principles and the computational properties of the universe: Explaining it or explaining it away*, Complexity **10**, 11 (2004).

[21] C. Ross, J. Bird, and A. Little, *Mechanics of Solids, 2nd ed* (Taylor & Francis, 2016).

[22] S. Lloyd, *Computational Capacity of the Universe*, Phys. Rev. Lett. **88**, 237901 (2002).

[23] N. Margolus and L. B. Levitin, *The maximum speed of dynamical evolution*, Physica D: Nonlinear Phenomena **120**, 188 (1998), Proceedings of the Fourth Workshop on Physics and Consumption.

[24] M. Pexton, *Emergence and Fundamentality in a Pancomputationalist Universe*, Minds and Machines **25**, 301 (2015).

[25] P. L. Luisi, *Emergence in Chemistry: Chemistry as the Embodiment of Emergence*, Foundations of Chemistry **4**, 183 (2002).

[26] P. E. Leopold, M. Montal, and J. N. Onuchic, *Protein folding funnels: a kinetic approach to the sequence-structure relationship.*, Proceedings of the National Academy of Sciences **89**, 8721 (1992).

[27] K. A. Dill and J. L. MacCallum, *The Protein-Folding Problem, 50 Years On*, Science **338**, 1042 (2012).

[28] V. S. Denchev *et al.*, *What is the Computational Value of Finite-Range Tunneling?*, Phys. Rev. X **6**, 031015 (2016).

[29] C. G. Hempel and P. Oppenheim, *Studies in the Logic of Explanation*, Philosophy of Science **15**, 135 (1948).

[30] W. Salmon, *Four Decades of Scientific Explanation* (University of Minnesota Press, 1989).

[31] N. Rescher, *Scientific Explanation* (New York: Free Press, 1970).

[32] B. Baumrin, *Philosophy of Science: The Delaware Seminar. Edited by Bernard Baumrin. V.2* (Interscience Publishers, 1963).

[33] C. Hempel, *Aspects of scientific explanation: and other essays in the philosophy of science* (Free Press, 1965).

[34] P. Kitcher and W. Salmon, *Scientific Explanation* (University of Minnesota Press, 1989).

[35] J. Nelson, *The Physics of Solar Cells* (Imperial College Press, 2003).

[36] N. Asim *et al.*, *A review on the role of materials science in solar cells*, Renewable and Sustainable Energy Reviews **16**, 5834 (2012).

[37] G. Jeanmairet, S. Sharma, and A. Alavi, *Stochastic multi-reference perturbation theory with application to the linearized coupled cluster method*, The Journal of Chemical Physics **146**, 044107 (2017).

[38] P. Hohenberg and W. Kohn, *Inhomogeneous Electron Gas*, Phys. Rev. **136**, B864 (1964).

[39] P. Čársky, R. J. Bartlett, G. Fitzgerald, J. Noga, and V. Špirko, *Ab initio calculations on the energy of activation and tunneling in the automerization of cyclobutadiene*, The Journal of Chemical Physics **89**, 3008 (1988).

[40] R. Lefebvre and N. Moiseyev, *Automerization of cyclobutadiene*, Journal of the American Chemical Society **112**, 5052 (1990).

[41] M. Eckert-Maksić, M. Vazdar, M. Barbatti, H. Lischka, and Z. B. Maksić, *Automerization reaction of cyclobutadiene and its barrier height: An ab initio benchmark multireference average-quadratic coupled cluster study*, The Journal of Chemical Physics **125**, 064310 (2006).

[42] T. Saito *et al.*, *A broken-symmetry study on the automerization of cyclobutadiene. Comparison with UNO- and DNO-MRCC methods*, Chemical Physics Letters **498**, 253 (2010).

[43] E. Wilson, J. Decius, and P. Cross, *Molecular Vibrations: The Theory of Infrared and Raman Vibrational Spectra* (Dover Publications, 1955).

[44] G. Herzberg, *Molecular spectra and molecular structure. Vol.2: Infrared and Raman spectra of polyatomic molecules* (D.Van Nostrand Company Inc., 1945).

[45] J. Bain, *Emergence and mechanism in the fractional quantum Hall effect*, Studies in History and Philosophy of Science Part B: Studies in History and Philosophy of Modern Physics **56**, 27 (2016).

[46] T. Lancaster and M. Pexton, *Reduction and emergence in the fractional quantum Hall state*, Studies in History and Philosophy of Science Part B: Studies in History and Philosophy of Modern Physics **52**, 343 (2015).

[47] T. Frawley *et al.*, *Elucidation of the helical spin structure of FeAs*, Phys. Rev. B **95**, 064424 (2017).

[48] D. Parker and I. I. Mazin, *Non-nesting spin-density-wave antiferromagnetism in FeAs from first principles*, Phys. Rev. B **83**, 180403 (2011).

[49] X. Ren, P. Rinke, C. Joas, and M. Scheffler, *Random-phase approximation and its applications in computational chemistry and materials science*, Journal of Materials Science **47**, 7447 (2012).

[50] A. W. Overhauser, *Spin Density Waves in an Electron Gas*, Phys. Rev. **128**, 1437 (1962).

[51] S.-H. Lee *et al.*, *Emergent excitations in a geometrically frustrated magnet*, Nature **418**, 856 (2002).

[52] F. Ma, C. Reichhardt, W. Gan, C. J. O. Reichhardt, and W. S. Lew, *Emergent geometric frustration of artificial magnetic skyrmion crystals*, Phys. Rev. B **94**, 144405 (2016).

[53] W. R. Branford, *Emergent magnetic monopoles in frustrated magnetic systems*, Philosophical transactions. Series A, Mathematical, physical, and engineering sciences **370**, 5702–5704 (2012).

[54] J. Kubler, K. H. Hock, J. Sticht, and A. R. Williams, *Density functional theory of non-collinear magnetism*, J. Phys. F **18**, 469 (1988).

[55] J. Kubler, L. Sandratskii, and M. Uhl, *Theory for itinerant electrons in noncollinear and incommensurate structured magnets (invited)*, Journal of Applied Physics **v76**, p6694(6) (1994-11-15), graph.

[56] L. M. Sandratskii, *Noncollinear magnetism in itinerant-electron systems: Theory and applications*, Advances in Physics **47**, 91 (1998).

[57] F. G. Eich, *Non-collinear magnetism in density-functional theories*, PhD thesis, Freie Universität Berlin, 2013.

[58] J. D. F. Essenberger, S. Sharma, Elk-cecam workshop, CECAM-HQ-EPFL, Lausanne, Switzerland, 2011, [Online; accessed 4-September-2017].

[59] D. R. Bowler, *Density functional theory: a tale of success in three codes*, Journal of Physics: Condensed Matter **28**, 421001 (2016).

[60] C. D. Sherrill, *Frontiers in electronic structure theory*, The Journal of Chemical Physics **132**, 110902 (2010).

[61] L. H. Thomas, *The calculation of atomic fields*, Proc. Cam. Phil. Soc. **23**, 542 (1927).

[62] E. Teller, *On the Stability of Molecules in the Thomas-Fermi Theory*, Rev. Mod. Phys. **34**, 627 (1962).

[63] N. L. Balàzs, *Formation of Stable Molecules within the Statistical Theory of Atoms*, Phys. Rev. **156**, 42 (1967).

[64] W. Kohn and L. J. Sham, *Self-Consistent Equations Including Exchange and Correlation Effects*, Phys. Rev. **140**, A1133 (1965).

[65] W. Kohn and L. J. Sham, *Self-consistent equations including exchange and correlation effects*, Phys. Rev. **140**, A1133 (1965).

[66] D. M. Ceperley and B. J. Alder, *Ground State of the Electron Gas by a Stochastic Method*, Phys. Rev. Lett. **45**, 566 (1980).

[67] J. F. Janak, *Proof that $\partial E \partial ni = \epsilon$ in density-functional theory*, Phys. Rev. B **18**, 7165 (1978).

[68] H. J. Monkhorst and J. D. Pack, *Special points for Brillouin-zone integrations*, Phys. Rev. B **13**, 5188 (1976).

[69] D. R. Hamann, M. Schlüter, and C. Chiang, *Norm-Conserving Pseudopotentials*, Phys. Rev. Lett. **43**, 1494 (1979).

[70] P. A. Christiansen, Y. S. Lee, and K. S. Pitzer, *Improved ab initio effective core potentials for molecular calculations*, The Journal of Chemical Physics **71**, 4445 (1979).

[71] D. Vanderbilt, *Soft self-consistent pseudopotentials in a generalized eigenvalue formalism*, Phys. Rev. B **41**, 7892 (1990).

[72] P. E. Blöchl, *Generalized separable potentials for electronic-structure calculations*, Phys. Rev. B **41**, 5414 (1990).

[73] E. Anderson *et al.*, *LAPACK Users' Guide*, Third ed. (Society for Industrial and Applied Mathematics, Philadelphia, PA, 1999).

[74] G. Kresse and J. Furthmüller, *Efficient iterative schemes for ab initio total-energy calculations using a plane-wave basis set*, Phys. Rev. B **54**, 11169 (1996).

[75] P. Pulay, *Improved SCF convergence acceleration*, J. Comput. Chem. **3**, 556 (1982).

[76] C. G. Broyden, *A Class of Methods for Solving Nonlinear Simultaneous Equations*, Math. Comput. **19**, pp. 577 (1965).

[77] N. Marzari, D. Vanderbilt, and M. C. Payne, *Ensemble Density-Functional Theory for Ab Initio Molecular Dynamics of Metals and Finite-Temperature Insulators*, Phys. Rev. Lett. **79**, 1337 (1997).

[78] O. Gunnarsson and B. I. Lundqvist, *Exchange and correlation in atoms, molecules, and solids by the spin-density-functional formalism*, Phys. Rev. B **13**, 4274 (1976).

[79] J. E. Peralta, G. E. Scuseria, and M. J. Frisch, *Noncollinear magnetism in density functional calculations*, Phys. Rev. B **75**, 125119 (2007).

[80] J. Kubler, K. H. Hock, J. Sticht, and A. R. Williams, *Density functional theory of non-collinear magnetism*, Journal of Physics F: Metal Physics **18**, 469 (1988).

[81] U. von Barth and L. Hedin, *A local exchange-correlation potential for the spin polarized case. i*, Journal of Physics C: Solid State Physics **5**, 1629 (1972).

[82] J. P. Perdew, K. Burke, and Y. Wang, *Generalized gradient approximation for the exchange-correlation hole of a many-electron system*, Phys. Rev. B **54**, 16533 (1996).

[83] R. Feynman, *Quantum Electrodynamics* (Avalon Publishing, 1998).

[84] Blender Online Community, *Blender - a 3D modelling and rendering package*, Blender Foundation, Blender Institute, Amsterdam, 2017.

[85] A. Kokalj, *XCrySDen—a new program for displaying crystalline structures and electron densities*, Journal of Molecular Graphics and Modelling **17**, 176 (1999).

[86] T. Williams, C. Kelley, and many others, Gnuplot 4.6: an interactive plotting program, `http://gnuplot.sourceforge.net/`, 2013.

[87] S. J. Clark *et al.*, *First principles methods using CASTEP*, Z. Kristall. **220**, 567 (2005).

[88] R. L. Redington, *Statespecific vibrational anharmonicities in cyclobutadiene and evidence for fast automerization by 12C4H4*, The Journal of Chemical Physics **109**, 10781 (1998).

[89] P. Čársky and J. Michl, *Heavy-atom tunneling in cyclobutadiene:Ab initio calculation of the intensities ofa g Raman lines*, Theoretica chimica acta **84**, 125 (1992).

[90] F. Fantuzzi, T. M. Cardozo, and M. A. C. Nascimento, *The Nature of the Singlet and Triplet States of Cyclobutadiene as Revealed by Quantum Interference*, ChemPhysChem **17**, 288 (2016).

[91] G. Maier, H.-G. Hartan, and T. Sayrac, *Cyclobutadiene—A Square Singlet Molecule?*, Angewandte Chemie International Edition in English **15**, 226 (1976).

[92] D. W. Whitman and B. K. Carpenter, *Limits on the activation parameters for automerization of cyclobutadiene-1,2-d2*, Journal of the American Chemical Society **104**, 6473 (1982).

[93] R. Breslow, R. Grubbs, and S. Murahashi, *Electrochemical evidence for the antiaromaticity of cyclobutadiene*, Journal of the American Chemical Society **92**, 4139 (1970).

[94] V. Gogonea, P. v. R. Schleyer, and P. R. Schreiner, *Consequences of Triplet Aromaticity in 4nπ-Electron Annulenes: Calculation of Magnetic Shieldings for Open-Shell Species*, Angewandte Chemie International Edition **37**, 1945 (1998).

[95] T. Bally, *Cyclobutadiene: The Antiaromatic Paradigm?*, Angewandte Chemie International Edition **45**, 6616 (2006).

[96] A. Fattahi, L. Lis, Z. Tian, and S. R. Kass, *The Heat of Formation of Cyclobutadiene*, Angewandte Chemie International Edition **45**, 4984 (2006).

[97] B. K. Carpenter, *Heavy-atom tunneling as the dominant pathway in a solution-phase reaction? Bond shift in antiaromatic annulenes*, Journal of the American Chemical Society **105**, 1700 (1983).

[98] A. M. Orendt *et al.*, *Carbon-13 NMR and polarized IR spectra of vicinally labeled cyclobutadiene-13C2 in an argon matrix: interconversion of valence tautomers*, Journal of the American Chemical Society **110**, 2648 (1988).

[99] B. Kovacevic, D. Barić, Z. B. Maksić, and T. Müller, *Dominant Role of the π Framework in Cyclobutadiene*, The Journal of Physical Chemistry A **108**, 9126 (2004).

[100] D. Ley, D. Gerbig, and P. R. Schreiner, *Tunnelling control of chemical reactions - the organic chemist's perspective*, Org. Biomol. Chem. **10**, 3781 (2012).

[101] A. Balková and R. J. Bartlett, *A multireference coupled cluster study of the ground state and lowest excited states of cyclobutadiene*, The Journal of Chemical Physics **101**, 8972 (1994).

[102] A. Kostenko *et al.*, *Spectroscopic Observation of the Triplet Diradical State of a Cyclobutadiene*, Angewandte Chemie International Edition **56**, 10183 (2017).

[103] Y. Shiota, M. Kondo, and K. Yoshizawa, *Role of molecular distortions in the spin–orbit coupling between the singlet and triplet states of the 4π electron systems C4H4, C5H5+, and C3H3−*, The Journal of Chemical Physics **115**, 9243 (2001), https://doi.org/10.1063/1.1412250.

[104] J. Binney and D. Skinner, *The Physics of Quantum Mechanics: An Introduction* (Cappella Archive, 2010).

[105] W. T. Borden, *Reactions that involve tunneling by carbon and the role that calculations have played in their study*, Wiley Interdisciplinary Reviews: Computational Molecular Science **6**, 20 (2016).

[106] S. Coleman, *Aspects of Symmetry: Selected Erice Lectures* (Cambridge University Press, 1985).

[107] S. R. McConnell, A. Löhle, and J. Kästner, *Rate constants from instanton theory via a microcanonical approach*, The Journal of Chemical Physics **146**, 074105 (2017).

[108] M. T. Cvitas and S. C. Althorpe, *Locating Instantons in Calculations of Tunneling Splittings: The Test Case of Malonaldehyde*, Journal of Chemical Theory and Computation **12**, 787 (2016).

[109] P. Čársky, V. Špirko, B. A. H. Jr., and L. J. Schaad, *Variational calculations on the Ag vibrational states, the automerization, and the predicted Raman spectrum of cyclobutadiene*, The Journal of Chemical Physics **92**, 6069 (1990).

[110] X. Li and J. Paldus, *Accounting for the exact degeneracy and quasidegeneracy in the automerization of cyclobutadiene via multireference coupledcluster methods*, The Journal of Chemical Physics **131**, 114103 (2009).

[111] B. R. Arnold, J. G. Radziszewski, A. Campion, S. S. Perry, and J. Michl, *The Raman spectrum of matrix-isolated cyclobutadiene. Evidence for environmental hindrance to heavy-atom tunneling?*, Journal of the American Chemical Society **113**, 692 (1991).

[112] T. K. Roy and R. B. Gerber, *Vibrational self-consistent field calculations for spectroscopy of biological molecules: new algorithmic developments and applications*, Phys. Chem. Chem. Phys. **15**, 9468 (2013).

[113] O. Christiansen and J. M. Luis, *Beyond vibrational self-consistent-field methods: Benchmark calculations for the fundamental vibrations of ethylene*, International Journal of Quantum Chemistry **104**, 667, https://onlinelibrary.wiley.com/doi/pdf/10.1002/qua.20615.

[114] O. Christiansen, *Vibrational structure theory: new vibrational wave function methods for calculation of anharmonic vibrational energies and vibrational contributions to molecular properties*, Phys. Chem. Chem. Phys. **9**, 2942 (2007).

[115] J. M. Bowman, K. Christoffel, and F. Tobin, *Application of SCF-SI theory to vibrational motion in polyatomic molecules*, The Journal of Physical Chemistry **83**, 905 (1979), https://doi.org/10.1021/j100471a005.

[116] W. Kohn and L. J. Sham, *Self-Consistent Equations Including Exchange and Correlation Effects*, Phys. Rev. **140**, A1133 (1965).

[117] D. Watkins, *The Matrix Eigenvalue Problem* (Society for Industrial and Applied Mathematics, 2007).

[118] K. V. Fernando and B. N. Parlett, *Accurate singular values and differential qd algorithms*, Numerische Mathematik **67**, 191 (1994).

[119] D. S. Watkins, On gr algorithms for the eigenvalue problem, in *Numerical Linear Algebra, Digital Signal Processing and Parallel Algorithms*, edited by G. H. Golub and P. Van Dooren, pp. 687–693, Berlin, Heidelberg, 1991, Springer Berlin Heidelberg.

[120] I. S. Dhillon and B. N. Parlett, *Relatively robust representations of symmetric tridiagonals*, Linear Algebra and its Applications **309**, 121 (2000).

[121] I. S. Dhillon and B. N. Parlett, *Orthogonal Eigenvectors and Relative Gaps*, SIAM Journal on Matrix Analysis and Applications **25**, 858 (2003).

[122] E. Silberman and H. W. Morgan, *Use of group theory in the interpretation of infrared and Raman spectra* (Oak Ridge National Laboratory, TN, 1977).

[123] C.-K. Lin, H.-C. Chang, and S. H. Lin, *Symmetric Double-Well Potential Model and Its Application to Vibronic Spectra: Studies of Inversion Modes of Ammonia and Nitrogen-Vacancy Defect Centers in Diamond*, The Journal of Physical Chemistry A **111**, 9347 (2007), PMID: 17725334.

[124] A. G. Csaszar and T. Furtenbacher, *Promoting and inhibiting tunneling via nuclear motions*, Phys. Chem. Chem. Phys. **18**, 1092 (2016).

[125] H. Xu, S. Saebo, and C. U. Pittman, *The potential energy surface of singlet cyclobutadiene and substituted analogs: a coupled-cluster study*, Structural Chemistry **25**, 635 (2014).

[126] Y. Apeloig, *The Diamond Within a Silicon Analog of Cyclobutadiene*, Science **331**, 1277 (2011).

[127] M. Born and K. Huang, *Dynamical theory of crystal lattices* (Oxford: Clarendon Press, Oxford, 1954).

[128] L. D. A., *Intensities in Raman spectra I. A bond polarizability theory*, Proceedings of the Royal Society of London A: Mathematical, Physical and Engineering Sciences **217**, 203 (1953).

[129] K. Gough, *Theoretical analysis of molecular polarizabilities and polarizability derivatives in hydrocarbons*, The Journal of chemical physics **91**, 2424 (1989).

[130] P. R. Tulip, *Dielectric and Lattice Dynamical Properties of Molecular Crystals via Density Functional Perturbation Theory: Implementation within a First Principles Code*, PhD thesis, Durham University, 2004.

[131] H. S. Smalø, P.-O. Åstrand, and L. Jensen, *Nonmetallic electronegativity equalization and point-dipole interaction model including exchange interactions for molecular dipole moments and polarizabilities*, The Journal of Chemical Physics **131**, 044101 (2009).

[132] W. T. Borden, *Reactions that involve tunneling by carbon and the role that calculations have played in their study*, Wiley Interdisciplinary Reviews: Computational Molecular Science **6**, 20 (2016).

[133] V. Benderskii, D. Makarov, and C. Wight, *Chemical Dynamics at Low Temperatures* (Wiley, 1994).

[134] R. P. Bell, *Experimental evidence for tunnelling in chemical reactions* (Springer US, Boston, MA, 1980), pp. 106–144.

[135] P. Dirac, *Quantum mechanics of many-electron systems*, Proceedings of the Royal Society of London A: Mathematical, Physical and Engineering Sciences **123**, 714 (1929).

[136] Y. Feng *et al.*, *Evolution of incommensurate spin order with magnetic field and temperature in the itinerant antiferromagnet GdSi*, Phys. Rev. B **88**, 134404 (2013).

[137] W. C. Koehler, J. W. Cable, M. K. Wilkinson, and E. O. Wollan, *Magnetic Structures of Holmium. I. The Virgin State*, Phys. Rev. **151**, 414 (1966).

[138] Z. Barak, E. Fawcett, D. Feder, G. Lorincz, and M. B. Walker, *Experimental and theoretical investigation of the magnetic phase diagram of chromium*, Journal of Physics F: Metal Physics **11**, 915 (1981).

[139] Y. Mizuguchi and Y. Takano, *Review of Fe Chalcogenides as the Simplest Fe-Based Superconductor*, Journal of the Physical Society of Japan **79**, 102001 (2010).

[140] E. E. Rodriguez *et al.*, *Noncollinear spin-density-wave antiferromagnetism in FeAs*, Phys. Rev. B **83**, 134438 (2011).

[141] S. V. Halilov, A. Y. Perlov, P. M. Oppeneer, A. N. Yaresko, and V. N. Antonov, *Magnetocrystalline anisotropy energy in cubic Fe, Co, and Ni: Applicability of local-spin-density theory reexamined*, Phys. Rev. B **57**, 9557 (1998).

[142] K. Selte *et al.*, *The crystal structure of FeAs*, Acta Chem. Scand. A **23**, 2047 (2006).

[143] D. Gonzalez-Alvarez *et al.*, *FeAs: Heat capacity, enthalpy increments, other thermodynamic properties from 5 to 1350 K, and magnetic transition*, The Journal of Chemical Thermodynamics **21**, 363 (1989).

[144] R. Hafner, D. Spišák, R. Lorenz, and J. Hafner, *Magnetic ground state of Cr in density-functional theory*, Phys. Rev. B **65**, 184432 (2002).

[145] R. Blachnik *et al.*, *CrAs: heat capacity, enthalpy increments, thermodynamic properties from 5 to 1280 K, and transitions*, The Journal of Chemical Thermodynamics **10**, 507 (1978).

[146] I. Mannari, *Electrical Resistance of Ferromagnetic Metals*, Progress of Theoretical Physics **22**, 335 (1959).

[147] A. Mackintosh, *Energy gaps in spin-wave spectra*, Physics Letters **4**, 140 (1963).

[148] C. Kittel, *Introduction to solid state physics 6th ed.*. (Wiley, 1986).

[149] K. Segawa and Y. Ando, *Magnetic and Transport Properties of FeAs Single Crystals*, J. Phys. Soc. Japan **78**, 104720 (2009).

[150] K. A. Ziq and A. F. Salem, *Magnetic Properties of FeAs Single Crystal*, Journal of Superconductivity and Novel Magnetism **26**, 1185 (2013).

[151] M. Blume, *Magnetic scattering of x rays (invited)*, Journal of Applied Physics **57**, 3615 (1985).

[152] G. P. M. Poppe and A. Fasolino, X-ray resonant exchange scattering (xres), Accessed: 2017-09-26.

[153] A. Błachowski, K. Ruebenbauer, J. Żukrowski, and Z. Bukowski, *Magnetic anisotropy and lattice dynamics in FeAs studied by Mössbauer spectroscopy*, Journal of Alloys and Compounds **582**, 167 (2014).

[154] S. Blundell, Magnetism in condensed matter, 2003.

[155] J. P. Perdew, K. Burke, and M. Ernzerhof, *Generalized Gradient Approximation Made Simple*, Phys. Rev. Lett. **77**, 3865 (1996).

[156] D. J. Singh, W. E. Pickett, and H. Krakauer, *Gradient-corrected density functionals: Full-potential calculations for iron*, Phys. Rev. B **43**, 11628 (1991).

[157] J. J. Sakurai and E. D. Commins, Modern quantum mechanics, revised edition, 1995.

[158] E. Wigner, *Group theory: and its application to the quantum mechanics of atomic spectra* (Academic Press (New York), 1971).

[159] K. Esler, Accessed: 2017-06-30.

[160] R. S. Mulliken, *Electronic Population Analysis on LCAO-MO Molecular Wave Functions. I*, Journal of Chemical Physics **23**, 1833 (1955).

[161] S. M. Griffin and N. A. Spaldin, *A density functional theory study of FeAs comparing LDA+ U, GGA+ U and hybrid functionals*, arXiv:1401.2277 (2014).

[162] B. Saparov, J. E. Mitchell, and A. S. Sefat, *Properties of binary transition-metal arsenides (T As)*, Supercond. Sci. Tech. **25**, 084016 (2012).

[163] E. C. S. F. R. S, *Ferromagnetism*, Reports on Progress in Physics **11**, 43 (1947).

[164] J. Hubbard, *The magnetism of iron*, Phys. Rev. B **19**, 2626 (1979).

[165] R. P. Feynman, *Forces in Molecules*, Phys. Rev. **56**, 340 (1939).

[166] J. A. Mydosh, *Spin glasses: redux: an updated experimental/materials survey*, Reports on Progress in Physics **78**, 052501 (2015).

[167] T. Moriya, *Spin fluctuations in itinerant electron magnetism* (Springer-Verlag, 1985).

[168] P. Bak, *Commensurate phases, incommensurate phases and the devil's staircase*, Reports on Progress in Physics **45**, 587 (1982).

[169] P. W. Anderson, *Antiferromagnetism. Theory of Superexchange Interaction*, Phys. Rev. **79**, 350 (1950).

[170] B. Weiner and S. B. Trickey, *Fukutome symmetry classification of the Kohn–Sham auxiliary one-matrix and its associated state or ensemble*, International Journal of Quantum Chemistry **69**, 451 (1998).

[171] S. Yamanaka, D. Yamaki, Y. Shigeta, H. Nagao, and K. Yamaguchi, *Noncollinear spin density functional theory for spin-frustrated and spin-degenerate systems*, International Journal of Quantum Chemistry **84**, 670 (2001).

[172] V. M. García-Suárez, C. M. Newman, C. J. Lambert, J. M. Pruneda, and J. Ferrer, *First principles simulations of the magnetic and structural properties of Iron*, The European Physical Journal B - Condensed Matter and Complex Systems **40**, 371 (2004).

[173] N. Mizuno, K. Nakamura, T. Akiyama, and T. Ito, *Noncollinear magnetism and exchange interaction in spin-spiral structures of thin film Fe(110)*, Journal of Physics: Condensed Matter **19**, 365222 (2007).

[174] P. Radaelli, *Symmetry in Crystallography: Understanding the International Tables* (OUP Oxford, 2011).

[175] S. C. Abrahams, L. Guttman, and J. S. Kasper, *Neutron Diffraction Determination of Antiferromagnetism in Face-Centered Cubic (γ) Iron*, Phys. Rev. **127**, 2052 (1962).

[176] A. Lavakumar, Crystal structures, in *Concepts in Physical Metallurgy*, pp. 2–1 to 2–20, Morgan & Claypool Publishers, 2017.

[177] O. N. Mryasov, A. I. Liechtenstein, L. M. Sandratskii, and V. A. Gubanov, *Magnetic structure of FCC iron*, Journal of Physics: Condensed Matter **3**, 7683 (1991).

[178] S. Sharma *et al.*, *First-Principles Approach to Noncollinear Magnetism: Towards Spin Dynamics*, Phys. Rev. Lett. **98**, 196405 (2007).

[179] H. Brooks, *Ferromagnetic Anisotropy and the Itinerant Electron Model*, Phys. Rev. **58**, 909 (1940).

[180] M. Asdente and M. Delitala, *Magnetocrystalline Energy, Electronic Charge Distribution, and Fermi Surface of Iron from a Tight-Binding Calculation*, Phys. Rev. **163**, 497 (1967).

[181] I. Yang, S. Y. Savrasov, and G. Kotliar, *Importance of Correlation Effects on Magnetic Anisotropy in Fe and Ni*, Phys. Rev. Lett. **87**, 216405 (2001).

[182] C. Wang, B. Klein, and H. Krakauer, *Theory of magnetic and structural ordering in iron*, Phys. Rev. Lett. **54**, 1852 (1985).

[183] L. Stixrude, R. E. Cohen, and D. J. Singh, *Iron at high pressure: Linearized-augmented-plane-wave computations in the generalized-gradient approximation*, Phys. Rev. B **50**, 6442 (1994).

[184] H. C. Herper, E. Hoffmann, and P. Entel, *Ab initio full-potential study of the structural and magnetic phase stability of iron*, Phys. Rev. B **60**, 3839 (1999).

[185] J. Hubbard, *The magnetism of iron II*, Phys. Rev. B **30**, 4584 (1979).

[186] R. F. Sabiryanov and S. S. Jaswal, *Magnons and Magnon-Phonon Interactions in Iron*, Phys. Rev. Lett. **83**, 2062 (1999).

[187] I. Levine, *Quantum Chemistry* (Pearson, 2013).

[188] W. L. Roth, *Magnetic Structures of MnO, FeO, CoO, and NiO*, Phys. Rev. **110**, 1333 (1958).

[189] A. K. Cheetham and D. A. O. Hope, *Magnetic ordering and exchange effects in the antiferromagnetic solid solutions* $Mn_xNi_{1-x}O$, Phys. Rev. B **27**, 6964 (1983).

[190] B. E. F. Fender, A. J. Jacobson, and F. A. Wedgwood, *Covalency Parameters in MnO, α-MnS, and NiO*, The Journal of Chemical Physics **48**, 990 (1968).

[191] J. van Elp, R. H. Potze, H. Eskes, R. Berger, and G. A. Sawatzky, *Electronic structure of MnO*, Phys. Rev. B **44**, 1530 (1991).

[192] B. A. Frandsen and S. J. L. Billinge, *Magnetic structure determination from the magnetic pair distribution function (mPDF): ground state of MnO*, Acta Crystallographica Section A **71**, 325 (2015).

[193] A. M. Balagurov, I. A. Bobrikov, S. V. Sumnikov, V. Y. Yushankhai, and N. Mironova-Ulmane, *Magnetostructural phase transitions in NiO and MnO: Neutron diffraction data*, JETP Letters **104**, 88 (2016).

[194] H. Shaked, J. Faber, and R. L. Hitterman, *low-temperature magnetic structure of mno: a high-resolution neutron-diffraction study*, Phys. Rev. B **38**, 11901 (1988).

[195] S. Das, J. E. Coulter, and E. Manousakis, *Convergence of quasiparticle self-consistent GW calculations of transition-metal monoxides*, Phys. Rev. B **91**, 115105 (2015).

[196] K. Terakura, T. Oguchi, A. R. Williams, and J. Kübler, *Band theory of insulating transition-metal monoxides: Band-structure calculations*, Phys. Rev. B **30**, 4734 (1984).

[197] L. F. Mattheiss, *Electronic Structure of the* 3*d Transition-Metal Monoxides. I. Energy-Band Results*, Phys. Rev. B **5**, 290 (1972).

[198] L. F. Mattheiss, *Electronic Structure of the* 3*d Transition-Metal Monoxides. II. Interpretation*, Phys. Rev. B **5**, 306 (1972).

[199] W. E. Pickett, *Electronic structure of the high-temperature oxide superconductors*, Rev. Mod. Phys. **61**, 433 (1989).

[200] V. I. Anisimov, J. Zaanen, and O. K. Andersen, *Band theory and Mott insulators: Hubbard U instead of Stoner I*, Phys. Rev. B **44**, 943 (1991).

[201] V. I Anisimov, F. Aryasetiawan, and A. Lichtenstein, *First-Principles Calculations of the Electronic Structure and Spectra of Strongly Correlated Systems: The LDA+ U Method*, **9**, 767 (1997).

[202] P. J. Brown and T. Chatterji, *Neutron diffraction and polarimetric study of the magnetic and crystal structures of HoMnO 3 and YMnO 3*, Journal of Physics: Condensed Matter **18**, 10085 (2006).

[203] A. Lima and M. Lalic, *Ground-state magnetic structure of hexagonal YMnO3 compound: A non-collinear spin density functional theory study*, Journal of Magnetism and Magnetic Materials **416**, 236 (2016).

[204] A. Baldereschi and E. Tosatti, *Mean-value point and dielectric properties of semiconductors and insulators*, Phys. Rev. B **17**, 4710 (1978).

[205] D. J. Chadi and M. L. Cohen, *Special Points in the Brillouin Zone*, Phys. Rev. B **8**, 5747 (1973).

[206] P. Hohenberg and W. Kohn, *Inhomogeneous electron gas*, Phys. Rev. **136**, B864 (1964).

[207] S. M. Griffin and N. A. Spaldin, *A density functional theory study of the influence of exchange-correlation functionals on the properties of FeAs*, Journal of Physics: Condensed Matter **29**, 215604 (2017).